The physics of fast radio bursts

Bing Zhang[*]

*Nevada Center for Astrophysics and Department of Physics and Astronomy,
University of Nevada, Las Vegas, Las Vegas, Nevada 89154, USA*

(published 25 September 2023)

Fast radio bursts (FRBs), millisecond-duration bursts prevailing in the radio sky, are the latest large puzzle in the Universe and have been a subject of intense observational and theoretical investigations in recent years. The rapid accumulation of observational data has painted the following sketch about the physical origin of FRBs: They predominantly originate from cosmological distances, so their sources produce the most extreme coherent radio emission in the Universe; at least some, probably most, FRBs are repeating sources that do not invoke cataclysmic events; and at least some FRBs are produced by magnetars, neutron stars with the strongest magnetic fields in the Universe. Many open questions regarding the physical origin(s) and mechanism(s) of FRBs remain. This review addresses the phenomenology and possible underlying physics of FRBs. Topics include a summary of the observational data, basic plasma physics, general constraints on FRB models from the data, radiation mechanisms, source and environment models, and propagation effects, as well as FRBs as cosmological probes. Current pressing problems and future prospects are also discussed.

CONTENTS

[*]bing.zhang@unlv.edu

035005-1

I. INTRODUCTION

Fast radio bursts (FRBs), millisecond-duration radio bursts originating predominantly from cosmological distances, are one of the few remaining unsolved puzzles in contemporary astrophysics. The study of these mysterious events has a relatively short history. The first reported FRB was detected on July 24, 2001 (now called FRB 20010724, for FRB naming conventions; see Sec. II.A), by the Parkes 64-m telescope in Australia. It was not discovered until later by Duncan Lorimer and collaborators during an archival search for burstlike events. The burst was located 3° from the Small Magellanic Cloud (SMC), had a peak flux density $S_\nu \gtrsim 30$ Jy at ~ 1.4 GHz, a duration (also called "width"; see Sec. II.B) $W \sim 5$ ms, and a dispersion measure (DM) ~ 375 cm^{-3} pc (see the definition in Sec. II.E; this is a proxy of distance from the source to Earth), which greatly exceeds the value expected from Milky Way or SMC, suggesting that it likely originated from a cosmological distance. The discovery was published in 2007 in the journal Science (Lorimer et al., 2007), so 2007 was widely regarded as the birth of the FRB research field. Note that there was an unconfirmed report about some repeating bursts from the nearby galaxy M87 back in 1980 (Linscott and Erkes, 1980) that were regarded by most as radio frequency interferences (RFIs). However, the inferred energy ($\sim 10^{40}$ erg) and luminosity ($\sim 10^{37}$ erg s^{-1}) of those bursts fall into the range of typical known FRBs. If confirmed, those bursts could be the earliest detected repeating FRB bursts.

Like the studies of other cosmological puzzles [the closest analogy being gamma-ray bursts (GRBs)], the study of FRBs went through several phases from uncertainty about whether they are even genuinely astronomical to getting to the bottom of the emitting source(s) and physical mechanisms. While it took half a century (from 1967 to 2017) to solve the full puzzle of GRBs, the study of FRBs is progressing much faster. In a mere 15-yr period, observations have led to answers or partial answers to the following four questions: (1) Are they astronomical? (2) Are there multiple types? (3) Where are they? (4) What make them?

Fully addressing the first question took 5–8 yr. After the detection of the "Lorimer burst," no similar events were detected until several years later. On the other hand, there were many somewhat similar events that were detected by the Parkes telescope that appeared artificial. These so-called perytons (Burke-Spolaor et al., 2011) differed from genuine FRBs by being detected by all 13 beams of the Parkes telescope and clustering in time. Their existence cast doubt on the astronomical origin of the Lorimer burst itself. In 2012, Keane et al. (2012) reported another highly dispersed burstlike event (later called FRB 20010621A) with $S_\nu \sim 400$ mJy at ~ 1.4 GHz, $W \sim 7.8$ ms, and DM ~ 746 cm^{-3} pc. Since the burst was close to the Galactic plane, the excess DM is not significant. The possibility that the burst was a giant pulse of an underlying pulsar or from a rotating radio transient [a type of part-time pulsar (McLaughlin et al., 2006)] was not ruled out. Strong support was given to the existence of extragalactic and cosmological FRBs the next year, when Thornton et al. (2013) reported four more FRBs discovered by the Parkes telescope. It was shown that all the events were detected in one or a few beams of the telescope, unlike the perytons. They were from high Galactic latitudes and had large DM values in great excess of the Milky Way (MW) values in those directions, similar to the Lorimer burst. Thornton et al. (2013) also estimated that the event rate of FRBs is high, about 10^4/d all sky above an ~ 3 Jy ms fluence density threshold at 1.4 GHz. Finally, the perytons were eventually identified as artificial signals caused during the magnetron shutdown phase of a microwave oven when one impatiently opens the oven before heating is over (Petroff et al., 2015c). Since none of those seemingly genuine bursts happened during the dining time when perytons were generated, this development finally separated perytons from true FRBs and suggested that FRBs are indeed of an astronomical origin.

After the initial detection of the Lorimer burst, the source direction was intensively monitored for 90 additional hours, but no detection of repeated bursts was made (Lorimer et al., 2007). Later detected FRBs were all one-off events until 2016, when Spitler et al. (2016) first reported that one FRB source, named FRB 20121102A (also called FRB 121102, R1, or Spitler burst), emitted repeated bursts with a similar DM as detected by the Arecibo 305-m radio telescope. This source remained the sole detected repeater for a short period before the Canadian Hydrogen Intensity Mapping Experiment (CHIME) discovered a few more repeating sources (Amiri et al., 2019; Andersen et al., 2019). More repeaters were discovered through deep monitoring with the Australian Square Kilometre Array Pathfinder (ASKAP) (Kumar et al., 2019) and the Five-Hundred-Meter Aperture Spherical Radio Telescope (FAST) in China (Luo et al., 2020; C. H. Niu et al., 2022). On the other hand, most detected FRBs are still one off. At least observationally one can therefore say that there are two apparent types, repeaters and nonrepeaters, but it is unclear whether all nonrepeaters will eventually repeat.

The repeating nature of FRB 20121102A allowed targeted observations using the Karl G. Jansky Very Large Array and

the Arecibo Telescope to detect additional bursts and eventually localize the source using the interferometric technique (Chatterjee *et al.*, 2017). This enabled the detection of a compact persistent radio source in association with the burst source (Chatterjee *et al.*, 2017). Further very-long-baseline radio interferometric observations using the European VLBI Network and the Arecibo Telescope refined the persistent radio source to milliarcsecond scale, which corresponds to ≤ 70 pc at the source (Marcote *et al.*, 2017). It also led to direct identification of the source host galaxy in the optical band, which is a dwarf-star-forming galaxy at redshift $z = 0.19$ (Tendulkar *et al.*, 2017). This finally answered the "where" question and established the cosmological origin of FRBs. Localizations of FRBs, both repeaters and nonrepeaters, were later made via interferometry by the ASKAP Collaboration, the Deep Synotic Array Collaboration, and several other groups, which revealed a gallery of host galaxy types and positions of the FRBs within the hosts (Bannister *et al.*, 2019; Prochaska *et al.*, 2019; Ravi *et al.*, 2019; Macquart *et al.*, 2020; Marcote *et al.*, 2020; Bhandari *et al.*, 2022; Xu *et al.*, 2022) and confirmation of the theoretically expected $\mathrm{DM_{IGM}} - z$ correlation (Macquart *et al.*, 2020).

The question "What make them?" is the most difficult to answer. Shortly after the reports of the discovery of the first FRBs, especially the four more FRBs reported by Thornton *et al.* (2013), dozens of theoretical models were proposed; see Platts *et al.* (2019) for a summary. The bright persistent radio source (Chatterjee *et al.*, 2017), the actively star-forming host galaxy (Tendulkar *et al.*, 2017), and an extremely large Faraday rotation measure [(RM) a proxy of the strength of magnetic field and density near the FRB source; see Sec. II.G for a definition] of FRB 20121102A (Michilli *et al.*, 2018) suggested that young magnetars might be sources of active repeaters. Even though a twin source FRB 20190520B was later detected by FAST (C. H. Niu *et al.*, 2022), most other sources, including both repeating and nonrepeating FRBs, display diverse emission and host galaxy properties that are inconsistent with such a simple picture.

A definite clue on the magnetar origin of at least some FRBs came from the detection of the Galactic FRB 20200428. The identification of cosmological origin of FRBs suggests that if an FRB would occur in the Milky Way Galaxy, it should be extremely bright. This expectation was realized on April 28, 2020, when an extremely high fluence, FRB-like event with two pulses was detected by CHIME (Andersen *et al.*, 2020) and the Survey for Transient Astronomical Radio Emission 2 (STARE2) (Bochenek *et al.*, 2020), which detected only one of the two pulses. The radio burst was associated with a hard x-ray burst (XRB) from a Galactic magnetar named a soft gamma-ray repeater (SGR) J1935 + 2154 during one of its active phases (Mereghetti *et al.*, 2020; C. K. Li *et al.*, 2021; Ridnaia *et al.*, 2021; Tavani *et al.*, 2021). This established a long-speculated connection between FRBs and magnetars. Deep monitoring of the magnetar by FAST, on the other hand, suggested that the majority of x-ray bursts emitted by the magnetar are actually not associated with FRBs (Lin *et al.*, 2020), suggesting the rarity of the magnetar FRB-XRB associations. Deeper monitoring by FAST and European radio telescopes discovered fainter radio pulses from this source (C.-F. Zhang *et al.*, 2020; Kirsten *et al.*, 2021).

Despite this breakthrough discovery, the mystery of cosmological FRBs remains. Some recent discoveries pose more clues and, in the meantime, create more confusion in the large picture. An apparent ~16-d periodicity of a repeating source FRB 20180916B (also called FRB 180916.J0158 + 65) was reported from the CHIME observations (Amiri *et al.*, 2020). Follow-up observations suggest that the active window is "chromatic," with bursts detected at higher frequencies appearing at somewhat earlier phases than those detected at lower frequencies (Pastor-Marazuela *et al.*, 2021; Pleunis *et al.*, 2021b). A tentative ~157-d period was also suggested for FRB 20121102A (Rajwade *et al.*, 2020). Bursting activities during the active windows are actually sporadic. For FRB 20121102A, more than 1600 bursts were detected by FAST in a total of 59.5 observing hours spanning 47 d during one active window (D. Li *et al.*, 2021), but there were no active bursts detected during some projected active windows later.

A repeating source FRB 20200120E discovered by the CHIME/FRB Collaboration was found to be associated with a nearby spiral galaxy M81 at a distance of 3.6 Mpc (Bhardwaj *et al.*, 2021). Follow-up observations surprisingly localized the source to a globular cluster in the host galaxy (Kirsten *et al.*, 2022). The bursts from the source have lower luminosities than typical cosmological FRBs. Some bursts have rapid temporal structures as short as 60 ns (Nimmo *et al.*, 2021).

The FAST-detected repeating FRB source FRB 20190520B (C. H. Niu *et al.*, 2022), besides showing similar properties as FRB 20121102A, also showed some unique properties. For example, its large RM showed an extreme sign change in a month timescale (Dai *et al.*, 2022; Anna-Thomas *et al.*, 2023). Located at $z = 0.241 \pm 0.001$, its estimated host contribution of the DM exceeds ~1000 pc cm^{-2}, which is the largest value among known FRBs (C. H. Niu *et al.*, 2022).

The polarization properties of FRBs, which have been closely studied over the years, provide clues in understanding FRB sources, environments, and radiation mechanisms. Evidence of a large rotation measure (RM $\simeq 186$ rad m^{-2}) in excess of the Galactic value was first reported for FRB 20110523A, which suggested a dense magnetized plasma associated with the FRB (Masui *et al.*, 2015). More extreme values (of the order of 10^5 rad m^{-2}) were detected from FRB 20121102A (Michilli *et al.*, 2018) and FRB 20190520B (Dai *et al.*, 2022; Anna-Thomas *et al.*, 2023). FRB 20121102A showed an essentially nonvarying polarization angle across each burst during individual bursts (Michilli *et al.*, 2018). An opposite case was observed in another active repeating source FRB 20180301A, which showed diverse polarization angle swings among different bursts (Luo *et al.*, 2020). Intense follow-up observations of the CHIME-discovered repeating source FRB 20201124A using FAST (Xu *et al.*, 2022) revealed peculiar short-term polarization property variations, including unpredictable RM evolution and nonevolution and oscillations of circular and linear polarization degrees and linear polarization angles as a function of wavelength in a small fraction of bursts. Significant circular polarization from the source was discovered (Kumar *et al.*, 2022; Xu *et al.*, 2022). Extreme RM variations, including a reversal of the RM (Dai *et al.*, 2022; Anna-Thomas *et al.*, 2023), were observed

in FRB 20190529B. All of these suggest a dynamically evolving magnetized environment around repeating FRB sources. A frequency-dependent polarization degree was noticed in a sample of repeating FRBs, which may be interpreted as a scatter of the RM due to the multipath propagation effect of radio emission (Feng *et al.*, 2022).

One special source detected by CHIME, FRB 20191221A, was identified to show a 216.8(1) ms periodicity with a significance of 6.5σ (Andersen *et al.*, 2022). It has a roughly 3-s-long duration, making it an outlier in the FRB population. However, this periodicity offers strong support to a magnetar (or pulsar) origin of this special event.

With the rapid accumulation of observational data, the physical understanding of FRBs also advanced steadily in recent years, from knowing essentially nothing to painting a rough sketch of the FRB production mechanism. As in the field of gamma-ray bursts (Nemiroff, 1994), the early years of the FRB study also witnessed a large number of theoretical papers dedicated to guessing the origin of FRBs based on limited observational data (Platts *et al.*, 2019). Not surprisingly, most of these ideas are quickly disfavored or completely rejected as data are accumulated. Rather than surveying all the proposed models [such a task was carried out; see Platts *et al.* (2019) and an online FRB theory wiki page[1]], this review focuses on a critical assessment of the leading ideas of interpreting FRBs that are currently under active investigation.

In the following, I discuss the topics related to the physical nature of FRBs. I first summarize observational facts in Sec. II to prepare for later discussion and refer interested readers to more comprehensive observational reviews; see Cordes and Chatterjee (2019), Petroff, Hessels, and Lorimer (2019, 2022), and Bailes (2022), and references therein.[2] After reviewing the basic plasma physics relevant to the FRB mechanisms (Sec. III), I discuss some generic theoretical arguments that pose constraints on any FRB models (Sec. IV). Section V discusses possible mechanisms for generating the extremely coherent radiation of FRBs, with two general types of models (magnetospheric and relativistic shock models) discussed and compared. This is followed by a survey of the source models (Sec. VI) for repeating FRBs and some ideas of generating genuinely nonrepeating FRBs. The environmental models of FRBs are discussed in Sec. VII, and the propagation effects of FRBs are addressed in Sec. VIII. FRBs as various cosmological probes are summarized in Sec. IX. The review ends with a discussion of the problems in and prospects of the field in Sec. X. Early theoretical reviews on the surveys of many theoretical models were given by Katz (2018b), Popov, Postnov, and Pshirkov (2018), and Platts *et al.* (2019). Theoretical reviews on the physical mechanisms of FRBs were given by Zhang (2020c), Lyubarsky (2021), and Xiao, Wang, and Dai (2021).

Note that the FRB field is a rapidly evolving area. For the topics discussed in this review, I have tried to separate the parts that involve robust physics (Secs. III, IV, and VIII) from those that are undergoing intense investigation (Secs. II and V–VII). In the latter part, I attempt to describe both sides of the debate for controversial topics and critically comment on the pros and cons of various models. It is my hope that at least the former part and most of the latter part will have a long shelf life.

II. FRB PHENOMENOLOGY

A. Arrival times, coordinates, and naming convention

A detected FRB is characterized by the time it is detected on Earth (corrected to the barycentric time) and the spatial coordinate of the source. There have been different conventions to name FRBs. Since they are bursting events in nature, a widely adopted scheme is to name them based on the time that the burst was detected, similar to GRBs, i.e., FRB YYMMDD. However, since some (probably most) FRB sources emit repeated bursts, one has to adopt the time at which the first burst was detected to name the source. For example, the first repeater is widely named FRB 121102 or, now, officially FRB 20121102A. When CHIME came online, many detected FRBs flooded in. Since multiple FRBs could be detected on the same day and some of them could be repeating ones, the CHIME/FRB Collaboration adopted a more informative and complicated name by combining the time information and spatial information (right ascension and declination) of the source. For example, the second repeater detected by CHIME was named FRB $180814.\text{J}0422 + 73$ (now officially FRB 20180814A). There was also a suggestion to call repeaters R#, where the pound sign is an assigned number based on the sequence of their discoveries. For example, FRB 121102 and FRB 180814.J0422+73 are also called R1 and R2, respectively. The 16-d periodic repeater FRB 20180916B is R3. Another possibility was that one can add a prefix "r" before the FRB name if a source is discovered to repeat. For example, R1, R2, and R3 may also be called rFRB 20121102A, rFRB 20180814A, and rFRB 20180916B, respectively. There was an unofficial vote for the preferred naming convention among the attendees of the February 2019 FRB Workshop in Amsterdam, Netherlands, but no consensus was reached. The commonly adopted naming convention in the literature now follows the Transient Name Server (TNS) convention FRB YYYYMMDDabc. I believe that the information as to whether the source is a repeater is important. Throughout the review, I follow the official TNS convention but add the "r" prefix for repeating sources in the rest of the review. Other nicknames are also used occasionally. Note that the prefix "r" is not a universally accepted convention but rather my personal preference.

B. Temporal properties

The typical observed duration (also known as width W) of an FRB is milliseconds. This duration is believed to be the convolution of the intrinsic pulse duration at the source (W_i), plasma scattering broadening (τ_{sc}) during the propagation of the pulse, as well as instrumental broadening by the radio telescope (t_{tel}). Assuming uncorrelated Gaussian profiles of

---

[1]See https://frbtheorycat.org.

[2]On the other hand, this review includes the most updated observational progress that was not included in the previous reviews.
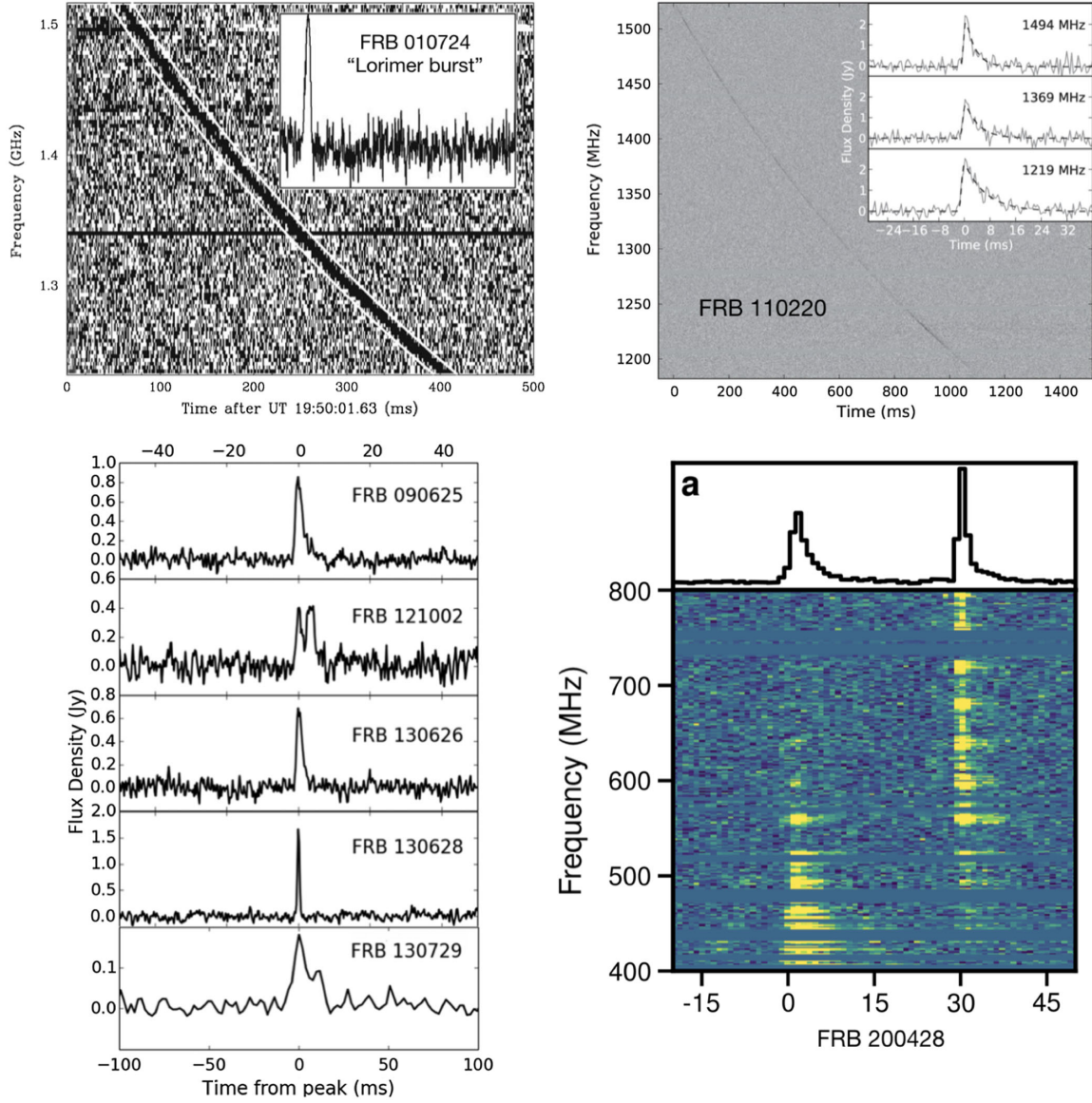
FIG. 1. Diverse light curves of FRBs. Upper left panel: first reported FRB, FRB 20010724, or the Lorimer burst. Main panel: frequency vs arrival time of the radio burst shown as a result of dispersion. Inset: light curve of the burst after the effect of dispersion is corrected for. From Lorimer *et al.*, 2007. Upper right panel: FRB 20110220 depiction showing frequency-dependent widths. The convention is the same as in the upper left panel, but the light curves are constructed for three central frequencies. The decaying tail is wider in lower frequencies as a result of plasma scattering along the line of sight. From Thornton *et al.*, 2013. Lower left panel: five additional FRBs detected with the Parkes 64-m telescope. From Champion *et al.*, 2016. Lower right panel: Galactic FRB 20200428 from SGR J1935+2154 as detected by the CHIME telescope. The upper panel is the light curve, while the lower panel shows the two-dimensional frequency-time distribution (also called the dynamic spectrum) of the emission after dispersion is corrected for. From Andersen *et al.*, 2020.

these components, one can write the observed width as (Cordes and McLaughlin, 2003; Lorimer and Kramer, 2012)

$$W = [W_i^2(1 + z)^2 + \tau_{sc}^2 + t_{ins}^2]^{1/2}, \quad (1)$$

where W_i is the intrinsic duration of the FRB pulse in the source frame (the observed duration is longer by a factor of $1 + z$ due to the cosmological time-dilation effect);

$$\tau_{sc} = [\tau_{MW}^2 + \tau_{IGM}^2 + \tau_{HG}^2(1 + z)^2]^{1/2} \quad (2)$$

is the scattering time, which includes the contributions from the Milky Way, the intergalactic medium (IGM), and the FRB host galaxy (see Sec. VIII.A for a discussion of scattering); and

$$t_{ins} = (t_{samp}^2 + \Delta t_{DM}^2 + \Delta t_{\delta DM}^2 + \Delta t_{\delta \nu}^2)^{1/2} \quad (3)$$

is the instrumental broadening (Cordes and McLaughlin, 2003; Petroff, Hessels, and Lorimer, 2019), which includes the data sampling interval t_{samp}, the frequency-dependent smearing due to the DM
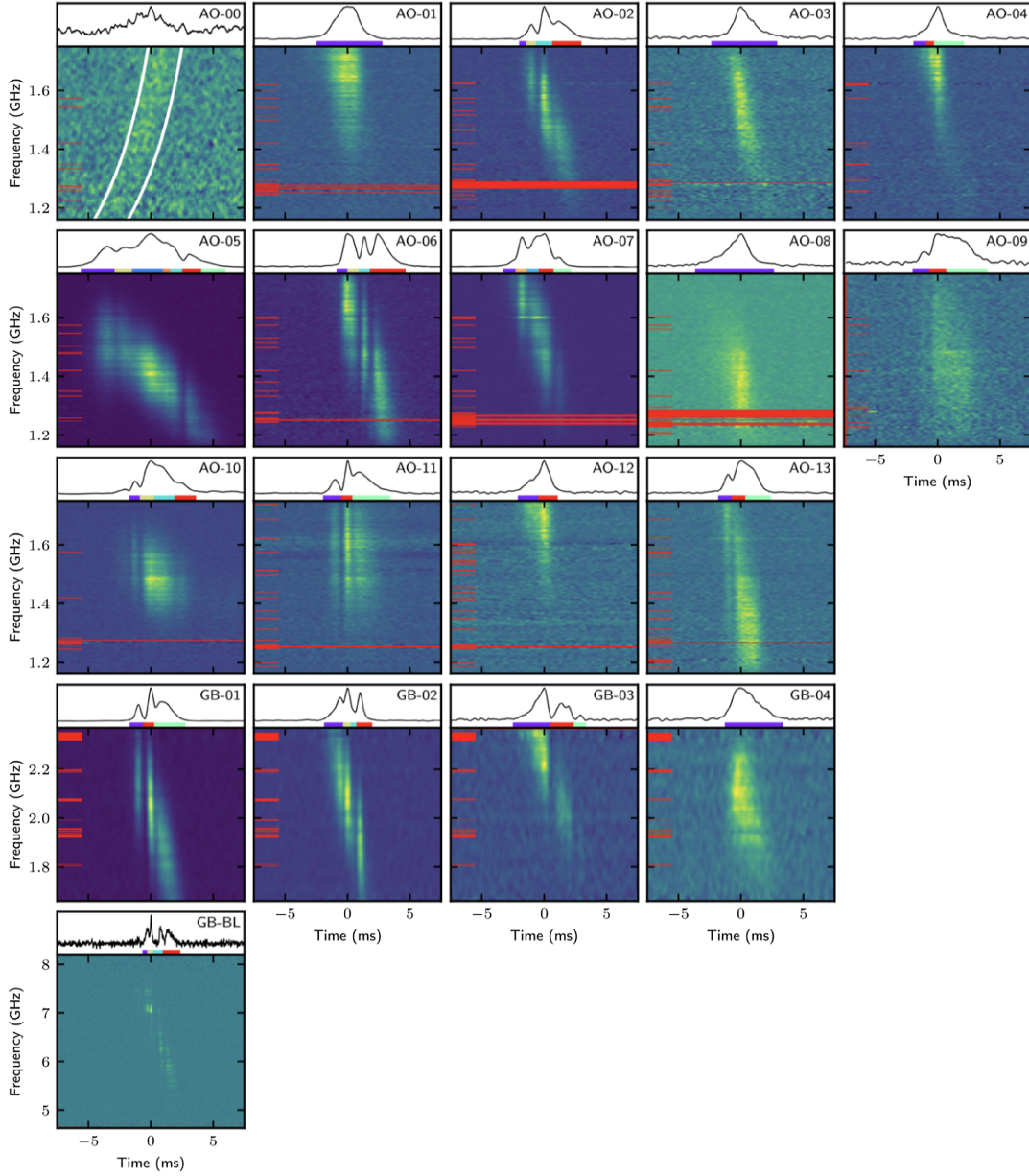
FIG. 2.   An example of the dynamic spectra of individual bursts from rFRB 20121102A (R1) that show a down-drifting of pulses with frequency, which is also called the sad trombone effect. Horizontal solid red bars denote RFI excision. From Hessels *et al.*, 2019.

$$\Delta t_{DM} = (8.3 \ \mu s) DM \Delta \nu_{MHz} \nu_{GHz}^{-3}, \qquad (4)$$

the smearing due to the error of DM $\Delta t_{\delta DM}$, and the smearing due to the bandwidth $\Delta t_{\delta \nu} \sim (\Delta \nu)^{-1} = 1 \ \mu s (\Delta \nu_{MHz})^{-1}$.

As shown in Fig. 1, the light curves of FRBs show diverse behaviors. Many FRBs have a single pulse (or indistinguishable multiple pulses). However, some FRBs (such as FRB 20121002) show an apparently temporal structure (Champion *et al.*, 2016). The Galactic FRB 20200428 had two pulses separated by roughly 30 ms, which can also be regarded as a repeating source that emitted two bursts. Some bursts clearly show an asymmetric pulse profile, with a longer decaying wing than the rising phase. This decaying wing is frequency dependent, with a longer tail at a lower frequency [such as FRB 20111220, which is shown in the upper right panel of

Fig. 1 (Thornton *et al.*, 2013)]. The frequency-dependent scattering tail of these FRBs is consistent with $\tau_{sc} \propto \nu^{-4}$ or $\tau_{sc} \propto \nu^{-4.4}$, as predicted by the plasma scattering effect (Luan and Goldreich, 2014; Cordes *et al.*, 2016; Xu and Zhang, 2016).

One interesting temporal feature of some FRBs is a down-drifting of pulses with frequency (Amiri *et al.*, 2019; Andersen *et al.*, 2019; Hessels *et al.*, 2019), which is also called the sad trombone effect (Fig. 2). This is after correcting the standard dispersive delay due to propagation and is likely related to the intrinsic radiation physics of FRBs. Such a behavior is often seen in repeating FRB bursts. The down-drifting predominates. The opposite trend (up-drifting) is much rarer (Amiri *et al.*, 2021; D. J. Zhou *et al.*, 2022), even though the two apparently separated pulses in FRB 20200428 indeed showed a higher peak frequency in the second pulse (Andersen *et al.*, 2020).

The morphology of FRBs, especially for repeaters, has been studied extensively. Pleunis *et al.* (2021a) studied 536 bursts from 492 sources from the CHIME first catalog and identified four observed archetypes of burst morphology, namely, "simple broadband," "simple narrowband," "temporally complex," and "downward drifting." D. J. Zhou *et al.* (2022) studied more than 700 bursts from one repeating source rFRB 20201124A detected by FAST and identified five morphological types based on the drifting patterns: downward drifting, upward drifting (a small fraction), complex, no drifting, and no evidence for drifting. Subtypes are introduced as needed based on the emission frequency range in the band (low, middle, high, and wide), and also the number of subpulses in the burst (one, two, or multiple). Altogether 18 morphological subtypes have been identified. The longest burst includes 11 pulses lasting 124 ms. There are no apparent correlations among duration, bandwidth, central frequency, and flux.

C. Spectral properties

FRBs have been detected from 110 MHz (Pleunis *et al.*, 2021b) to at least 8 GHz (Gajjar *et al.*, 2018). Nondetection at higher frequencies could be due to limited sensitivity (Law *et al.*, 2017) or the difficulty to achieve strong coherence. The lack of dispersion at high frequencies makes it difficult to differentiate RFIs from true signals, which might also contribute to the deficit. The nondetection at lower frequencies, especially with Low-Frequency Array at 145 MHz, may suggest an intrinsic hardening of spectrum at low frequencies, probably due to a certain absorption process (Karastergiou *et al.*, 2015).

The spectral shape of some early FRBs was not well measured. If one approximates the spectral shape as a power-law function $F_\nu \propto \nu^{-\alpha}$, the power-law index α was observed to vary significantly from case to case. For example, the Lorimer burst had $\alpha = 4 \pm 1$ (Lorimer *et al.*, 2007), while FRB 20110523A had $\alpha = 7.8 \pm 0.4$ (Masui *et al.*, 2015). Even for different bursts from the same repeating source α can be significantly different. For example, the α values of rFRB 20121102A bursts ranged from -10.4 to $+13.6$ (Spitler *et al.*, 2016). Such a large variation may be an indication that the intrinsic spectrum of FRBs is narrow. Multitelescope studies of some repeater bursts often show that the bursts detected in one band are not detected in another, such as for rFRB 20121102A (Law *et al.*, 2017) and rFRB 20180916B (Pastor-Marazuela *et al.*, 2021). This suggests that the spectra of these bursts are not simple power laws. Indeed, the dynamical spectra of FRBs (Figs. 1 and 2) often show that the bursts are bright only in part of the entire observing bandpass. The Galactic magnetar burst FRB 20200428 had two pulses detected by CHIME (Andersen *et al.*, 2020), but only the second pulse with a higher peak frequency was detected by STARE2 (Bochenek *et al.*, 2020), which has a higher bandpass than CHIME. This again suggests that the FRB spectra could be narrow. A systematic study of the spectral properties of more than 700 bursts from rFRB 20201124A detected by FAST (D. J. Zhou *et al.*, 2022) suggested that the majority of repeating FRBs have narrow spectra, with a typical spectral bandwidth of ~ 275 MHz in the FAST band.

D. Repetition and periodicity

More than 20 FRBs have been reported to repeat (Spitler *et al.*, 2016; Amiri *et al.*, 2019; Andersen *et al.*, 2019; Kumar *et al.*, 2019; Luo *et al.*, 2020; C. H. Niu *et al.*, 2022). Since a repeating FRB is identified whenever one more burst is detected from the same source, it is essentially impossible to claim that an FRB source is not a repeater. In fact, it is possible that all FRB sources repeat but with a wide range of repetition rate. Since the observed FRB rate density exceeds the rate density of supernovae, the most common catastrophic events, it is immediately inferred that the majority of the FRBs have to be from repeating sources (Ravi, 2019; Luo, Men *et al.*, 2020). The remaining question is whether all FRB sources repeat and whether there is a minority population of FRBs that originate from catastrophic events (Palaniswamy, Li, and Zhang, 2018; Caleb *et al.*, 2019).

Some differences in the observational properties between repeaters and apparent one-off FRBs have been noticed, but no conclusive results have been drawn.

- The CHIME/FRB Collaboration (Andersen *et al.*, 2019; Amiri *et al.*, 2021; Pleunis *et al.*, 2021a) reported that repeaters tend to have wider widths than one-off FRBs. They also tend to have narrower spectra than one-off bursts. However, the two populations have overlapping parameter spaces, so it is difficult to definitely tell whether an apparent one-off burst actually belongs to the repeater population.
- The frequency down-drifting feature has been observed in several repeating sources (Amiri *et al.*, 2019; Hessels *et al.*, 2019). However, not all bursts from these sources and not all repeating sources show such a behavior. On the other hand, some apparently one-off FRBs show such a behavior, which may be regarded as candidates for repeating FRBs.
- Both supervised (Luo, Zhu-Ge, and Zhang, 2023) and unsupervised (Zhu-Ge, Luo, and Zhang, 2023) machine-learning algorithms applied on the first CHIME/FRB catalog reached the consensus that repeaters and most nonrepeaters seem to belong to different categories. Including both observed and derived parameters, both algorithms recognize brightness temperature and rest-frame spectral width as the two dominant traits to differentiate between the two categories. Some common repeater candidates can be identified from these two independent categories of machine-learning methods (Luo, Zhu-Ge, and Zhang, 2023; Zhu-Ge, Luo, and Zhang, 2023). However, the accuracy of the predicted repeaters is not high in comparison with the latest repeater catalog reported by the CHIME/FRB Collaboration (Andersen *et al.*, 2023a) as more high-luminosity FRBs turn into repeaters.

Note that some polarization properties, for instance, varying the polarization angle (PA) (Cho *et al.*, 2020) or circular polarization (Dai *et al.*, 2021), had once been proposed to be the unique properties of nonrepeaters. However, later observations showed that some repeaters also possess these properties (Luo *et al.*, 2020; Xu *et al.*, 2022). It is now clear that polarization properties cannot be used to differentiate between the two categories.
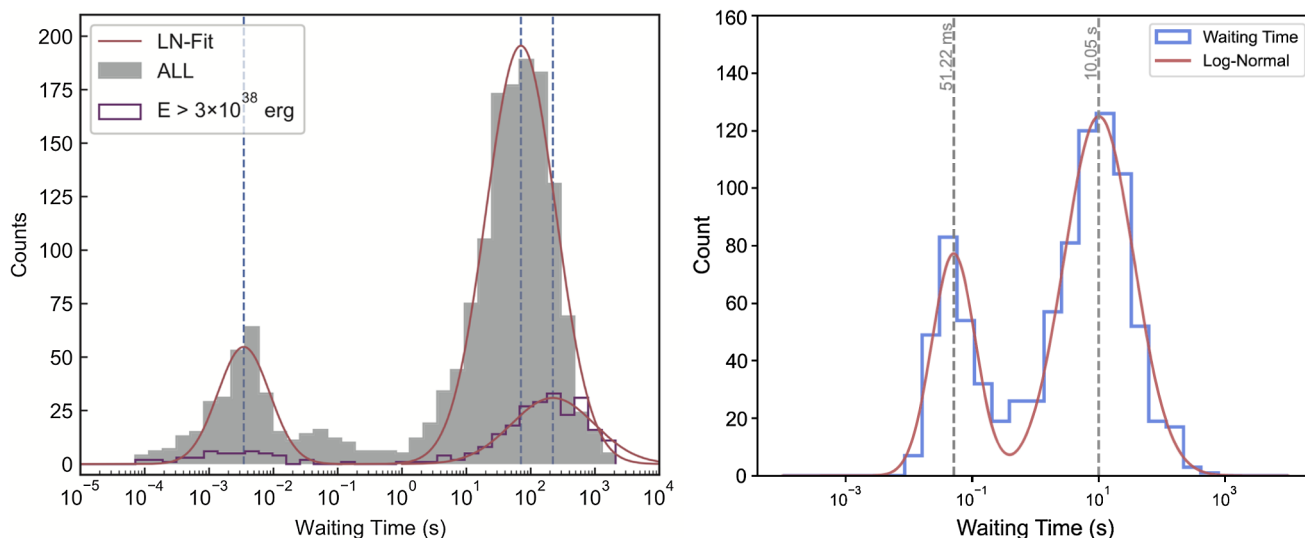
FIG. 3. The waiting time distributions of repeating FRBs. Left panel: the case of rFRB 20121102A during the 2019 active episode. The two peaks occur at a few milliseconds and ~100 s. From D. Li *et al.*, 2021. Right panel: the case of rFRB 20201124A during an active 4-d episode in September 2021. The second peak is at ~10 s, suggesting an active episode. In an earlier episode of the same source in April 2021, the second peak was at ~100 s, suggesting that the same source can have significantly different activity levels, and hence different waiting time distributions. From Zhang *et al.*, 2022.

If all FRBs are repeaters, then at least some apparent one-off FRBs must have a low repetition rate. Palaniswamy, Li, and Zhang (2018) and Caleb *et al.* (2019) suggested that most FRBs cannot have a repetition rate similar to rFRB 20121102A. Otherwise, many of them should have been observed to repeat. Indeed, extensive follow-up observations of some bright FRBs, such as the Lorimer burst, have thus far failed to detect any repeated bursts (Lorimer *et al.*, 2007; Petroff *et al.*, 2015b), suggesting that they might have a different origin. Katz (2019) pointed out that the duty factor defined as $D \equiv \langle S \rangle^2 / \langle S^2 \rangle$ (S is the flux density) may be used to differentiate repeaters from nonrepeaters, with active repeaters such as rFRB 20121102A having $D \sim 10^{-5}$ and nonrepeaters having $D \sim 10^{-8}$–10^{-10}.

In their simulations, Ai, Gao, and Zhang (2021) suggested that tracking the evolution of observed repeater fraction $F_{r,obs}$ may shed light on the existence of genuinely nonrepeating FRBs. This is because if genuinely nonrepeating FRBs indeed exist, their numbers will linearly increase as a function of time. The number of repeaters, on the other hand, may approach a limit with time. As a result, $F_{r,obs}$ is expected to reach a peak and then decline. Therefore, detecting such a peak would strongly suggest the existence of genuinely nonrepeating FRBs. In reality, however, depending on parameters and possible evolution of source populations, the time to reach the peak could be long and the duration at the peak could also be long. Long-term monitoring of the sky using CHIME-like wide-field survey telescopes will hold the key to placing constraints on the existence of genuinely nonrepeating FRBs. Note that recent CHIME observations suggested that $F_{r,obs}$ already stays constant for a few years, which is consistent with the hypothesis that genuinely nonrepeating FRBs exist (Andersen *et al.*, 2023b).

Searches for periodicity of repeating FRB sources have been carried out extensively. The early targeted periods in the searches were in the millisecond to second range, which is similar to the periods of known pulsars and magnetars. Deep searches of periodicity in this period range for rFRB 20121102A [see Zhang *et al.* (2018), D. Li *et al.* (2021), Hewitt *et al.* (2022), and an independent search by Katz (2022b)] and rFRB 20201124A (J.-R. Niu *et al.*, 2022; Xu *et al.*, 2022) using thousands of bursts all led to null results, suggesting that FRB bursts are likely not giant pulses of rotating neutron stars (NSs). On the other hand, unexpected, long periods (or active cycles) were found in some repeating sources. The most robust case is the CHIME-discovered rFRB 20180916B, which shows a ~16-d period with an ~5-d active window (Amiri *et al.*, 2020). The duration and phase of the active window seems to be frequency dependent, with the windows in higher frequencies appearing earlier in phase and being narrower than the windows in lower frequencies (Pastor-Marazuela *et al.*, 2021; Pleunis *et al.*, 2021b). Long-term monitoring of rFRB 20121102A also revealed a possible long-term ~160-d periodicity (Rajwade *et al.*, 2020; Cruces *et al.*, 2021). Long-term monitoring of rFRB 20121102A with FAST suggests that bursts are often missing during the predicted active window and the duty cycle of the periodicity becomes greater than 50% (Wang *et al.* 2023). This casts a shadow on the claimed periodicity. Finally, the "oddball" source FRB 20191221A was detected to have a 0.2168-s period with a significance of 6.5σ (Andersen *et al.*, 2022). Since the total duration (~3 s) is much longer than other FRBs, this event likely has a different origin from the bulk of the FRB population. On the other hand, a deep periodicity search of rFRB 20201124A bursts (J.-R. Niu *et al.*, 2022) suggested that even though no global periodicity was found, fake local periodicity in adjacent burst clusters can be found with a significance of up to 3.9σ. This cautions one against claiming any periodicity from clustered bursts with significance $\lesssim 4\sigma$.

One interesting common feature of active repeaters is that the waiting time distributions of their bursts show two distinct peaks (D. Li *et al.*, 2021; J.-R. Niu *et al.*, 2022; Xu *et al.*,

2022; Zhang et al., 2022; D. J. Zhou et al., 2022). As shown in Fig. 3, the first peak occurs in approximately milliseconds, and the exact value depends on how distinct bursts are defined. The second peak actually depends on the activity level of the source, ranging from tens to hundreds of seconds, even for the same source at different epochs. The bridge between the two peaks lies at approximately tens of milliseconds. Since some FRB bursts show multiple peaks, the short separations of bursts in the first component of waiting time distribution can be regarded as due to the similar origin as multipeaks, which may be related to the continuous activity of the FRB source from one emission episode. D. J. Zhou et al. (2022) defined "burst clusters" that include all the bursts whose relative waiting times fall within this first waiting time peak. The second peak apparently scales with the global activity level of the source. More observations are needed to see whether the dip between the two components may carry information about the periodicity of the underlying engine.

E. Dispersion measure and distance

Radio waves in a plasma are dispersed, with waves with lower frequencies delayed with respect to waves with higher frequencies. The DM (see Sec. III.B for details) describes the degree of such delay. The best-fit DM is obtained for each FRB when it is discovered,[3] and it carries the physical meaning of the column density of free electrons along the line of sight from the source to the observer (in $pc\,cm^{-3}$). Since FRBs are from cosmological distances, the DM can be written most generally as

$$DM = \int_0^{D_z} \frac{n_e(l)}{1 + z(l)} dl, \quad (5)$$

where n_e (a function of location denoted by l) is the local electron number density, z is the redshift at that location, l is the comoving distance from the observer to a location along the path of propagation, and

$$D_z = \frac{c}{H_0} \int_0^z \frac{dz'}{E(z')} \quad (6)$$

is the comoving distance from the observer to the source, where

$$E(z) = \sqrt{\Omega_m(1 + z)^3 + \Omega_k(1 + z)^2 + \Omega_{DE}f(z)}, \quad (7)$$

$$f(z) = \exp\left[3\int_0^z \frac{[1 + w(z')]dz'}{1 + z'}\right], \quad (8)$$

H_0 is the Hubble constant, Ω_m, Ω_k, and Ω_Λ are the energy density fractions of matter, curvature, and dark energy, respectively, and $w(z) \equiv p(z)/\rho(z)$ is the dark energy equation of state parameter. For the concordance lambda cold dark

---

---

[3]The FRB search algorithm scans through a range of DM values to correct for such a delay. The DM of FRB is assigned to either the highest signal-to-noise (S/N) ratio or the finest burst temporal structure (Hessels et al., 2019).

matter (ΛCDM) cosmological model, one has $\Omega_k = 0$, $\Omega_{DE} = \Omega_\Lambda$, $w = -1$, and $f(z) = 1$.

The observed DM is usually split into multiple terms (Thornton et al., 2013, Deng and Zhang, 2014, Prochaska and Zheng, 2019)

$$DM = DM_{MW} + DM_{halo} + DM_{IGM} + \frac{DM_{host} + DM_{src}}{1 + z}, \quad (9)$$

where DM_{MW}, DM_{halo}, DM_{IGM}, DM_{host}, and DM_{src} are the contributions from the Milky Way, its halo, the intergalactic medium (IGM), the host galaxy, and the immediate environment of the source, respectively. Notice that the observed contributions from the last two components are smaller by a factor of $1 + z$, where z is the source redshift. The Milky Way term DM_{MW} can be obtained using the MW electron density models derived from the radio pulsar data (Cordes and Lazio, 2002; Yao, Manchester, and Wang, 2017) (with a $> 50\%$ uncertainty). The extended Milky Way halo contributes to an additional $DM_{halo} \sim 30 - 80\,pc\,cm^{-3}$ beyond DM_{MW} (Dolag et al., 2015; Prochaska and Zheng, 2019).

The IGM component of DM is a function of redshift (Ioka, 2003; Inoue, 2004). The full expression reads (Deng and Zhang, 2014; Gao, Li, and Zhang, 2014; Zhou et al., 2014; Macquart et al., 2020)

$$\langle DM_{IGM}(z)\rangle = \frac{3cH_0\Omega_b f_{IGM}}{8\pi Gm_p} \int_0^z \frac{\chi(z')(1 + z')dz'}{E(z')}, \quad (10)$$

where

$$\chi(z) \simeq \tfrac{3}{4}\chi_{e,H}(z) + \tfrac{1}{8}\chi_{e,He}(z), \quad (11)$$

noticing that the cosmological mass fractions of H and He are $\sim3/4$ and $\sim1/4$, respectively, Ω_b is the energy density fraction of baryons, f_{IGM} is the fraction of baryons in the IGM, and $\chi_{e,H}(z)$ and $\chi_{e,He}(z)$ are the fractions of ionized electrons in hydrogen (H) and helium (He), respectively, as a function of redshift. The DM-z relation is roughly linear at low redshifts (Ioka, 2003; Inoue, 2004). With the standard cosmological parameters as measured by the Planck mission (Ade et al., 2016), one can derive a rough linear relation at $z < 3$ (Zhang, 2018a; Pol et al., 2019; Cordes, Ocker, and Chatterjee, 2021)

$$\langle DM_{IGM}\rangle \simeq (855\,pc\,cm^{-3})z\left(\frac{H_0}{67.74\,kms^{-1}\,kpc^{-1}}\right)$$
$$\times \left(\frac{\Omega_b}{0.0486}\right)\left(\frac{f_{IGM}}{0.83}\right)\left(\frac{\chi}{7/8}\right), \quad (12)$$

where f_{IGM} is normalized to ~0.83 (Fukugita, Hogan, and Peebles, 1998; Z. Li et al., 2020). In the literature, the DM-z relation is also called the Macquart relation to honor J.-P. Macquart's leadership in the ASKAP Collaboration to precisely localize a sample of FRBs and measure their redshifts to prove the theoretically motivated relation (10). Notice that Eqs. (10) and (12) apply to average values. For individual FRBs, the measured DM can be either greater or smaller than the theoretical value due to the inhomogeneity of the IGM caused by large-scale structures (Ioka, 2003; McQuinn, 2014).

TABLE I. Published FRBs with measured redshifts, their observed DM values, and the MW contributions.

FRB	z	DM[a]	$DM_{MW}(NE2001)$[b]	$DM_{MW}(YMW16)$[c]	Reference
rFRB 20121102A	0.192 73	∼557	∼188	∼287	Tendulkar *et al.* (2017)
FRB 20171020A	0.0087	∼114	∼37	∼25	Mahony *et al.* (2018)
rFRB 20180301A	0.3304	∼517	∼152	∼254	Luo *et al.* (2020)
rFRB 20180916B	0.0337	∼349	∼199	∼325	Marcote *et al.* (2020)
rFRB 20180924C	0.3214	∼362	∼41	∼28	Bannister *et al.* (2019)
FRB 20181030A	0.0039	∼104	∼41	∼33	Bhandari *et al.* (2022)
FRB 20181112A	0.4755	∼589	∼42	∼29	Prochaska *et al.* (2019)
FRB 20190102C	0.2913	∼363	∼57	∼43	Macquart *et al.* (2020)
rFRB 20190520B	0.241	∼1205	∼60	∼50	C. H. Niu *et al.* (2022)
FRB 20190523A	0.6600	∼761	∼37	∼30	Ravi *et al.* (2019)
FRB 20190608B	0.1178	∼339	∼37	∼27	Macquart *et al.* (2020)
FRB 20190611B	0.3778	∼321	∼58	∼44	Macquart *et al.* (2020)
FRB 20190614D	0.60	∼959	∼88	∼109	Law *et al.* (2020)
rFRB 20190711A	0.5220	∼593	∼56	∼43	Macquart *et al.* (2020)
FRB 20190714A	0.2365	∼504	∼39	∼31	Bhandari *et al.* (2022)
FRB 20191001A	0.2340	∼508	∼44	∼31	Bhandari *et al.* (2022)
FRB 20191228A	0.2432	∼298	∼32	∼20	Bhandari *et al.* (2022)
rFRB 20200120E	0.0008	∼88	∼41	∼33	Kirsten *et al.* (2022)
FRB 20200430A	0.1608	∼380	∼27	∼26	Bhandari *et al.* (2022)
FRB 20200906A	0.3688	∼578	∼36	∼38	Bhandari *et al.* (2022)
rFRB 20201124A	0.0979	∼414	∼140	∼197	Ravi *et al.* (2022)

[a]All DMs are in $pc\,cm^{-3}$.
[b]Calculated from the NE2001 model (Cordes and Lazio, 2002). Data provided by Ye Li who ran the script provided at https://pypi.org/project/pyne2001/.
[c]Calculated from the YMW17 model (Yao, Manchester, and Wang, 2017) using the website interface https://www.atnf.csiro.au/research/pulsar/ymw16/.

The redshifts of the localized FRBs (Table I) indeed follow the theoretical expectations (Bannister *et al.*, 2017; Tendulkar *et al.*, 2017; Prochaska *et al.*, 2019; Ravi *et al.*, 2019; Macquart *et al.*, 2020; Marcote *et al.*, 2020). After deducting the Milky Way contribution, the external component of DM indeed shows a rough linear relation with z, with the best-fit line consistent with the prediction of the ΛCDM model (Macquart *et al.*, 2020). Using the sample of Macquart *et al.* (2020) and systematically deducting an average DM_{host} value, the DM-z relation could give a constraint on $f_{IGM} \sim 0.85$ (Z. Li *et al.*, 2020), which is consistent with previous results (Fukugita, Hogan, and Peebles, 1998).

Figure 4 gives the updated DM_E-z relation with the 21 redshift-known FRBs listed in Table I. The vertical axis is $DM_E = DM - DM_{MW} - DM_{halo}$, where the NE2001 model (Cordes and Lazio, 2002) and $DM_{halo} = 30\,pc\,cm^{-3}$ have been adopted. A simple linear regression best fit is presented. Using the YMW17 model (Yao, Manchester, and Wang, 2017) or the average NE2001/YMW17 model leads to similar results, with slightly different regression results,

$$DM_E = 934.9z + 126.7, \quad NE2001, \quad (13)$$

$$DM_E = 979.7z + 103.1, \quad YMW17, \quad (14)$$

$$DM_E = 957.3z + 114.9, \quad average. \quad (15)$$

In Eqs. (13)–(15) the slope can be compared with the prediction in Eq. (12), and the y intersection can be regarded as the average $(DM_{host} + DM_{src})/(1 + z)$. Comparing the

fitting results to Eq. (12), one can tentatively draw the conclusion that $f_{IGM} > 0.9$, which is greater than the estimate from the past (Fukugita, Hogan, and Peebles, 1998). Considering that the outlier rFRB 20190520B with large $DM_{host} + DM_{src}$ (C. H. Niu *et al.*, 2022) might have leveraged the y intersection, an average value of $DM_{host} + DM_{src} \sim 100\,pc\,cm^{-3}$ would be reasonable. A systematically lower
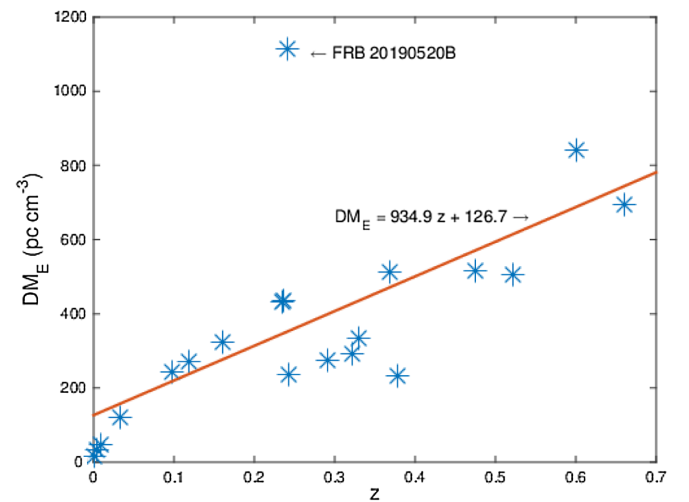

FIG. 4. DM-z relation of 21 FRBs with known redshifts, which is an updated version of the results of Macquart *et al.* (2020). The NE2001 electron density model and $DM_{halo} = 30\,pc\,cm^{-3}$ are adopted. The best-fit linear regression line is plotted. rFRB 20190520B has an abnormally large DM_{host} (C. H. Niu *et al.*, 2022), which is marked separately.

DM_E than the linear fit is noticeable at low redshifts, but this may be a result of large-scale density fluctuations. More data are needed to judge whether there is a systematic deficit of DM_E at low redshifts.

F. Luminosity, energy, and brightness temperature

With measured redshifts, the isotropic-equivalent energy and peak luminosity of FRBs can be measured precisely. Because the DM-z relation has been confirmed by the data, for most FRBs without redshift measurements the measured DM values can be used to estimate the redshift, and hence the energetics, of the FRBs. Lacking the geometric beaming information of FRBs, one can estimate only the isotropic-equivalent values of the peak luminosity and energy. The best estimates depend on the spectral shape of the FRB. If the FRB spectra are narrowband with emission contained within the telescope observing band (which is the case for most bursts from repeaters) (D. J. Zhou et al., 2022), it is more appropriate to multiply the bandwidth $\Delta\nu$ by the specific flux to obtain the luminosity. On the other hand, if the FRB spectra are broadband (which is relevant to some nonrepeating FRBs, such as the Lorimer burst) (Lorimer et al., 2007) with emission extending beyond the telescope observing band, it would be more appropriate to multiply the band central frequency ν_c by the specific flux to obtain luminosity (Zhang, 2018a). Therefore, in general one can write

$$
\begin{aligned}
L_{p,\text{iso}} &\simeq 4\pi D_L^2 \mathcal{S}_{\nu,p} \times \begin{cases} \Delta\nu, & \text{narrow spectrum,} \\ \nu_c, & \text{broad spectrum,} \end{cases} \\
&= (4\pi \times 10^{42}\ \text{erg s}^{-1}) \left(\frac{D_L}{10^{28}\ \text{cm}}\right)^2 \frac{\mathcal{S}_{\nu,p}}{\text{Jy}} \frac{(\Delta\nu \text{ or } \nu_c)}{\text{GHz}},
\end{aligned}
$$
(16)

$$
\begin{aligned}
E_{\text{iso}} &\simeq \frac{4\pi D_L^2}{1+z} \mathcal{F}_\nu \times \begin{cases} \Delta\nu, & \text{narrow spectrum,} \\ \nu_c, & \text{broad spectrum,} \end{cases} \\
&= \frac{4\pi \times 10^{39}\ \text{erg}}{1+z} \left(\frac{D_L}{10^{28}\ \text{cm}}\right)^2 \frac{\mathcal{F}_\nu}{\text{Jy ms}} \frac{(\Delta\nu \text{ or } \nu_c)}{\text{GHz}},
\end{aligned}
$$
(17)

where $\mathcal{S}_{\nu,p}$ is the specific peak flux density, $\mathcal{F}_\nu$ is the specific fluence, and $D_L = (1+z)D_z$ is the luminosity distance. The isotropic peak luminosities of known FRBs vary from (Ravi et al., 2019; Bochenek et al., 2020) $\sim 10^{38}$ erg s^{-1} to a few 10^{46} erg s^{-1}. The corresponding isotropic energies vary from a few 10^{35} erg to a few 10^{43} erg. The luminosity is extremely high by the radio pulsar standard but is minuscule by the GRB standard. The true energetics of FRBs should be reduced by a beaming factor $f_b = \max(\Delta\Omega/4\pi, 1/4\gamma^2) \leq 1$, where $\Delta\Omega$ is the solid angle of the geometric beam and γ is the Lorentz factor of the FRB emitter ($1/\gamma$ is the half kinetic beaming angle for an FRB emitter traveling close to the speed of light). For a one-off FRB, a successful FRB engine should generate a luminosity and an energy at least of the order of $f_b L_p$ and $f_b E$, respectively. Observationally, the majority of hard x-ray bursts from SGR J1935+2154 were not associated with FRBs (Lin et al., 2020). One possibility is that FRB emitters (at least those produced by magnetars) are narrowly beamed. If so, one

would also expect to detect less-luminous but longer-duration radio bursts ("slow radio bursts") with a line of sight outside the emission beam (Zhang, 2021).

The combination of high luminosity and a short variability timescale of an FRB defines an extremely high brightness temperature T_b. One can derive this by noticing that the observed specific intensity $I_\nu = S_\nu/\Delta\Omega$, where S_ν is the observed specific flux, $\Delta\Omega = \pi(c\Delta t_0)^2/D_A^2$ is the solid angle of the source viewed at the observer location [$\Delta t_0 = \Delta t/(1+z)$ is the rest-frame duration of the burst, while $c\Delta t_0$ is adopted as the transverse scale, which is true for a nonrelativistic, spherical, transparent emitter], and $D_A = D_z/(1+z) = D_L/(1+z)^2$ is the angular diameter distance of the source. Considering an imaginary blackbody emitter with temperature $T_b(\nu_0)$ at the rest-frame frequency $\nu_0 = (1+z)\nu$ and noticing that $I_\nu(\nu_0) \simeq 2k_B T_b(\nu_0)(\nu_0^2/c^2)$ in the Rayleigh-Jeans regime (k_B is the Boltzmann constant) and $I_\nu(\nu_0) = I_\nu(\nu)(1+z)^3$ (i.e., I_ν/ν^3 is constant), one finally obtains the brightness temperature at the source frequency ν_0 (Luo, Zhu-Ge, and Zhang, 2023),[4]

$$
\begin{aligned}
T_b(\nu_0) &= \frac{\mathcal{S}_\nu D_A^2 (1+z)^3}{2\pi k_B (\nu\Delta t)^2} = \frac{\mathcal{S}_\nu D_L^2}{2\pi k_B (\nu\Delta t)^2 (1+z)} \\
&\simeq (1.2 \times 10^{36}\ \text{K}) \frac{\mathcal{S}_\nu}{\text{Jy}} \left(\frac{\nu}{\text{GHz}}\right)^{-2} \left(\frac{\Delta t}{\text{ms}}\right)^{-2} \\
&\quad \times \begin{cases} (1+z)^3 \left(\dfrac{D_A}{10^{28}\ \text{cm}}\right)^2, \\ \dfrac{1}{1+z} \left(\dfrac{D_L}{10^{28}\ \text{cm}}\right)^2. \end{cases}
\end{aligned}
$$
(18)

The physical meaning of T_b is the imaginary temperature of the emitter if the photons and the electrons that emit the photons are in thermal equilibrium. This is apparently not the case for FRBs. The gigantic T_b ($\sim 10^{36}$ K for nominal FRB parameters) is much greater than any temperature allowed for incoherent radiation; see Sec. IV.E for details. This demands the radiation mechanism for FRB emission to be "coherent," i.e., the radiation by relativistic electrons must not only not be absorbed but also greatly enhanced with respect to the total expected emission if the electrons radiate independently (or incoherently). Before the discovery of FRBs, radio pulsars were the only known sources of producing extremely high T_b (typically $\sim 10^{25}$–10^{30} K). FRBs further push the limit of the degree of coherent radiation in the Universe.

G. Polarization properties and rotation measure

According to Petroff, Hessels, and Lorimer (2019), early polarization measurements indicated a puzzling,

---

[4]If the emitter is moving relativistically toward Earth with a Lorentz factor Γ, the transverse size in the comoving frame would be $\Gamma c\Delta t$, such that T_b' is smaller by a factor of Γ^2 with respect to Eq. (18). The observer-frame T_b is boosted by a factor of $\sim\Gamma$, so the overall T_b is smaller by a factor of Γ than Eq. (18); see also Lyubarsky (2021). Here I define T_b solely based on observables without assuming whether the source has relativistic motion.

heterogeneous picture: the polarization properties can vary significantly among bursts. The high-quality polarization data accumulated later suggested a more consistent picture: it seems that most FRBs have strongly polarized emission. The linear polarization degree is typically $\Pi_L > 30\%$, and sometimes nearly 100% (Michilli *et al.*, 2018; Cho *et al.*, 2020; Day *et al.*, 2020; Luo *et al.*, 2020). The apparent low polarization observed in some FRBs might be intrinsic but could also be due to the large Faraday RM [see Eq. (19)] in these sources, as is the case for rFRB 20121102A (Michilli *et al.*, 2018). A frequency-dependent linear polarization degree has been observed in some FRBs, but it could be understood that the multipath propagation effect introduces a scatter of the RM so that the intrinsically strong polarization is smeared at low frequencies (Feng *et al.*, 2022). Strong circular polarization has been observed in both apparently nonrepeating FRBs (Masui *et al.*, 2015; Petroff *et al.*, 2015a; Caleb *et al.*, 2018) and repeating FRBs (Kumar *et al.*, 2022; Xu *et al.*, 2022). For linear polarization, the PA remains constant across each burst for some FRBs (such as rFRB 20121102A) (Michilli *et al.*, 2018); see Fig. 5, upper panels. However, in some other FRBs, both apparent one-off ones (Cho *et al.*, 2020) and repeating ones (Luo, Men *et al.*, 2020), swings of PA across each burst are observed, and the swing patterns are diverse among bursts (Fig. 5, lower panels). For the most studied repeater rFRB 20201124A, even though most of bursts are consistent with nonvarying PAs, significant PA variations above 5σ are observed in $\sim 33\%$ of bursts (Jiang *et al.*, 2022).

Linearly polarized radio waves propagating in a magnetized medium would have the polarization angle undergoing a frequency-dependent variation known as Faraday rotation. The degree of rotation is measured by the rotation measure defined by

$$ \mathrm{RM} = (-0.81 \ \mathrm{rad \, m^{-2}}) \int_0^{D_z} \frac{[B_\parallel(l)/\mu\mathrm{G}]n_e(l)}{[1+z(l)]^2} \, dl, \qquad (19) $$

where $B_\parallel(l)$ is the *l*-dependent magnetic field strength along the line of sight (in microgauss), n_e is the number density of the medium along the line of sight in $\mathrm{cm^{-3}}$, and *l* is parsecs. FRBs have a wide range of measured RM absolute values: whereas some of them have sizable RMs ranging from a few hundred to $\sim 10^5 \ \mathrm{rad \, m^{-2}}$ in the case of FRB 20121102A (Michilli *et al.*, 2018), some others have RMs consistent with being close to zero and could be used to place a constraint on the magnetic field strength in the IGM (Ravi *et al.*, 2016). The distribution of RM/DM of FRBs, which gives a rough estimate of $|B_\parallel|$, is slightly larger but not inconsistent with the distribution of Galactic pulsars (W.-Y. Wang *et al.*, 2020).

The observed RM values of active repeaters show interesting variations. The first repeater rFRB 20121102A (Michilli *et al.*, 2018) showed a secular decaying trend in RM. Short-term RM variation was observed in rFRB 20180301A (Luo, Men *et al.*, 2020) and more clearly in rFRB 20201124A (Xu *et al.*, 2022). As shown in Fig. 6 (upper panel), during an active episode of rFRB 20201124A, the RM of the source showed irregular variations during the

first 36 d and turned to essentially invariant for another 18 d before the source is quenched (Xu *et al.*, 2022). Another active repeater rFRB 20190520B (C. H. Niu *et al.*, 2022) showed an even stranger behavior. Its large RM value of the order of $10^4 \ \mathrm{rad \, m^{-2}}$ underwent an unexpected reversal within six months (Dai *et al.*, 2022; Anna-Thomas *et al.*, 2023); see Fig. 6, lower panel.

H. Global properties

The DM-*z* relation allows one to estimate the isotropic peak luminosity and energy of the FRBs. For individual sources, the estimated luminosity or energy can have a large error because of the uncertainty of the correlation. When a large sample of FRBs is considered, the uncertainties can be averaged out so that the luminosity or energy function of the FRBs can be reasonably studied. Independent groups (Luo *et al.*, 2018; Lu and Piro, 2019; Hashimoto *et al.*, 2020; Lu, Kumar, and Zhang, 2020; Luo, Men *et al.*, 2020; Zhang *et al.*, 2021; Hashimoto *et al.*, 2022; Zhang and Zhang, 2022) reached the consistent conclusion that the bulk of the energy or luminosity function can be fit with the following power-law distribution:

$$ N(E)dE \propto E^{-\gamma_E}dE, \qquad N(L)dL \propto L^{-\gamma_L}dL. \quad (20) $$

The index $\gamma_E \sim \gamma_L$ is not well constrained [for instance, 1.3–1.9 (Lu and Piro, 2019) or 1.5–2.1 (Luo, Men *et al.*, 2020)], but a central value of 1.8 seems to be able to accommodate FRBs in at least 7 orders of magnitude, extending from $\sim 10^{26} \ \mathrm{erg \, Hz^{-1}}$ for the Galactic FRB 20200428 to $\sim 10^{33} \ \mathrm{erg \, Hz^{-1}}$, above which a possible exponential cutoff may exist (Lu, Kumar, and Zhang, 2020; Luo, Men *et al.*, 2020); see Fig. 7, upper panel.

Besides global energy and luminosity distributions among FRB sources, for active repeaters one can derive detailed energy and luminosity distributions for individual sources. The most comprehensive analysis was done for a few active repeaters using FAST data. D. Li *et al.* (2021) reported the detection of more than 1600 bursts detected from rFRB 20121102A in 47 d and found that there were two components in the energy distribution. Whereas the high-energy part is consistent with a power-law distribution, a distinct log-normal distribution component peaking at $E_0 \sim 4.8 \times 10^{37}$ erg at 1.25 GHz was observed (Fig. 7, lower panel). The energy distributions of rFRB 20201124A (Xu *et al.*, 2022; Zhang *et al.*, 2022) and rFRB 20190520B (C. H. Niu *et al.*, 2022) show somewhat different shapes, but all require more complicated functions than the simple power-law function.

With the observed DM distribution, one can in principle constrain the redshift distribution of the FRBs. The observed DM distribution is the convolution of the intrinsic redshift distribution, FRB energy or luminosity function, and the instrumental fluence or flux sensitivity threshold, so inferring it is not straightforward. One needs to apply a uniform sample (for instance, FRBs detected with the same telescope) to place the constraints. With the pre-CHIME data, Zhang *et al.* (2021) tested several astrophysically motivated redshift distribution models, from a model assuming FRBs tracking
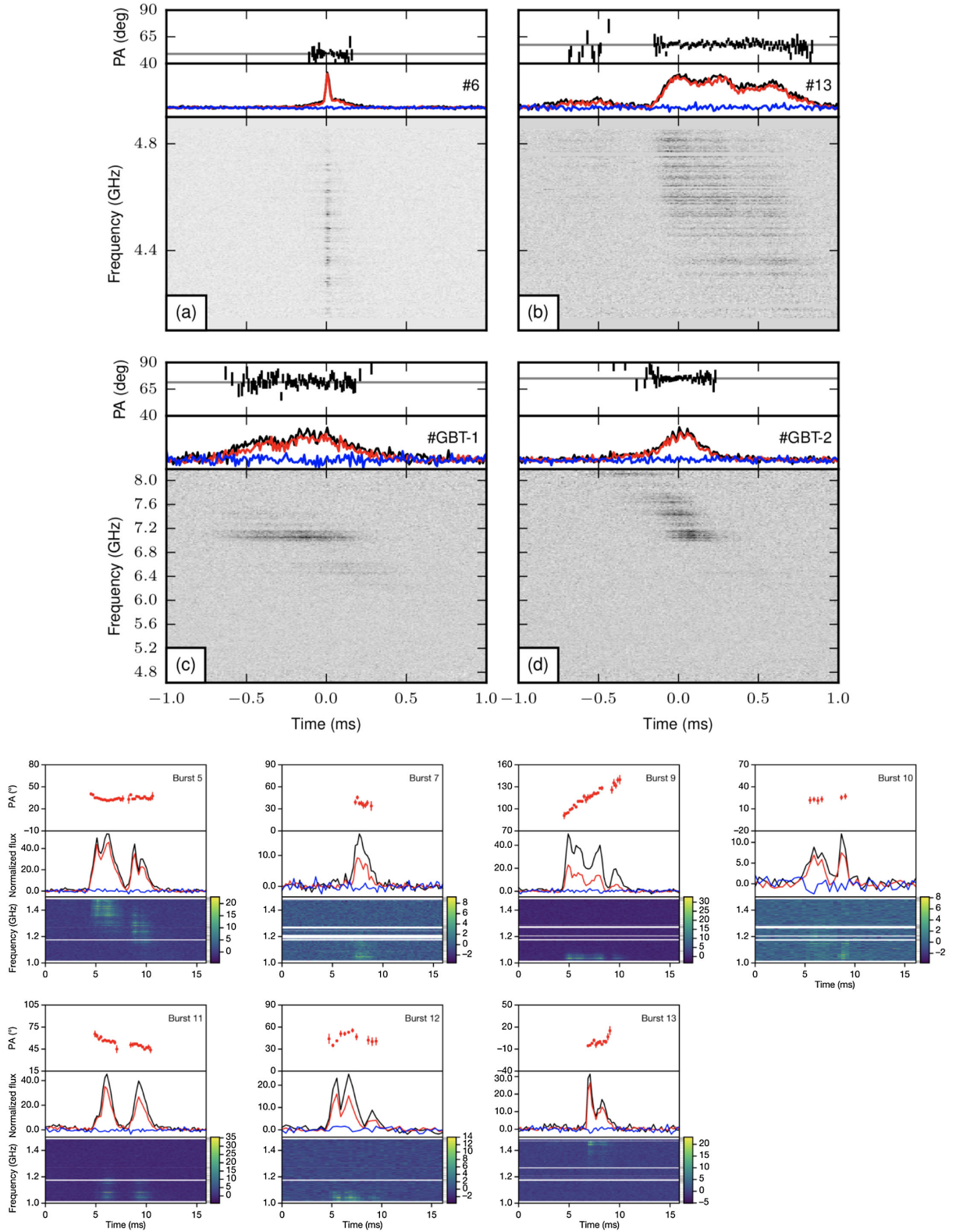
FIG. 5. Examples of polarization angle (PA) variations across individual bursts from FRBs. In each subfigure, the upper panel is the polarization angle, the middle panel is the light curve, and the lower panel is the dynamic spectrum. Upper panels: constant PA in rFRB 20121102A bursts. From Michilli et al., 2018. Lower panels: diverse PA swing patterns in rFRB 20180301A. From Luo et al., 2020.
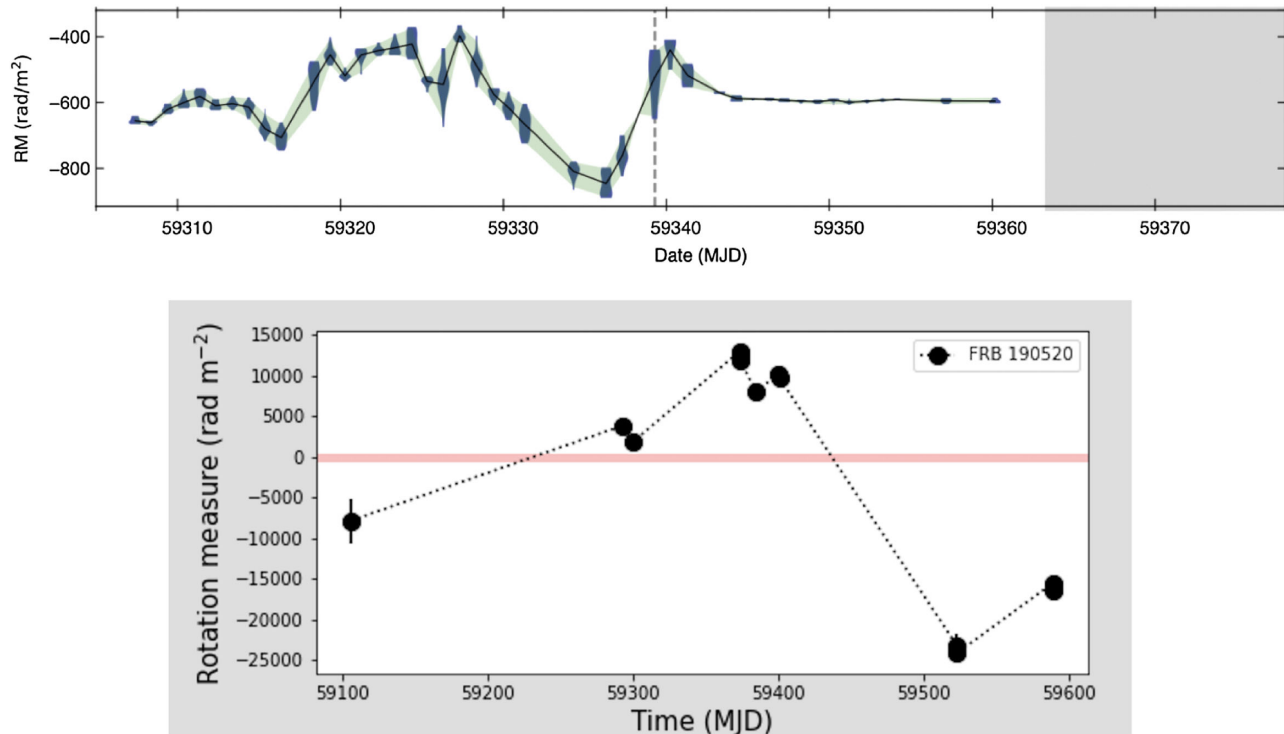
FIG. 6. Examples of short-term rotation measure (RM) variations in active repeating FRBs. Upper panel: irregular RM variations of rFRB 20201124A observed during a 54-d compaign with FAST. From Xu *et al.*, 2022. Lower panel: surprising RM reversal from rFRB 20190520B. From Anna-Thomas *et al.*, 2023.

star-formation history to a model assuming FRBs tracking compact star merger events, which experience a significant delay with respect to star formation. They found that the available Parkes or ASKAP FRBs are not inconsistent with either model. James *et al.* (2022) showed that the simple nonevolution model is inconsistent with the data and found that the star-formation model is consistent with the ASKAP data. However, they did not test models invoking delays with respect to star formation. Hashimoto *et al.* (2020) suggested that the limited data are consistent with no evolution with redshift.

With the first CHIME catalog, the FRB redshift distribution can be further constrained. Zhang and Zhang (2022) pointed out that the DM distribution peaks at a value lower than predicted by the star-formation history model and suggested that the CHIME/FRB data are consistent with a redshift model with a significant delay with respect to star formation. The conclusion was confirmed by Hashimoto *et al.* (2022) and Qiang, Li, and Wei (2022), with the former group also claiming that the data are consistent with FRBs tracking the stellar mass rather than the star-formation rate. Using a reduced sample from the CHIME catalog, Shin *et al.* (2022) found that the CHIME bursts are still consistent with following the star-formation history. However, this might be because Shin *et al.* (2022) adopted criteria to remove low DM and low S/N bursts, which have removed a significant number of nearby low-luminosity FRBs. However, the removed FRBs are the dominant population that demands a delayed redshift distribution from star formation. The existence of rFRB 20200120E in a globular cluster in M81 (Kirsten *et al.*, 2022) suggests that such burst sources

should be in abundance, which would require a significant delay in star formation.

I. Host galaxies

The first identified FRB host galaxy, that of rFRB 20121102A, is a low-metallicity, dwarf-star-forming galaxy, which is analogous to those of long-duration gamma-ray bursts (LGRBs) and superluminous supernovae (SLSNe) (Nicholl *et al.*, 2017; Tendulkar *et al.*, 2017). On the other hand, the later identified host galaxies, mostly for apparently nonrepeating FRB sources, are typically Milky Way–like massive spiral galaxies (Bannister *et al.*, 2019; Ravi *et al.*, 2019; Bhandari *et al.*, 2020; Heintz *et al.*, 2020; Marcote *et al.*, 2020). The positions of FRBs within the host galaxies also carry clues for the origin of FRB sources. Even though rFRB 20121102A is located in an active star-forming region of the host galaxy (Nicholl *et al.*, 2017; Tendulkar *et al.*, 2017), most other FRBs, especially apparently nonrepeating ones, are not. Instead, many of them lie on the outskirts of the host galaxies, with a not particularly high star-formation rate (Bhandari *et al.*, 2020; Heintz *et al.*, 2020). The active repeater rFRB 20201124A has a Milky Way–like massive host galaxy with a high star-formation rate (Fong *et al.*, 2021; Piro *et al.*, 2021; Ravi *et al.*, 2022). Detailed observations with the Keck telescopes suggested that the host galaxy is a metal-rich, barred spiral galaxy, with the FRB source residing in a low stellar density, interarm region at an intermediate galactocentric distance (Xu *et al.*, 2022). This is inconsistent with the environment expected for long GRBs and superluminous supernovae. Cross comparing the host galaxy and FRB
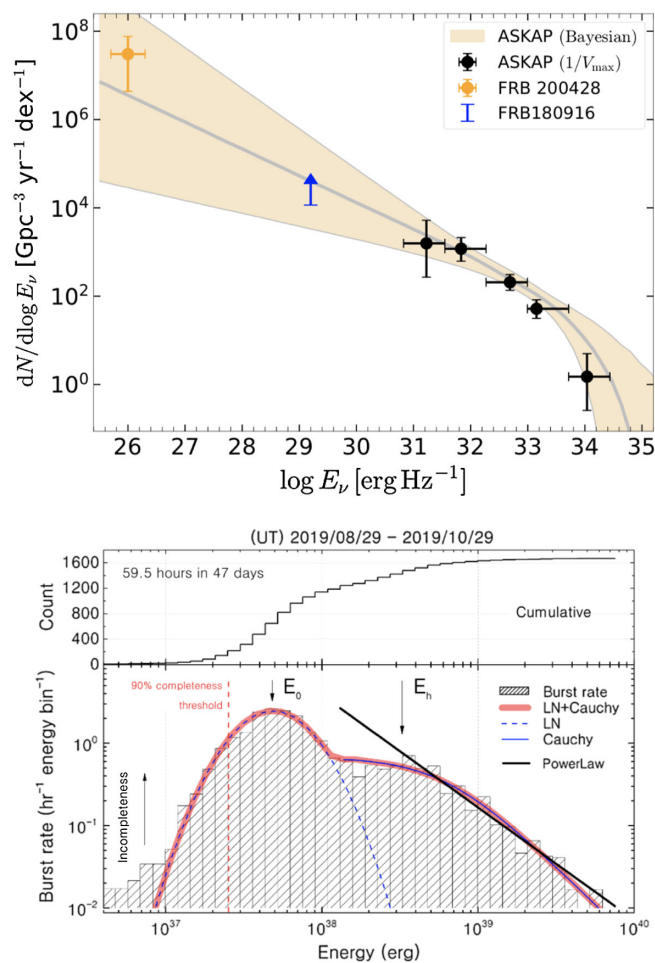
FIG. 7. Energy distribution of FRBs. Upper panel: FRB isotropic energy distribution among different sources showing a rough -1.8 power-law distribution covering at least 7 orders of magnitude. From Lu, Kumar, and Zhang, 2020. Lower panel: energy distribution of 1652 bursts detected from rFRB 20121102A showing a bimodal distribution. From D. Li et al., 2021.

position properties with other astronomical transients, Li and Zhang (2020) showed that the global properties of FRBs are inconsistent with those of LGRBs and SLSNe but are more consistent with type II SNe, and even compact object mergers. Overall, FRBs are not inconsistent with being produced by magnetar engines, even though multiple formation channels are also possible. Bochenek, Ravi, and Dong (2021) compared the host properties of FRBs and core-collapse supernovae and reached the conclusion that the FRB environments are consistent with core-collapse supernovae making magnetars.

J. Counterparts

Most FRBs do not have counterparts detected in other bands or other messenger channels (such as gravitational waves and neutrinos). Searches have been conducted, and some putative counterparts were reported but not confirmed (DeLaunay et al., 2016; Keane et al., 2016; Williams and Berger, 2016; Sakamoto et al., 2021). To date only two confirmed multiwavelength counterparts have been observed for a few sources.

First, both rFRB 20121102A (Chatterjee et al., 2017; Marcote et al., 2017) and rFRB 20190520B (C. H. Niu et al., 2022) are found to be associated with a pointlike persistent radio source (PRS). Incidently, these two sources are also active repeaters with relatively large RMs. It is suspected that all repeaters may have an associated synchrotron-emitting PRS [a supernova remnant, a magnetar wind nebula, or a mini active galactic nucleus (AGN)], but only the ones with a dense and highly magnetized environment (and thus a large RM) could be detectable (Yang, Li, and Zhang, 2020; Yang et al., 2022).

Second, the Galactic FRB 20200428 (Andersen et al., 2020; Bochenek et al., 2020) detected from the magnetar SGR J1935+2154 was associated with a contemporary hard x-ray burst (Mereghetti et al., 2020; C. K. Li et al., 2021; Ridnaia et al., 2021; Tavani et al., 2021). Searches for x-ray or γ-ray emission in association with cosmological FRBs have been carried out for multiple sources with null results (Zhang and Zhang, 2017; Cunningham et al., 2019; Yang, Zhang, and Zhang, 2019; Guidorzi et al., 2020; Piro et al., 2021; Laha et al., 2022a, 2022b; Xu et al., 2022). The nondetection is expected since the predicted x-ray flux is below the sensitivity threshold of the detectors for cosmological FRBs, even if the x-ray-to-radio luminosity ratio is the same as it is for FRB 20200428. Note that there was a stringent optical upper limit (Z-equivalent 17.9 mag in a 60-s exposure) during the prompt epoch of FRB 20200428 (Lin et al., 2020). Since the prompt optical flux is low even for the Galactic FRB, the chance of detecting a prompt optical counterpart for cosmological FRBs is slim. Recent searches have set up more upper limits in the optical band for some nearby FRBs before, during, and after the bursts (Hiramatsu et al., 2022; Niino et al., 2022). The nondetection is consistent with the expectation that the optical counterparts of FRBs are faint (Yang, Zhang, and Wei, 2019).

Searches for FRBs following some GRBs or superluminous supernovae in the timescale of years have been carried out, but with null results (Law et al., 2019; Men et al., 2019). Searches for progenitor explosions years prior to some FRBs have been also carried out, with some candidates reported (X.-G. Wang et al., 2020; Li et al., 2022).

Searches for gravitational waves (GWs) temporarily coincident with CHIME FRBs have been carried out, which has led to tight upper limits on the GW fluxes (Abbott et al., 2022; Wang and Nitz, 2022). The null results imply that at most $\mathcal{O}(0.01)\% - \mathcal{O}(1)\%$ of FRBs are associated with compact binary coalescences (CBCs), which is consistent with the much higher rate density of FRBs than of CBCs. Allowing a time difference between FRBs and GW events, a potential association pair between the NS-NS merger event GW190425 and a bright CHIME burst FRB 20190425A, with the FRB delayed by 2.5 h with respect to the GW event, has been suggested (Moroianu et al., 2022). Its candidate host galaxy and the FRB environment are consistent with those expected for a NS-NS merger (Panther et al., 2023).

III. BASIC PLASMA PHYSICS

A plasma is a gas that contains a significant fraction of charged particles, usually with charge balance between negatively charged species (free electrons) and positively

charged species (positive ions or positrons). An FRB is likely produced in a plasma and radio waves need to propagate through plasmas before reaching Earth. The discussion of the physics of FRBs inevitably involves plasma physics, which I review in this section.

A. Plasma physics in the FRB context

The most important property of a plasma is the double reaction between particles and electromagnetic (EM) fields. While the EM fields would control the motion of the plasma, the motion of the plasma would generate currents and alter EM fields. The description of the physical behavior of a plasma is therefore complicated (Kulsrud, 2005). In general one needs to solve the evolution of the particle component (i.e., each species of the plasma) in six-dimensional $(\vec{r}, \vec{v})$ phase space in the form of the Fokker-Planck equation, and to solve the EM field component in three dimensions in the form of Maxwell equations. For each particle and field component, one also needs to consider the physics in three scales: the large scale of smooth particle distribution and EM fields, the small scale of particle distribution and EM field variations due to particle collisions, and the intermediate scale variation of particle distribution and EM fields dictated by various plasma waves.

For the FRB problem, the most relevant scale is the intermediate one related to plasma waves. In many FRB radiation models, the observed FRB emission is related to certain types of plasma waves in the emission region to begin with. The microscopic particle collisional or collisionless interaction processes are usually not important in interpreting FRB observations, and I do not discuss them in the rest of the review. The largest macroscopic scale, on the other hand, could be important. This is particularly true if the emission region is from the magnetosphere of a rotating object (such as a magnetar), in which case the global magnetic field configuration and plasma density distribution play an important role in defining FRB emission properties. For models invoking relativistic shocks, the globally ordered magnetic fields also play an important role in reproducing some properties (for instance, high brightness temperature and high linear polarization degree) of FRB observations. More generally, radio waves associated with FRBs need to go through the plasmas between the source and the observer, undergoing dispersion, absorption, scattering, scintillation, and Faraday rotation and conversion for polarized emission. In the rest of the section, I discuss the basics of dispersion and Faraday rotation and conversion and leave more complicated multipath effects (such as scattering, scintillation, and plasma lensing effects) to Sec. VII.

B. Radio wave propagation in a nonmagnetized plasma

Electromagnetic waves are oscillations of electromagnetic fields in both space and time in the form of $\exp i(\vec{k} \cdot \vec{r} - \omega t)$. When waves with a particular frequency go through a stationary plasma, even though their oscillations in time (represented by angular frequency ω) remain the same as in vacuum, their oscillations in space (represented by wave number k) would be modified in a frequency-dependent

manner depending on the plasma properties. This leads to a varying wave propagation speed with frequency, known as dispersion. The relationship $\omega = \omega(k)$ is known as the dispersion relation.

The dispersion relation of EM waves propagating in a nonmagnetized, globally neutral plasma can be straightforwardly derived by introducing a space and time variation of all quantities of the form of $\exp i(\vec{k} \cdot \vec{r} - \omega t)$ in Maxwell's equations and Newton's second law equation involving the Lorentz force. The final dispersion relation reads (Rybicki and Lightman, 1979)

$$c^2 k^2 = \epsilon \omega^2, \quad ck = n_r \omega, \quad \text{or } \omega^2 = \omega_p^2 + k^2 c^2, \quad (21)$$

where

$$\epsilon \equiv n_r^2 \equiv 1 - \frac{4\pi\sigma}{i\omega} = 1 - \left(\frac{\omega_p}{\omega}\right)^2 \quad (22)$$

is the dielectric constant, n_r is the index of refraction, σ is the conductivity defined by $\vec{j} = \sigma\vec{E}$, and

$$\omega_p \equiv \left(\frac{4\pi n_e e^2}{m_e}\right)^{1/2} \simeq (5.63 \times 10^4 \text{ s}^{-1}) n_e^{1/2} \quad (23)$$

is the plasma frequency, where n_e is the plasma density and e and m_e are the charge (absolute value) and mass of the electron, respectively. Noticing that $\epsilon \geq 0$ is required to have a real solution of the dispersion relation $\omega = \omega(k)$, one can see that ω_p defines a cutoff frequency below which the EM waves cannot propagate. This is also the oscillation frequency of longitudinal waves (Langmuir waves) in a plasma.[5] If the FRB frequency (typically ~gigahertz) is related to the plasma frequency, one requires $n \simeq (1.2 \times 10^{10} \text{ cm}^{-3})\nu_{\text{FRB},9}^2$, where $\nu_{\text{FRB},9} = \nu_{\text{FRB}}/(10^9 \text{ Hz})$ and throughout the review the convention $Q_n = Q/10^n$ is adopted in centimeter-gram-second units.

The DM discussed in Sec. II.E is defined through deriving the arrival time difference of a pulse in two different spectral bands. One can start with the dispersion relation (21), which gives the group velocity of the dispersed wave as

$$v_g(\nu) \equiv \frac{\partial \omega}{\partial k} = c \left(1 - \frac{\omega_p^2}{\omega^2}\right)^{1/2}. \quad (24)$$

This gives a frequency-dependent arrival time of radio waves

$$t(\nu) = \int_0^D \frac{dl}{v_g(\nu)} \simeq \int_0^D \frac{dl}{c} \left(1 + \frac{1}{2}\frac{\omega_p^2}{\omega^2}\right), \quad (25)$$

where the approximation $\omega \gg \omega_p$ has been adopted. The arrival time difference between two frequencies $\nu_2 > \nu_1$ can be expressed as

---

[5]Note that the terms *longitudinal* ($\vec{k}\|\vec{E}$) and *transverse* ($\vec{k}\perp\vec{E}$) indicate the direction of wave propagation with respect to the electric field $\vec{E}$. EM waves are transverse waves. On the other hand, the terms *parallel* ($\vec{k}\|\vec{B}$) and *perpendicular* ($\vec{k}\perp\vec{B}$) indicate the direction of wave propagation with respect to the magnetic field $\vec{B}$.

$$\Delta t = t(\nu_1) - t(\nu_2) = \frac{e^2}{2\pi m_e c}\left(\frac{1}{\nu_1^2} - \frac{1}{\nu_2^2}\right)\text{DM}$$

$$\simeq (4.15 \text{ ms})\left(\frac{1}{\nu_{1,\text{GHz}}^2} - \frac{1}{\nu_{2,\text{GHz}}^2}\right)\frac{\text{DM}}{\text{pc cm}^{-3}}, \tag{26}$$

where

$$\text{DM} = \int_0^D n_e dl \tag{27}$$

is defined. For a cosmological source, considering that the observed time $t_{\text{obs}} = (1+z)t$ and the observed frequency $\nu_{\text{obs}} = \nu/(1+z)$, the final expression of the DM is Eq. (5) when t and ν are expressed in terms of the observed values. Defining

$$\mathcal{D} \equiv \frac{\Delta t}{\Delta(1/\nu^2)} = \frac{t_{\nu_1} - t_{\nu_2}}{1/\nu_1^2 - 1/\nu_2^2}, \tag{28}$$

one can write

$$\text{DM} = K\mathcal{D}, \tag{29}$$

where (Kulkarni, 2020)

$$K = 241.033\,178\,6(66) \text{ GHz}^{-2}\,\text{cm}^{-3}\,\text{pc s}^{-1} \tag{30}$$

and the DM is in cm^{-3} pc. Notice that many assumptions have entered the previously mentioned derivation (Kulkarni, 2020): The motion of ions is neglected and the medium is cold, not moving with respect to the observer, and not magnetized. These factors are not important if the purpose is to give a rough estimate of electron column density along the line of sight but could be essential to perform precise measurements of arrival times and cross-check the measurements of the same source using different detectors (for instance, the detection data of FRB 200428 between CHIME and STARE2).

C. Radio wave propagation in a magnetized plasma

1. General discussion

When a plasma carries an ordered magnetic field $\vec{B}$, the dispersion relation is much more complicated. Besides the plasma frequency ω_p, another characteristic frequency, the electron gyration frequency ω_B (also called the Larmor frequency ω_L), is introduced.[6] For nonrelativistic motion, this frequency depends on B and fundamental constants, i.e.,

$$\omega_B = -\Omega_e \equiv \frac{eB}{m_e c} = (1.76 \times 10^7 \text{ s}^{-1})B. \tag{31}$$

If the FRB frequency is related to ω_B, the required magnetic field strength is $B \simeq (360 \text{ G})\nu_{\text{FRB},9}$. Note that $\Omega_e = -eB/m_e c$ is defined as negative to contrast with the positive ion gyration frequency,

---

[6]The discussion in this section applies to the classical (non-quantum) plasma and wave regime.

$$\Omega_i = \frac{ZeB}{m_i c} = Z\frac{m_e}{m_i}|\Omega_e|, \tag{32}$$

where m_i is the mass of the positive ion and Z is the atomic number of the ion. For an electron-positron $(e^+ e^-)$ pair plasma, one has $\Omega_i = |\Omega_e| = \omega_B$.

The existence of $\vec{B}$ introduces another special direction besides the wave propagation direction

$$\vec{n}_r = \frac{c}{\omega}\vec{k}. \tag{33}$$

The dispersion relation becomes angle dependent. Repeating the exercise of wave expansion for the Maxwell's equations and Lorentz force equation for a global neutral plasma, one gets a dielectric tensor to replace the dielectric constant, which reads (Mészáros, 1992; Stix, 1992; Boyd and Sanderson, 2003)

$$\overleftrightarrow{\epsilon} \equiv \begin{pmatrix} S & -iD & 0 \\ iD & S & 0 \\ 0 & 0 & P, \end{pmatrix}. \tag{34}$$

This is defined from

$$\vec{n}_r \times (\vec{n}_r \times \vec{E}) = -\overleftrightarrow{\epsilon} \cdot \vec{E} \tag{35}$$

(which itself comes from the fourth Maxwell equation $\vec{j} = \overleftrightarrow{\sigma} \cdot \vec{E}$, where $\overleftrightarrow{\sigma}$ is the conductivity tensor, $\overleftrightarrow{\epsilon}$ is defined as $\overleftrightarrow{\epsilon} = \overleftrightarrow{I} - 4\pi\overleftrightarrow{\sigma}/i\omega$, and $\overleftrightarrow{I}$ is the unit tensor), where $\vec{E}$ is the electric field vector of the waves and the magnetic field direction is defined as the $\hat{z}$ direction. In Eq. (34)

$$S = \frac{1}{2}(R+L) = 1 - \frac{\omega_p^2(\omega^2 + \Omega_i\Omega_e)}{(\omega^2 - \Omega_i^2)(\omega^2 - \Omega_e^2)}, \tag{36}$$

$$D = \frac{1}{2}(R-L) = \frac{\omega_p^2\omega(\Omega_i + \Omega_e)}{(\omega^2 - \Omega_i^2)(\omega^2 - \Omega_e^2)}, \tag{37}$$

$$R = 1 - \frac{\omega_p^2}{(\omega + \Omega_i)(\omega + \Omega_e)}, \tag{38}$$

$$L = 1 - \frac{\omega_p^2}{(\omega - \Omega_i)(\omega - \Omega_e)}, \tag{39}$$

$$P = 1 - \frac{\omega_p^2}{\omega^2}, \tag{40}$$

where R, L, and P denote parameters related to the right, left, and plasma modes, respectively, and S and D denote the sum and difference, respectively.

Generally $\vec{n}_r$ and $\vec{B}$ can contain an angle θ. One can write $\vec{n}_r = (n_r \sin\theta, 0, n_r \cos\theta)$ without loss of generality such that Eq. (35) becomes $(\vec{n}_r \cdot \vec{E})\vec{n}_r - n_r^2\vec{E} + \overleftrightarrow{\epsilon} \cdot \vec{E} = 0$ or

$$\begin{pmatrix} S - n_r^2 \cos^2\theta & -iD & n_r^2 \cos\theta\sin\theta \\ iD & S - n_r^2 & 0 \\ n_r^2 \cos\theta\sin\theta & 0 & P - n_r^2 \sin^2\theta \end{pmatrix} \begin{pmatrix} E_x \\ E_y \\ E_z \end{pmatrix} = 0. \quad (41)$$

Taking the determinant of the coefficients, the general dispersion relation for waves propagating in a cold, magnetized plasma becomes

$$A n_r^4 - B n_r^2 + C = 0, \quad (42)$$

where

$$A = S \sin^2\theta + P \cos^2\theta, \quad (43)$$

$$B = RL \sin^2\theta + PS(1 + \cos^2\theta), \quad (44)$$

$$C = PRL. \quad (45)$$

In the following, I consider the dispersion relations for a cold, magnetized plasma for different cases of the angle between $\vec{k}$ (or $\vec{n}_r$) and $\vec{B}$:

2. $\vec{k} \| \vec{B}$

When the wave vector is along the magnetic field (such as for FRB waves propagating in the open field line region of a magnetosphere), Eq. (41) becomes

$$\begin{pmatrix} S - n_r^2 & -iD & 0 \\ iD & S - n_r^2 & 0 \\ 0 & 0 & P \end{pmatrix} \begin{pmatrix} E_x \\ E_y \\ E_z \end{pmatrix} = 0. \quad (46)$$

Besides the $P = 0$ plasma mode ($\omega^2 = \omega_p^2$), one has two transverse wave modes, i.e., the R and L modes,[7]

$$n_r^2 = R, \quad R \text{ mode}, \quad (47)$$

$$n_r^2 = L, \quad L \text{ mode}, \quad (48)$$

with the dispersion relations

$$\frac{c^2 k^2}{\omega^2} = R \simeq \begin{cases} 1 - \omega_p^2/\omega(\omega - \omega_B), & \text{ion}, \\ 1 - \omega_p^2/(\omega^2 - \omega_B^2), & \text{pair}, \end{cases} \quad R \text{ mode}, \quad (49)$$

$$\frac{c^2 k^2}{\omega^2} = L \simeq \begin{cases} 1 - \omega_p^2/\omega(\omega + \omega_B), & \text{ion}, \\ 1 - \omega_p^2/(\omega^2 - \omega_B^2), & \text{pair}, \end{cases} \quad L \text{ mode}, \quad (50)$$

respectively. Note that hereafter for a pair plasma the plasma frequency is defined as

---

[7]Notice that opposite conventions of R- and L-mode definitions have been used in some of the literature. For example, Boyd and Sanderson (2003) defined right handed and left handed with respect to the photon propagation direction, while Rybicki and Lightman (1979) defined right handed and left handed with respect to the line-of-sight direction toward the source. I adopt the Boyd and Sanderson (2003) convention in the following discussion.

$$\omega_p \equiv \left(\frac{4\pi n_\pm e^2}{m_e} \right)^{1/2} \simeq (5.63 \times 10^4 \text{ s}^{-1}) n_\pm^{1/2}, \quad (51)$$

in contrast to Eq. (23), where $n_\pm = 2n_e$ is the pair number density, which is 2 times n_e for a neutral pair plasma. If one still uses the electron number density n_e to define ω_p, all the pair-related dispersion relations should have ω_p^2 replaced by $2\omega_p^2$. This is because in Eqs. (36) and (40) a small term $\omega_{p,i}^2 = 4\pi n_e (Ze)^2/m_i$ in parallel to ω_p^2 has been ignored. This term becomes comparable to $\omega_{p,e}^2$ in the case of pairs.

Setting $R = 0$ and $L = 0$ and looking for positive solutions,[8] one can define two cutoff frequencies,

$$\omega_R \equiv \left[\omega_p^2 + \frac{(\Omega_i - \Omega_e)^2}{4} \right]^{1/2} - \frac{(\Omega_i + \Omega_e)}{2}$$

$$\simeq \begin{cases} (\omega_p^2 + \omega_B^2/4)^{1/2} + \omega_B/2, & \text{ion}, \\ (\omega_p^2 + \omega_B^2)^{1/2}, & \text{pair}, \end{cases} \quad (52)$$

and

$$\omega_L \equiv \left[\omega_p^2 + \frac{(\Omega_i - \Omega_e)^2}{4} \right]^{1/2} + \frac{\Omega_i + \Omega_e}{2}$$

$$\simeq \begin{cases} (\omega_p^2 + \omega_B^2/4)^{1/2} - \omega_B/2, & \text{ion}, \\ (\omega_p^2 + \omega_B^2)^{1/2}, & \text{pair}, \end{cases} \quad (53)$$

respectively. In Eqs. (52) and (53), $\Omega_i \ll |\Omega_e|$ and $\Omega_i = |\Omega_e|$ ($Z = 1$) have been adopted for an ion plasma and a pair plasma, respectively. The propagation condition for the R-mode and L-mode waves depends on the sign of the denominators in Eqs. (38) and (39), respectively.

Setting $R \to \infty$ and $L \to \infty$, one can define principle resonances at $\omega_{\text{res},R} = |\Omega_e| = \omega_B$ and $\omega_{\text{res},L} = \Omega_i$. The frequency range in which radio waves can propagate is defined by $n_r^2 > 0$, which is

$$\omega > \omega_R \quad \text{or} \quad \omega < \omega_B, \quad R \text{ mode}, \quad (54)$$

$$\omega > \omega_L \quad \text{or} \quad \omega < \Omega_i, \quad L \text{ mode}. \quad (55)$$

Now consider the following two asymptotic regimes:

- In the regions far from the magnetosphere of a neutron star [for instance, in the interstellar medium (ISM) or IGM], one has $\omega \gg \omega_B \, \omega_p \gg \omega_B$ and $|\Omega_e| \gg \Omega_i$. In this case, one has $\omega_R \simeq \omega_L \simeq \omega_p$. The wave propagation condition is $\omega > \omega_p$ for both the R and L modes, which is essentially the same as a nonmagnetized medium.
- In the regions within a neutron star magnetosphere and for a pair plasma, one has $\omega \ll \omega_B$, $\omega_p \ll \omega_B$, and $|\Omega_e| = \Omega_i = \omega_B$. In this case, one has $\omega_R \simeq \omega_L \simeq (\omega_p^2 + \omega_B^2)^{1/2} \simeq \omega_B$ and the resonances are also ω_B. The

---

[8]Negative frequencies simply mean waves propagating in the opposite direction. Therefore, solving positive solutions is complete in solving the propagation problem.

R mode and the L mode become the same and are essentially transparent at all frequencies.

3. $\vec{k} \perp \vec{B}$

In another extreme case in which the wave vector is perpendicular to the magnetic field (such as for FRB waves propagating in the closed field line region of a magnetosphere), Eq. (41) becomes

$$
\begin{pmatrix} S & -iD & 0 \\ iD & S - n_r^2 & 0 \\ 0 & 0 & P - n_r^2 \end{pmatrix} \begin{pmatrix} E_x \\ E_y \\ E_z \end{pmatrix} = 0. \tag{56}
$$

One can also define two modes: the ordinary (O) and the extraordinary (X or E) modes, i.e.,

$$
n_r^2 = P, \qquad O \text{ mode}, \tag{57}
$$

$$
n_r^2 = \frac{RL}{S}, \qquad X \text{ mode}, \tag{58}
$$

with the O-mode dispersion relation

$$
\frac{c^2 k^2}{\omega^2} = P = 1 - \frac{\omega_p^2}{\omega^2} \tag{59}
$$

and the X-mode dispersion relation

$$
\frac{c^2 k^2}{\omega^2} = \frac{RL}{S}
$$
$$
\simeq \begin{cases} [(\omega^2 - \omega_p^2)^2 - \omega^2 \omega_B^2]/\omega^2(\omega^2 - \omega_p^2 - \omega_B^2), & \text{ion,} \\ 1 - \omega_p^2/(\omega^2 - \omega_B^2), & \text{pair,} \end{cases} \tag{60}
$$

respectively. The O mode corresponds to the case that the wave electric field vector is parallel to the background magnetic field vector, i.e., $\vec{E}_w \| \vec{B}$, so electrons moving in response to $\vec{E}_w$ oscillations do not feel the existence of the $\vec{B}$ field. As a result, the dispersion relation is the same as the nonmagnetized medium case, and hence the mode is called ordinary. The X mode corresponds to the case of $\vec{E}_w \perp \vec{B}$. The electrons in response to $\vec{E}_w$ oscillations would also undergo gyration motion around the background $\vec{B}$ field; hence, the mode is called extraordinary. The X mode has cutoffs ($k \to 0$) at ω_R ($R = 0$) and ω_L ($L = 0$) and principle resonances ($k \to \infty$) at $S = 0$, which defines two hybrid resonance frequencies (upper and lower)

$$
\omega_{\text{res,H}}^2 = \left(\frac{\omega_p^2 + \Omega_i^2 + \Omega_e^2}{2} \right)
$$
$$
\times \left[1 \pm \left(1 + \frac{4\Omega_i \Omega_e (\omega_p^2 - \Omega_i \Omega_e)}{(\omega_p^2 + \Omega_i^2 + \Omega_e^2)^2} \right)^{1/2} \right]. \tag{61}
$$

For an ion plasma, since $\Omega_e^2 \gg \Omega_i^2$, the second term in the square root is always $\ll 1$. One therefore has

$$
\omega_{\text{res,UH}}^2 \simeq \omega_p^2 + \Omega_e^2, \tag{62}
$$

$$
\omega_{\text{res,LH}}^2 \simeq -\frac{\Omega_i \Omega_e (\omega_p^2 - \Omega_i \Omega_e)}{\omega_p^2 + \Omega_i^2 + \Omega_e^2}. \tag{63}
$$

For an $e^\pm$ plasma with $\Omega_e^2 = \Omega_i^2 = \omega_B^2$, one has

$$
\omega_{\text{res,UH}}^2 = \omega_p^2 + \omega_B^2, \tag{64}
$$

$$
\omega_{\text{res,LH}}^2 = \omega_B^2. \tag{65}
$$

The frequency range in which radio waves can propagate ($n_r^2 > 0$) is

$$
\omega > \omega_p, \qquad O \text{ mode}, \tag{66}
$$

$$
\begin{cases} \omega > \omega_R, \\ \omega_L < \omega < \omega_{\text{res,UH}}, \qquad X \text{ mode}, \\ \text{or } \omega < \omega_{\text{res,LH}}. \end{cases} \tag{67}
$$

One can again consider two asymptotic regimes:

- In regions far from the magnetosphere of a neutron star (such as in the ISM or IGM), one has $\omega \gg \omega_B$, $\omega_p \gg \omega_B$, and $|\Omega_e| \gg \Omega_i$. In this case, one has $\omega_R \simeq \omega_{\text{res,UH}}$, $\omega_L \simeq \omega_p$, and $\omega_{\text{res,LH}} \simeq \omega_B$. The wave propagation condition is $\omega > \omega_p$ for both the O and X modes, which is essentially the same as a non-magnetized medium.

- In regions within a neutron star magnetosphere and for a pair plasma, one has $\omega \ll \omega_B$, $\omega_p \ll \omega_B$, and $|\Omega_e| = \Omega_i = \omega_B$. In this case, one has $\omega_R \simeq \omega_{\text{res,UH}} \simeq \omega_L \simeq (\omega_p^2 + \omega_B^2)^{1/2} \simeq \omega_B$ and $\omega_{\text{res,LH}} = \omega_B$. Thus, the X mode is essentially transparent in all frequencies. The O mode, however, can propagate only when $\omega > \omega_p$. Because of this, when radio waves propagate across the closed field line regions of a neutron star, the X-mode $\vec{E}_w$ vector would adiabatically rotate to remain perpendicular to the local $\vec{B}$ until reaching the radius where $\omega > \omega_p$ is satisfied, at which point the polarization vector is frozen out (Lu, Kumar, and Narayan, 2019).

4. Oblique propagation

When $\langle \vec{k}, \vec{B} \rangle = \theta$ has an arbitrary angle, the dispersion relation should take the form of Eq. (41), which is more complicated; see Stix (1992) and Boyd and Sanderson (2003) for details. Nonetheless, the treatments in the two extreme cases are helpful for discussing the general behavior of the dispersion relations when θ is small or close to $\pi/2$:

- When $\theta \ll 1$, one has the quasiparallel case. The dispersion relations can be modified from the R- and L-mode relations [Eqs. (49) and (50)] by replacing ω_B with $\omega_B \cos\theta$.

- When $\theta \to \pi/2$, one has the quasiperpendicular case. The O-mode dispersion relation is revised to

$$\frac{c^2 k^2}{\omega^2} \simeq \frac{\omega^2 - \omega_p^2}{\omega^2 - \omega_p^2 \cos^2 \theta}, \qquad (68)$$

which can be reduced to Eq. (59) when $\theta = \pi/2$. The X-mode dispersion relation can be modified directly from Eq. (60) by replacing ω_B with $\omega_B \sin \theta$.

In the literature, for the oblique cases the X and O modes are usually defined as cases in which $\vec{E}_w$ is perpendicular and parallel to the $(\vec{k}, \vec{B})$ plane, respectively. Note that the O mode defined in this way is not completely ordinary, since there is still a $\vec{E}_w$ component that is perpendicular to $\vec{B}$. One must be cautious to extend the properties of the O mode in the $\vec{k} \perp \vec{B}$ case to the more general O mode. For example, the statement that an O mode cannot propagate in a neutron star magneto-pshere is valid only in the quasiperpendicular regime. In the quasiparallel regime, even the O mode is essentially extraordinary, i.e., a significant $\vec{E}_w$ component is perpendicular to $\vec{B}$. The waves can therefore also propagate.

D. Faraday rotation

We now take a closer look at the propagation of radio waves in the case of $\vec{k} \parallel \vec{B}$ in an ion plasma. Removing Ω_i, the R- $(L$-) mode dispersion relations [Eqs. (49) and (50)] can generally be written as

$$\omega^2 = k^2 c^2 + \frac{\omega_p^2}{1 \mp \omega_B/\omega} \simeq k^2 c^2 + \omega_p^2 \left(1 \pm \frac{\omega_B}{\omega}\right), \qquad (69)$$

where the $\omega_B \ll \omega$ approximation has been adopted in the second equation, which is usually valid for the ISM and the IGM.

Following the same procedure in Sec. III.B and replacing ω_p^2 with $\omega_p^2 (1 \pm \omega_B/\omega)$ (again valid for $\omega_B \ll \omega$), one gets

$$v_g(\nu) = c \left[1 - \frac{\omega_p^2}{\omega^2} \left(1 \pm \frac{\omega_B}{\omega}\right)\right]^{1/2}. \qquad (70)$$

Further requiring $\omega_p \ll \omega$, one can derive

$$t(\nu) \simeq \int_0^D \frac{dl}{c} \left[1 + \frac{1}{2} \frac{\omega_p^2}{\omega^2} \left(1 \pm \frac{\omega_B}{\omega}\right)\right] \qquad (71)$$

and

$$\Delta t = t(\nu_1) - t(\nu_2)$$
$$= \frac{e^2}{2\pi m_e c} \left(\frac{1}{\nu_1^2} - \frac{1}{\nu_2^2}\right) DM \pm \frac{e^3}{(2\pi m_e c)^2} \left(\frac{1}{\nu_1^3} - \frac{1}{\nu_2^3}\right) \int_0^D n_e B_\parallel dl$$
$$\simeq (4.15 \text{ ms}) \left(\frac{1}{\nu_{1,\text{GHz}}^2} - \frac{1}{\nu_{2,\text{GHz}}^2}\right) \frac{DM}{\text{pc cm}^{-3}}$$
$$\pm (1.16 \times 10^{-11} \text{ s}) \left(\frac{1}{\nu_{1,\text{GHz}}^3} - \frac{1}{\nu_{2,\text{GHz}}^3}\right) \frac{\int_0^D n_e B_\parallel dl}{\text{pc cm}^{-3} \, \mu\text{G}}. \qquad (72)$$

One can see that the effect of the B field in the arrival time has a ν^{-3} dependence that is much smaller than the DM term. It

depends on $\int_0^D n_e B_\parallel dl$ (a proxy of the rotation measure discussed later), but this term is practically not measurable.

A measurement of $\int_0^D n_e B_\parallel dl$ is achievable by measuring the rotation of the PA of linearly polarized waves as a function of frequency known as Faraday rotation. Since linearly polarized waves can be decomposed as the superposition of right-handed and left-handed circularly polarized components and since the two modes (the R and L modes) have different propagation speeds, the PA of the observed waves would display a frequency-dependent variation. Mathematically this can be denoted as the variation of the phase difference of the circularly polarized waves as a function of frequency. Noticing that $k_R^2 c^2 = R\omega^2$, $k_L^2 c^2 = L\omega^2$ and that the phases of the R- and L-mode waves $\phi_{R,L} = \int_0^D k_{R,L} dl$, the rotation angle can be written as

$$\Delta\phi = \frac{1}{2} \int_0^D (k_L - k_R) dl$$
$$\simeq -\frac{1}{2} \int_0^D \frac{\omega_p^2 \omega_B}{c\omega^2} dl$$
$$\simeq -\frac{e^3 \lambda^2}{2\pi m_e^2 c^4} \int_0^D n_e B_\parallel dl$$
$$= \lambda^2 \text{RM}, \qquad (73)$$

where

$$\text{RM} \equiv -\frac{e^3}{2\pi m_e^2 c^4} \int_0^D n_e B_\parallel dl$$
$$\simeq (-0.81 \text{ rad m}^{-2}) \frac{\int_0^D n_e B_\parallel dl}{\text{pc cm}^{-3} \, \mu\text{G}}. \qquad (74)$$

For cosmological sources, the observed wavelength is $\lambda = (1 + z)\lambda_{\text{sr}}$, so a more general expression is Eq. (19).

E. Faraday conversion

More generally, Faraday rotation is a special case of "Faraday conversion." In general a polarized electromagnetic wave can be characterized by four Stokes parameters (Rybicki and Lightman, 1979),

$$I = \varepsilon_0^2, \qquad (75)$$

$$Q = \varepsilon_0^2 \cos 2\psi \cos 2\chi, \qquad (76)$$

$$U = \varepsilon_0^2 \cos 2\psi \sin 2\chi, \qquad (77)$$

$$V = \varepsilon_0^2 \sin 2\psi, \qquad (78)$$

where $I = \sqrt{Q^2 + U^2 + V^2}$ is the total intensity, $L = \sqrt{Q^2 + U^2}$ is the intensity of the linear polarization, V is the intensity of the circular polarization, $\varepsilon_0 = \sqrt{I}$ is the amplitude of the elliptically polarized EM waves, $\psi = (1/2) \arcsin(V/I)$ is a proxy of the circular polarization degree $\Pi_o = V/I$ that is intrinsic to the waves, and $\chi = (1/2) \arctan(U/Q)$ is the angle between the semimajor axis of the ellipse and the x axis defined by the telescope, which is

extrinsic to the waves. Notice that I, 2ψ, and 2χ are spherical coordinates in a imaginary Poincaré sphere and Q, U, and V define a polarization vector $\vec{P}$ from the center to a point on the sphere in the Cartesian coordinate system, which defines the polarization state of the wave. Faraday rotation is simply the rotation of the $\vec{P}$ vector around the V axis. When $\vec{P}$ rotates around axes other than the V axis, there is conversion between the linear polarization L and the circular polarization V. The waves undergo Faraday conversion (Zheleznyakov and Zlotnik, 1964; Melrose, Robinson, and Feletto, 1995).

The physics of Faraday conversion can be understood as follows. Any polarization state can be decomposed into a superposition of two fundamental modes, either two circular polarization modes (for instance, R and L modes) for the quasiparallel case or two linear polarization modes (for instance, O and X modes) for the quasiperpendicular case. The different phase velocities of the two eigenmodes would make the two modes out of phase and introduce modified polarization behaviors after superposition. For the quasiparallel case, the different velocities of the R and L modes introduce rotation of the superposed linear polarization angle, and hence the Faraday rotation. For the quasiperpendicular case, on the other hand, the difference in the propagation velocities in the O and X modes would put the two modes out of phase, making the superposed polarization elliptical. Effectively, part of linear polarization is converted to circular polarization. The amplitude of Faraday conversion is smaller than that of Faraday rotation by a factor of ω_B/ω, which is $\ll 1$ for waves propagating in a medium far outside the neutron star magnetosphere.

Mathematically one can consider that the vector $\vec{P}$ undergoes rotation around an imaginary vector axis in the direction of

$$\vec{\Omega} \equiv (g, h, f) \tag{79}$$

on the Poincaré sphere. The variation of the circular polarization degree can be described by $d\vec{P}/dz = \vec{\Omega} \times \vec{P}$, where the z axis is the direction of the V component (Gruzinov and Levin, 2019). The three components of $\vec{\Omega}$ are

$$f = -\frac{1}{c}\frac{\omega_p^2 \omega_B}{\omega^2}\hat{B}_z, \tag{80}$$

$$h + ig = -\frac{1}{c}\frac{\omega_p^2 \omega_B^2}{\omega^3}(\hat{B}_x + i\hat{B}_y)^2, \tag{81}$$

where $(\hat{B}_x, \hat{B}_y, \hat{B}_z)$ is the unit vector $\hat{B} = \vec{B}/B$, f denotes the traditional Faraday rotation rate discussed in Eq. (73), and $h + ig$ describes the Faraday conversion rate. To order of magnitude, one can see that $h/f \sim g/f \sim \omega_B/\omega$, which is $\ll 1$ for waves propagating far outside a neutron star magnetosphere. This means that $\vec{\Omega}$ is essentially parallel to the V direction and that Faraday conversion is a small-order effect compared to Faraday rotation.

When measuring oscillations of the Stokes parameter V, one can define a conversion measure (CM) as (Gruzinov and Levin, 2019)

$$\langle \Pi_V \rangle = \lambda^2 \text{CM}, \tag{82}$$

where $\Pi_V \equiv |V|/I$ and $\langle \Pi_V \rangle$ is the rms value of Π_V. The CM can be related to the RM through

$$\text{CM} \simeq \frac{\omega_B}{\omega}\text{RM}^{1/2} \sim (10^{-2} \text{ m}^{-2})\text{RM}_m^{1/2}(B/G), \tag{83}$$

where B is in gauss and RM is in rad m^{-2}. This is strictly valid for a small conversion angle θ_f (the final angle by which the linear polarization Q-U plane rotates). For a large θ_f, a more precise expression is (Gruzinov and Levin, 2019)

$$\langle \Pi_V \rangle = \sqrt{2[e^{-(\text{CM}\lambda^2)^2/2} - e^{(\text{CM}\lambda^2)^2}]}. \tag{84}$$

When both the CM and the RM are measured, one can directly measure B using Eq. (83).

Physically for a cold plasma Faraday conversion happens when the B field is quasiperpendicular. Astrophysically, this may be (but is not necessarily) related to the reversal of $B_\parallel$ along the line of sight (Melrose, 2010; Gruzinov and Levin, 2019). Another possibility of having Faraday conversion is when electrons are no longer "cold" but are mildly relativistic with a mean Lorentz factor $\gamma_e > 3$. This is because, when considering the response tensor or electrons with a general energy distribution, the expressions of the h, g, and f parameters depend on γ_e in the medium (Huang and Shcherbakov, 2011). As γ_e increases, h and g increase and f decreases such that conversion becomes progressively more important and rotation becomes less important. The non-detection of Faraday conversion in rFRB 20121102A was used by Vedantham and Ravi (2019) to place an upper limit on the Lorentz factor of the electrons in the medium that generate the conversion, i.e., $\gamma_e < 5$.

Faraday conversion can be more generally described using the transport equation (Huang and Shcherbakov, 2011; Li et al., 2023)

$$\frac{d\vec{S}}{ds} = \begin{pmatrix} \epsilon_I \\ \epsilon_L \\ 0 \\ \epsilon_V \end{pmatrix} - \begin{pmatrix} \eta & \eta_L & 0 & \eta_V \\ \eta_L & \eta & \rho_V & 0 \\ 0 & -\rho_V & \eta & \rho_L \\ \eta_V & 0 & -\rho_L & \eta \end{pmatrix}\vec{S} \tag{85}$$

for the Stokes vector

$$\vec{S} = \begin{pmatrix} I \\ Q \\ U \\ V \end{pmatrix} = \begin{pmatrix} I \\ L \\ 0 \\ V \end{pmatrix}, \tag{86}$$

where in the second equation I have replaced Q with L by adopting a coordinate system with $U = 0$ without loss of generality. In Eq. (85) ϵ is the emission coefficient, η is the absorption coefficient, ρ_V [the same as the f parameter in Eq. (80)] is the coefficient for Faraday rotation, and ρ_L

[essentially the amplitude of $h + ig$ in Eq. (81)] is the coefficient for Faraday conversion.

Apparent oscillations of L and V have been discovered in some bursts from rFRB 20201124A (Xu *et al.*, 2022). These features can be interpreted as Faraday conversion or polarization-dependent absorption, which in any case demands a complex magnetized environment around the source (Xu *et al.*, 2022; Li *et al.*, 2023).

F. Plasma radiation mechanisms

In classical electrodynamics, charged particles radiate when undergoing acceleration. I now discuss three well-known radiation mechanisms involving electron acceleration in electric fields, magnetic fields, and electromagnetic waves, respectively.

1. Bremsstrahlung

An electron in the Coulomb electric field of an ion would radiate through bound-bound (line emission), free-bound (recombination), and free-free (*bremsstrahlung*) processes. The opposite processes give respective absorption processes of the photons.

For a plasma in thermal equilibrium with temperature T, the plasma thermal bremsstrahlung (free-free) emissivity reads (Rybicki and Lightman, 1979)

$$
\begin{aligned}
\epsilon_\nu^{\text{ff}} &\equiv \frac{dE}{dV dt d\nu} \\
&= \frac{2^5 \pi e^6}{3 m_e c^3} \left(\frac{2\pi}{3 k_B m_e T} \right)^{1/2} Z^2 n_e n_i e^{-h\nu/k_B T} \bar{g}_{\text{ff}} \\
&= (6.8 \times 10^{-38} \text{ erg cm}^{-3} \text{ s}^{-1} \text{ Hz}^{-1}) Z^2 n_e n_i T^{-1/2} e^{-h\nu/k_B T} \bar{g}_{\text{ff}},
\end{aligned}
\tag{87}
$$

where c, k_B, e, and m_e are standard fundamental constants, T is the gas temperature, n_i is the number density of ions, Z is the atomic number of the ions, and $\bar{g}_{\text{ff}}$ is the Gaunt factor. The reason for the factor $n_e n_i$ is that the emissivity of each electron depends on the number density of ions, and the total emissivity is proportional to the number density of the electrons. Since $Z n_i = n_e$ is needed to maintain charge neutrality, n_e^2 enters the problem, so an *emission measure*

$$
\text{EM} = \int_0^D n_e^2 dl
\tag{88}
$$

can be defined for a radio source, which may be related to the DM of the source through $\text{EM} L \sim \text{DM}^2$, where L is the characteristic size of the source.

The opposite process of bremsstrahlung, i.e., free-free absorption, is relevant to constrain the physical condition to allow FRBs with extremely high brightness temperatures to be observed. The absorption coefficient can be expressed as (Rybicki and Lightman, 1979)

$$
\begin{aligned}
\alpha_\nu^{\text{ff}} &= \frac{4e^6}{3 m_e h c} \left(\frac{2\pi}{3 k_B m_e T} \right)^{1/2} Z^2 n_e n_i \nu^{-3} (1 - e^{-h\nu/k_B T}) \bar{g}_{\text{ff}} \\
&= (3.7 \times 10^8 \text{ cm}^{-1}) Z^2 n_e n_i T^{-1/2} \nu^{-3} (1 - e^{-h\nu/k_B T}) \bar{g}_{\text{ff}}
\end{aligned}
\tag{89}
$$

or, in the Rayleigh-Jeans regime,

$$
\begin{aligned}
\alpha_\nu^{\text{ff}} &= \frac{4e^6}{3 m_e k c} \left(\frac{2\pi}{3 k_B m_e} \right)^{1/2} T^{-3/2} Z^2 n_e n_i \nu^{-2} \bar{g}_{\text{ff}} \\
&= (0.0018 \text{ cm}^{-1}) T^{-3/2} Z^2 n_e n_i \nu^{-2} \bar{g}_{\text{ff}}.
\end{aligned}
\tag{90}
$$

Integrating over distance, one gets the optical depth for free-free absorption (Cordes and Lazio, 2002)

$$
\begin{aligned}
\tau_\nu^{\text{ff}} &= \int_0^D \alpha_\nu^{\text{ff}} dl \\
&= (5.47 \times 10^{-8}) T_4^{-3/2} Z^2 \nu_9^{-2} \bar{g}_{\text{ff}} \frac{\text{EM}}{\text{pc cm}^{-6}}.
\end{aligned}
\tag{91}
$$

An FRB is transparent only if $\tau_\nu^{\text{ff}} < 1$ is satisfied both in the emission region and in the local environment surrounding the FRB source.

For a relativistically hot plasma, the emissivity and absorption coefficient should be multiplied by a correction factor. The frequency-integrated correction factor is $1 + AT$, where $A = 4.4 \times 10^{-10} \text{ K}^{-1}$ (Rybicki and Lightman, 1979).

2. Cyclotron, synchrotron, and curvature radiation mechanisms

Electrons gyrate in magnetic fields and radiate. For non-relativistic electrons, the emitted *cyclotron radiation* spectrum is linelike, with the main power at the Larmor frequency ω_B and progressively lower powers at its higher harmonics.

A relativistic electron with the Lorentz factor γ_e radiates *synchrotron radiation* with a characteristic radiation frequency (Rybicki and Lightman, 1979)

$$
\omega_{\text{SR}} \simeq \frac{3}{2} \gamma_e^2 \frac{eB}{m_e c} \sin \alpha,
\tag{92}
$$

where α is the pitch angle between the electron velocity and the magnetic field. The power 2 for γ_e is due to the following three factors: (1) the relativistic mass is larger by a factor of γ_e; (2) the fraction of the orbital time with radiation beamed toward an observer is smaller by a factor of $2/\gamma_e$ due to the relativistic beaming effect; and (3) the observed timescale is shorter than the emission timescale by roughly a factor of $1 - \beta \sim 1/(2\gamma_e^2)$, where β is the dimensionless speed of the electron. If synchrotron radiation is responsible for the FRB emission (for instance, within the framework of the synchrotron maser model), the required condition is $\gamma_e^2 B \sin \alpha \simeq (360 \text{ G}) \nu_{\text{FRB},9}$.

The relativistic beaming effect for synchrotron radiation is valid under the vacuum approximation. In a plasma, with the refraction index $n_r \equiv \sqrt{\epsilon} < 1$, the beaming angle θ_b becomes $\sqrt{1 - n_r^2 \beta^2}$ rather than $\sqrt{1 - \beta^2}$. If n_r deviates from unity much more than β, one has $\theta_b \sim \sqrt{1 - n_r^2} = \omega_p / \omega$ and synchrotron radiation is suppressed (Rybicki and Lightman, 1979). One can define the Razin frequency by equating θ_b and $1/\gamma_e$, which gives

$$
\omega_{\text{Razin}} = \gamma_e \omega_p.
\tag{93}
$$

Synchrotron radiation is suppressed when $\omega < \omega_{\text{Razin}}$. Matching the Razin frequency with gigahertz, the condition is $\gamma_e^2 n_e \simeq (1.2 \times 10^{10} \text{ cm}^{-3}) \nu_{\text{FRB},9}^2$.

In a strong magnetic field environment such as the magnetosphere of a pulsar or a magnetar, the synchrotron cooling timescale $t_{c,SR} \sim \gamma_e m_e c^2/[(4/3)\gamma_e^2 \beta_e^2 c \sigma_T (B^2/8\pi)] \sim (8 \times 10^{-20} \text{ s})B_{12}^{-2}\gamma_{e,2}^{-2}$ is extremely short. As a result, charged particles stay at the lowest Landau level and essentially slide along the magnetic field lines in the local inertial (corotating) frame. Since the field lines are usually curved, particles will radiate when they accelerate in the curved trajectory. The characteristic frequency of such *curvature radiation* can be calculated by replacing the electron gyration radius in the synchrotron radiation formula with the curvature radius ρ of the field lines such that

$$\omega_{CR} = \frac{3}{2}\gamma_e^3 \frac{c}{\rho}. \tag{94}$$

The origin of γ_e^3 is similar to that of synchrotron radiation, except that there is no $\gamma_e m_e$ suppression in gyration frequency as is the case of synchrotron radiation (the mass does not enter into the problem, since the curvature radius of the field line does not depend on the mass). To match the gigahertz emission, the parameters should satisfy $\gamma_{e,2}^3 \rho_7^{-1} \simeq 1.4\nu_{FRB,9}$.

3. Compton and inverse Compton scattering

An initially at-rest electron oscillates in electromagnetic waves and emits essentially isotropically at the same incident frequency if $\hbar\omega_i \ll m_e c^2$ with a cross section equal to the Thomson scattering cross section $\sigma_T = (8\pi/3)(e^2/m_e c^2)^2 \simeq 6.65 \times 10^{-25} \text{ cm}^2$. When the electromagnetic waves have an extremely large amplitude such that the electron reaches a relativistic speed (relevant to FRBs near the FRB generation site), the electron motion trajectory becomes complicated and the cross section much enhanced (Yang and Zhang, 2020); see Sec. VIII.C for details. The existence of a strong background magnetic field further complicates the picture (Beloborodov, 2021a; Qu, Kumar, and Zhang, 2022).

When an electron moves relativistically and interacts with electromagnetic waves with angular frequency ω_i, it would inverse Compton scatter the waves to a higher frequency

$$\omega_s \sim \gamma_e^2(1 - \beta\cos\theta_i)\omega_i. \tag{95}$$

This process could be relevant to FRB radiation (Sec. V.B.3).

IV. GENERAL CONSTRAINTS ON THE MODELS

To interpret FRBs, a competent model needs to invoke a radiation mechanism model to address individual burst properties (brightness temperature, polarization properties, spectral down-drifting, radio efficiency, high-energy emission, etc.) and a source model that accounts for the global properties of the bursts (energetics, burst rate, luminosity or energy function, redshift distribution, host galaxy properties, etc.). Before discussing these in Secs. V and VI, one can place some generic, essentially model-independent constraints on the models based on some basic observational facts and physical principles.

A. Burst duration (width) and engine size

After the convolution effects from scattering and instrumental effects (Sec. II.B) are corrected for, the intrinsic duration W_i of an FRB defines a length scale

$$R_i = cW_i = (3 \times 10^7 \text{ cm})W_{-3}, \tag{96}$$

where W_{-3} is the intrinsic duration in milliseconds. The size of the FRB central engine R_0 should satisfy $R_0 \lesssim R_i$. This is straightforward if the FRB emitter does not move with a relativistic speed. The reason for this is that if $R_0 > R_i$, even if the emission region is lit up simultaneously everywhere, the duration of the event should be $R_0/c > W_i$ due to the light propagation delay between the front end and the rear end of the emission region with respect to the observer.

If the FRB emitter is moving toward the observer with a relativistic speed (which is likely the case, as discussed in Secs. IV.B and IV.F.1), the situation is more complicated, but the conclusion of $R_0 \lesssim R_i$ remains valid. More generally we assume that the emitter travels with a bulk Lorentz factor Γ in a direction with an angle θ with respect to the line of sight. In the lab frame, we consider the central engine to send off two light signals toward the relativistic emitter (the fastest causal connection is through propagation of photons), and the emitter promptly reacts to the two signals and sends off two signals to the observer immediately after receiving the two central engine signals. Approximating the emitter as a point source and ignoring cosmic expansion, one can write the following relation between the three intervals (Zhang, 2018c):

$$\frac{1 - \beta\cos\theta}{1 - \beta}\Delta t_{eng} = (1 - \beta\cos\theta)\Delta t_e = \Delta t_{obs}, \tag{97}$$

where Δt_{eng} is the time interval for the engine to emit two signals, Δt_e is the time interval for the relativistic emitter to receive the two signals from the engine and also the time interval for the emitter to send off two signals, and Δt_{obs} is the time interval for the observer to detect the two signals. In Eq. (97) β is the dimensionless speed of the emitter, θ is the angle between the direction of motion and the line of sight, the factor $1 - \beta\cos\theta$ (which $\simeq 1/2\Gamma^2$ for $\theta = 0$) is a factor accounting for the propagation effect, and $\Gamma = (1 - \beta^2)^{-1/2}$ is the Lorentz factor of the emitter. One can see that even though the emitter timescale is stretched due to its motion, the observed timescale Δt_{obs} still tracks the central engine timescale Δt_{eng} ($t_{obs} = t_{eng}$ for $\theta = 0$).[9] As a result, W_i can be used to constrain the size of the central engine in any case.

Equation (96) immediately suggests that the most compact stellar-mass objects in the Universe, i.e., a neutron star or a stellar-mass black hole, are the most likely candidates for a FRB engine. Larger objects (such as white dwarfs, stars, and even supermassive black holes) have been invoked to interpret

---

[9]If the line of sight is outside the emission beam, $1 - \beta\cos\theta \sim 1 - \cos\theta$, which becomes $\gg 1 - \beta$, so Δt_{obs} becomes $> \Delta t_{eng}$. One can see a longer burst with a lower flux. Such off-axis FRBs, also known as slow radio bursts, may be detectable from Galactic magnetars or other FRB-emitting sources (Zhang, 2021).

FRBs in some models, but these models must produce contrived conditions to allow only a small enough region to power an FRB.

B. Variability timescale and emission radius

The rapid variability timescale, particularly the ~ 60 ns timescale observed in rFRB 20200120E from the M81 globular cluster, can be used to further constrain the emission radius of FRBs (Beniamini and Kumar, 2020; Lu, Beniamini, and Kumar, 2022). For an on-beam FRB (i.e., $\theta \sim 0$ for a point source or $\theta < \theta_j$ for a conical jet with an opening angle θ_j), a natural variability timescale[10] is

$$\delta t \simeq \frac{R_{\text{FRB}}}{2c\Gamma^2}. \tag{98}$$

This timescale defines both the observed time for the emitter to travel to the emission radius R in the rising phase and the angular spreading time due to the propagation delay of a spherical jet front in the decaying phase. In principle, if one is allowed to arbitrarily increase the Lorentz factor of the emitter, any small δt can be reproduced for any R. Therefore, Eq. (98) alone is not constraining. Interesting constraints can be posed when the duration of the burst W is considered. For certain models in which the synchrotron maser model invokes the external shock (Metzger, Margalit, and Sironi, 2019), the emission radius can be estimated as $R_{\text{FRB}} \sim \Gamma^2 cW$. This immediately suggests that δt cannot be significantly shorter than W. The 60-ns variability from the millisecond-duration bursts of the M81 globular cluster FRB (Nimmo et al., 2022) therefore disfavors the external shock model of FRBs (Lu, Beniamini, and Kumar, 2022). The synchotron maser internal shock model (Beloborodov, 2020) is still allowed. However, it suffers from other drawbacks. For example, the frequency down-drifting feature, which the external shock model interprets as the shock propagating to progressively larger radii (Metzger, Margalit, and Sironi, 2019), is no longer straightforwardly interpreted within the internal shock models. On the other hand, rapid variability of FRBs is not a challenge to the magnetospheric models, as a 0.4-ns pulse has been observed from the magnetosphere of the 33-ms Crab pulsar (Hankins and Eilek, 2007) (even though FRBs are more energetic than nanoshots).

C. Periodicity

The special source FRB 20191221A was detected to have a 0.2168-s periodic separation with a 3-s duration (Andersen et al., 2022). Since known sources of a subsecond period are all rotating neutron stars (pulsars), this source offers a definite clue that at least some FRBs originate from pulsarlike objects. Further arguments can be made that the FRB radiation region (at least for this source) is the magnetosphere of an underlying pulsar or magnetar (Andersen et al., 2022; Beniamini and

Kumar, 2022). This is because models invoking emission regions outside the magnetosphere do not have well-defined geometric windows to maintain a strict periodic window.

The lack of periodicity from active repeaters such as rFRB 20121102A (Zhang, Geng, and Huang, 2018; D. Li et al., 2021; Hewitt et al., 2022) and rFRB 20201124A (J.-R. Niu et al., 2022; Xu et al., 2022), on the other hand, places fewer constraints on the models. Katz (2020a) argued that this suggests a black hole rather than a neutron star origin of repeating FRBs. This argument is not strong because, unlike pulsar emission, FRB radiation pressure is so strong that the magnetospheric structure is likely significantly distorted, so a well-defined magnetospheric window (the conventional open field line region) likely does not exist, and it is entirely possible that an FRB-emitting neutron star emits bursts at random phases. The radio bursts from the magnetar SGR J1935+2154 seem to be emitted from a much wider phase window than the narrow window for pulsed emission (Zhu et al., 2023). With the burst data alone, it appears that the source does not have a strict periodicity, even though the magnetar has a strict 3.24-s period.

Thus far only rFRB 20180916B has been confirmed to possess a long-term 16-d periodicity (Amiri et al., 2020; Pastor-Marazuela et al., 2021; Pleunis et al., 2021b). Its origin is subject to debate. The most natural interpretation would be to attribute this to the orbital period of a binary system, with the emission from the FRB emitter reaching the observer only in a particular phase window (Ioka and Zhang, 2020; Lyutikov, Barkov, and Giannios, 2020; Wada, Ioka, and Zhang, 2021). Other interpretations of the 16-d period of rFRB 20180916B include magnetar precession (Levin, Beloborodov, and Bransgrove, 2020; Yang and Zou, 2020), slowly rotating magnetars (Beniamini, Wadiasingh, and Metzger, 2020), and even precession of a black hole accretion disk (Katz, 2022a). None of these scenarios for the 16-d periodicity were theoretically predicted before the discovery of rFRB 20180916B. Therefore, it would be uncomfortable if such long-term periodicity were a common feature of active repeaters because that would require such periodicity being at the heart of FRB generation mechanisms (Zhang, 2020d). It is now clearer that such long-term periodicity is not commonly observed among active repeaters (the case of rFRB 20121102A is to be confirmed; see Sec. II.D). Whatever mechanism that is operating in rFRB 20180916B likely applies in rare cases and is probably attributable to coincidence.

D. Energetics, radio emission efficiency, and beaming

The derived isotropic energies of individual bursts and the energy-dependent burst rates for repeaters can be used to place interesting constraints on the average luminosity and total energy budget of the underlying FRB source that can be used to constrain FRB source models. For one-off FRBs, the true peak luminosity and energy of the burst are

$$L_p = L_{p,\text{iso}} f_b \eta_r^{-1},$$
$$E = E_{\text{iso}} f_b \eta_r^{-1}, \tag{99}$$

---

[10]Scintillation (see Sec. VIII.A for more discussion) can introduce modulations in shorter timescales, but with small amplitudes. Distinct pulses in an FRB light curve should be intrinsically related to the size of the source or emission region.
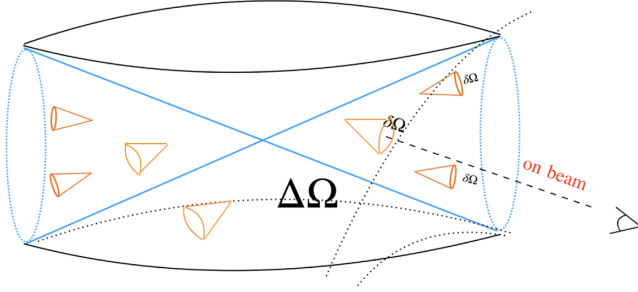
FIG. 8. Sketch of the beaming factor of individual bursts (with a solid angle $\delta\Omega$) and global beaming (with a solid angle of $\Delta\Omega$). A fan beam from a magnetospheric rotator is illustrated as an example for global beaming, but a more general geometry is possible.

where $L_{\mathrm{p,iso}}$ [Eq. (16)] and E_{iso} [Eq. (17)] are the isotropic radio peak luminosity and energy measured directly from observations, η_r is the radio emission efficiency, and

$$f_b \equiv \frac{\delta\Omega}{4\pi} \qquad (100)$$

is the beaming factor of an individual burst, with $\delta\Omega$ the solid angle of the burst. Note that f_b reduces and η_r^{-1} increases the energy budget of the source, so the effects of the two factors tend to cancel each other out. Neither factor is well constrained from observations. The x-ray burst associated with FRB 200428 was more than 10^4 more energetic than the radio burst itself (Mereghetti et al., 2020; C. K. Li et al., 2021; Ridnaia et al., 2021), so for this event the upper limit of η_r is $\sim 10^{-4}$–10^{-5}. Various x-ray flux upper limits for extragalactic FRBs place a lower limit on η_r that is of this order or even smaller (Piro et al., 2021; Laha et al., 2022a, 2022b).

For repeating sources, one should consider the average energy-dependent bursting rate $dN/dtdE_{\mathrm{iso}}$ during the active phase and the observational duty cycle of the active phase ζ [for instance, for the rFRB 20121102A observing campaign with FAST (D. Li et al., 2021) the observational duty cycle is about 60 h out of 47 d]. One should also introduce a global beaming factor

$$F_b \equiv \frac{\Delta\Omega}{4\pi}, \qquad (101)$$

which can be larger than f_b of the individual bursts. This is because the global emission beam can have a larger solid angle $\Delta\Omega$, inside which each burst could have a narrower beam; see Fig. 8. The average source luminosity that is used to make FRBs is

$$L_{\mathrm{src}} = \int_{E_{\mathrm{iso,m}}}^{E_{\mathrm{iso,M}}} \left(\frac{dN}{dtdE_{\mathrm{iso}}}\right) E_{\mathrm{iso}}(F_b\eta_r^{-1}) dE_{\mathrm{iso}}, \qquad (102)$$

where $E_{\mathrm{iso,m}}$ and $E_{\mathrm{iso,M}}$ are the minimum and maximum isotropic FRB energy from the source. The reason that F_b rather than f_b is adopted is the following. Even though each burst has a beaming factor f_b, altogether there are $\Delta\Omega/\delta\Omega$ such bursts on average, most of which are not detected but are added to the energy budget of the source. The final beaming factor is therefore $(\Delta\Omega/\delta\Omega)f_b = F_b$.

Assume that the repeater source has a lifetime τ and that the activity level remains unchanged during this lifetime. The total energy budget of the source over a duration τ can be estimated as

$$E_{\mathrm{src}} = \int_0^{\tau} \int_{E_{\mathrm{iso,m}}}^{E_{\mathrm{iso,M}}} \left(\frac{dN}{dtdE_{\mathrm{iso}}}\right) E_{\mathrm{iso}}(F_b\eta_r^{-1}\zeta^{-1}) dE_{\mathrm{iso}} dt, \qquad (103)$$

where $\zeta = \tau_{\mathrm{obs}}/\tau$ is the observational duty cycle.

Interesting constraints on the energy budget of repeaters have been made. For rFRB 20121102A, D. Li et al. (2021) reported that 1652 bursts were detected in ~ 60 h during a 47-d observational campaign. The total emitted radio energy [corresponding to the integral in Eq. (103) without the $F_b\eta_r^{-1}\zeta^{-1}$ factor] is $\sim 3.4 \times 10^{41}$ erg. Considering that $\zeta = 60/(47 \times 24) = 0.053$, $\eta_r = 10^{-4}\eta_{r,-4}$, and $F_b = 0.1F_{b,-1}$, one can derive the total source energy used to make FRBs as $E_{\mathrm{src}} = (6.4 \times 10^{45}$ erg$)F_{b,-1}\eta_{r,-4}^{-1}(\zeta/0.053)^{-1}$. This is already $\sim 4\%$ of the total dipolar magnetic energy $[E_B \sim (1/6)B^2R^3 \sim (1.7 \times 10^{47}$ erg$)B_{15}^2R_6^3]$ of a magnetar. Since rFRB 20121102A has already existed for over a decade, this observation poses a significant energy budget issue for the magnetar model unless η_r is larger or F_b is smaller. The magnetospheric models satisfy these constraints,[11] but the synchrotron maser shock model is already severely constrained by the data; see Sec. VI.A for details. Note that before the FAST observations, Margalit, Metzger, and Sironi (2020) had already posted a tight energy budget constraint on rFRB 20121102A based on the previous data within the framework of the magnetar synchrotron maser model. The many more bursts detected by FAST (D. Li et al., 2021) only tightened the constraints for the source. Even more stringent constraints on the magnetar synchrotron maser model have been established for another active repeater rFRB 20201124A (Xu et al., 2022; Zhang et al., 2022).

E. Brightness temperature and coherent radiation

Astronomical objects emit four levels of electromagnetic radiation with increasing complexity (Table II): blackbody radiation, thermal radiation, incoherent nonthermal radiation, and coherent nonthermal radiation. Blackbody and thermal radiation requires the emitting particles to be in thermal equilibrium (defined by the gas temperature T), with blackbody radiation having the additional requirement that photons have a large enough optical depth to reach thermal equilibrium as well (Rybicki and Lightman, 1979). Thermal radiation includes blackbody radiation but also allows photons not to achieve thermal equilibrium. One example is thermal bremsstrahlung that has a different spectral shape from blackbody radiation, with the cutoff energy defined by the gas temperature T. If particles are accelerated to deviate from thermal equilibrium, say, in shocks or magnetic reconnection regions, the radiation becomes nonthermal. As nonthermal particles typically have a one segment or multisegment power-law

---

[11]Because of the unidentified coherent mechanism of FRBs, the radio efficiency in the magnetospheric models cannot be predicted. However, the radio emission efficiency of radio pulsars is observed to range from 10^{-8} to close to unity (Szary et al., 2014).

TABLE II. Astrophysical radiation mechanisms.

Mechanisms	Particles	Photons	Examples
Blackbody	Thermal equilibrium	Thermal equilibrium	CMB, stars
Thermal	Thermal equilibrium	May or may not be in thermal equilibrium	Disks, intracluster medium
Incoherent nonthermal	Nonthermal	Subject to self-absorption limit	SNRs, GRBs, blazars
Coherent nonthermal	Nonthermal	Not subject to self-absorption limit	Radio pulsars, FRBs

distribution, nonthermal radiation spectra are typically broken power laws. In particular, in the low-frequency regime nonthermal radiation is usually subject to self-absorption from the opposite process of the emission mechanism if particle radiation is incoherent.

Coherent nonthermal radiation can be defined in different ways, but the most straightforward way is through its ability to overcome the self-absorption limit. The self-absorption-defined specific luminosity limit at a particular frequency is the blackbody specific luminosity at that frequency for a gas with the maximum temperature and source size allowed by the emitter. For electrons with a characteristic Lorentz factor γ_e in the comoving frame, the comoving-frame effective temperature would be $kT' \sim \gamma_e m_e c^2$. For a synchrotron radiation source, $\gamma_e = \max(\gamma_m, \gamma_a)$ is usually the maximum of the following two terms: the minimum injection Lorentz factor γ_m and the corresponding Lorentz factor for self-absorption γ_a (Kumar and Zhang, 2015). As a result,

$$kT' = \gamma_e m_e c^2 = \max(\gamma_m, \gamma_a) m_e c^2 \qquad (104)$$

or

$$T' = (5.9 \times 10^{11} \text{ K})\gamma_{e,2} \qquad (105)$$

defines the maximum incoherent brightness temperature in the comoving frame, where $\gamma_e \sim 100$ has been adopted. For radio galaxies, Kellermann and Pauliny-Toth (1969) showed that the observations had a maximum brightness temperature of $T_{b,\max} \sim 10^{12}$ K, which corresponds to a typical electron Lorentz factor $\gamma_e \sim 10^2$–10^3. They argued that this limit is physically related to the requirement that the second-order Compton scattering power does not exceed that of the first-order synchrotron self-Compton scattering through self-regulated Compton cooling. For systems like GRBs or blazar jets, γ_e is related to the bulk Lorentz factor of the jet, which directly defines the internal energy density (and hence the effective temperature) in the emission region.

For a relativistic emitter beaming toward Earth, the allowed maximum radio specific flux at a frequency is larger than the comoving value by a factor of $\mathcal{D}$ for an extended source or $\mathcal{D}^3$ for a point source (Zhang, 2018c), where

$$\mathcal{D} \equiv \frac{1}{\Gamma(1 - \beta \cos\theta)} \simeq \Gamma \qquad (106)$$

is the Doppler factor, Γ and θ carry the same meaning defined earlier, and the final approximation applies to the regime $\theta \leq 1/\Gamma$. Compared with the observationally defined brightness temperature [Eq. (18)], one can perform either of the

following two approaches. One is to derive brightness temperature in the comoving frame (T_b') and compare it with the maximum T'; the other is to derive the maximum allowed T in the observer frame and compare it with observationally defined T_b [Eq. (18)]. I adopt the more straightforward latter approach and derive the condition that coherence is required by the data if

$$T_b \geq \mathcal{D}\gamma_e m_e c^2/k \simeq (5.9 \times 10^{13} \text{ K})\Gamma_2 \gamma_{e,2}. \qquad (107)$$

This result is consistent with that of Lyubarsky (2021), who adopted the opposite approach. Since FRBs have an observed T_b much greater than this value, their radiation mechanisms must be coherent. I discuss various coherent mechanisms in Sec. V.

F. Attenuation processes

To have high-T_b radio pulses detectable from Earth, the radio waves must overcome various absorption or scattering processes along the propagation paths. The three important processes to attenuate the radio emission flux are induced Compton scattering, free-free absorption, and synchrotron absorption, which I now discuss in turn.

1. Induced Compton scattering and Lorentz factor lower limit

With the existence of free electrons, photons with a particular frequency can be scattered out of the state and other photons with different frequencies can be scattered into the state. The Thomson scattering optical depth can be estimated as $\tau_T \sim n_e \sigma_T R$, where n_e is the electron number density, $\sigma_T = (8\pi/3)(e^2/m_e c^2)^2 \simeq 6.65 \times 10^{-25}$ cm^2 is the Thomson cross section, and R is the size of the emission region. This optical depth is relevant for scattering of high-frequency photons (for very-high-energy photons, the Klein-Nishina correction is needed), but in the low-frequency regime, scattering can be enhanced significantly by induced Compton scattering if T_b is high enough (Kompaneets, 1957; Wilson and Rees, 1978; Thompson et al., 1994; Lyubarsky, 2008). The essence of this mechanism can be summarized as follows (Wilson and Rees, 1978). Consider two photon states (not electron states) a and b (defined by both the energies and the directions of the photons) with photon occupation numbers n_a and n_b, respectively. The spontaneous change in n_a because of scattering from a to b is $dn_a/dt \propto -n_a$. However, since photons are bosons that satisfy the Bose-Einstein statistics, the existence of photons at b actually boost the scattering rate from a to b by a factor of $n_b + 1$, i.e., $dn_a/dt = -n_a(1 + n_b)$. Similarly, the scattering rate from b to a is $dn_a/dt \propto (n_a + 1)n_b$. The net

change at level a is $dn_a/dt \propto (n_a + 1)n_b - n_a(1 + n_b)$, which essentially cancels out but leaves a small term related to the recoil frequency shift due to Compton scattering, i.e., $\Delta\nu/\nu = (h\nu/m_e c^2)(1 - \cos\theta)$, where θ is the angle between the directions of a and b. It was found that for cold electrons without bulk motion induced Compton scattering becomes important when $(k_B T_b/m_e c^2)\Omega^2 > 1$ (where Ω is the solid angle of the uniform beam) (Wilson and Rees, 1978).[12] As a result, the optical depth due to induced Compton scattering is enhanced with respect to Thomson scattering by the same factor, i.e.,[13]

$$\tau_C \simeq \frac{3}{8\pi^2}\left(\frac{k_B T_b}{m_e c^2}\Omega^2\right)\tau_T \simeq (6.4 \times 10^{24})\Omega^2 T_{b,36}\tau_T. \quad (108)$$

The detailed expression depends on the explicit problems one is addressing. For example, if one considers the induced Compton scattering constraint in an emitting source, the expression can be written as (Lyubarsky, 2008)

$$\tau_C \simeq \frac{3\sigma_T}{8\pi}\frac{cn_e\mathcal{S}_\nu^{obs}}{m_e\nu^2}\left(\frac{D_L}{r_0}\right)^2 Z, \quad (109)$$

where $\mathcal{S}_\nu^{obs}$ is the observed specific flux of the FRB, ν is the FRB frequency, D_L is the luminosity distance of the source, r_0 is the radius of the launching point, and Z is an integral that has the dimension of r_0/c and carries the information of Ω. For another example, if one considers the Compton scattering induced by a medium as an FRB from a separate source passes through it, the expression becomes (Ioka and Zhang, 2020)

$$\tau_C \simeq \frac{3\sigma_T}{32\pi^2}\frac{L_\nu n_e c\Delta t}{r^2 m_e\nu^2}, \quad (110)$$

where r is the distance between the FRB source and the scatterer. Note that this discussion applies to an unmagnetized plasma with $\omega_B \ll \omega_p$. In a highly magnetized environment such as the magnetosphere of a neutron star, charged particles are confined in strong magnetic fields, so the particles required to have the right directions and energies for induced Compton scattering are not available. As a result, there is no need to consider the induced Compton scattering constraint in the emission region if FRBs are emitted from the magnetosphere of a central engine.

When the emitter is moving relativistically with a bulk Lorentz factor Γ, the induced Compton scattering optical depth drops significantly (Lyubarsky, 2008). From Eq. (108), noticing $\Omega \propto \Gamma^{-2}$ and $T'_b = T_b/\mathcal{D} \simeq T_b/\Gamma$, one gets

$$\tau_C \sim \frac{k_B T_b}{m_e c^2}\frac{\tau_T}{\Gamma^5}, \quad (111)$$

which is significantly smaller than the case without bulk motion.

The induced Compton scattering optical depth also drops if the electron gas is relativistically hot. Lu and Kumar (2018) suggested that for a narrow Gaussian-like spectrum with a characteristic electron energy γ_e, the approximated optical depth is

$$\tau_C \sim \frac{kT_b}{m_e c^2}\frac{\tau_T}{\gamma_e^5}. \quad (112)$$

For a power-law photon spectrum, the results depend on the spectral index p (convention $I_\nu \propto \nu^p$), but the suppression factor is shallower than γ_e^{-5}.

Some FRB emission models invoke relativistic shocks as the emission site (Lyubarsky, 2014; Beloborodov, 2017; Metzger, Margalit, and Sironi, 2019; Plotnikov and Sironi, 2019; Beloborodov, 2020). The emission region also would be relativistically hot in the comoving frame. Combining Eqs. (108), (111), and (112) and noticing Ω^2 is already included in the $1/\Gamma^5$ suppression factor, one can derive the condition of $\tau_C < 10$ as[14]

$$\Gamma\gamma_e \gtrsim (5.8 \times 10^4)T_{b,36}^{1/5}\tau_T^{1/5}. \quad (113)$$

Since $\gamma_e \propto \Gamma$ is generally expected,[15] one can place a lower limit of Γ as

$$\Gamma \gtrsim 240\xi_e^{1/2}T_{b,36}^{1/10}\tau_T^{1/10}, \quad (114)$$

where $\gamma_e = \xi_e\Gamma$ has been assumed. Similar constraints were derived by Lyubarsky (2008) and Murase, Kashiyama, and Mészáros (2016). Note that within the relativistic shock models, a Lorentz factor of this order is also required by the duration and variability constraint [Eq. (98)], so the induced Compton scattering constraint is usually satisfied in the shock model without introducing an additional condition (Metzger, Margalit, and Sironi, 2019; Beloborodov, 2020).

2. Free-free absorption

Radio emission can be also attenuated via free-free absorption, the inverse process of free-free emission or bremsstrahlung. The importance of free-free absorption for FRBs has been extensively discussed (Luan and Goldreich, 2014; Murase, Kashiyama, and Mészáros, 2016; Kumar, Lu, and Bhattacharya, 2017; Metzger, Berger, and Margalit, 2017; Yang and Zhang, 2017; Kundu and Zhang, 2021).

---

[12]The factor $k_B T_b/m_e c^2$ is the product of the photon occupation number $k_B T_b/h\nu$ and the fractional change of energy $\sim h\nu/m_e c^2$.

[13]A coefficient $3/8\pi^2$ is added with precise calculations (Lu, 2021). Note that Eq. (108) assumes a uniform electron number density. It has been suggested that the medium may be subject to filamentation due to the propagation of FRBs, which would significantly reduce the optical depth for induced Compton scattering (Sobacchi et al., 2022).

[14]Notice that induced Compton scattering mainly modifies the shape of the spectrum rather than exponentially attenuate photon flux. As a result, a larger optical depth than unity, for instance, $\tau_C = 10$, is adopted as the transition point where the effect becomes important.

[15]This is straightforwardly expected for external shocks. For internal shocks, γ_e is more related to the relative Lorentz factor between the colliding shells, which can also scale with Γ.

The free-free absorption coefficient [Eq. (90)] together with the relativistic correction factor $(1 + AT)$ (Sec. III.F.1) can be used to estimate the optical depth against free-free absorption. An FRB is transparent if the optical depth is below unity.

Free-free absorption is important when the density of the emitter or environment medium is high. Therefore, the free-free absorption constraint was adopted (Luan and Goldreich, 2014) to disfavor an early FRB model invoking flaring stars (Loeb, Shvartzvald, and Maoz, 2014). For repeating FRB models invoking a young magnetar born from a supernova explosion, free-free absorption was used to place a lower limit on the age of the supernova remnant before which the remnant shell is too dense to allow FRBs to escape freely (Metzger, Berger, and Margalit, 2017; Yang and Zhang, 2017); see Sec. VII for details. For FRB systems invoking relativisic shocks, either as the site of FRB emission or as a screen in front of FRB produced at an inner radius, free-free absorption in the hot shocked plasma could be important if the total kinetic energy exceeds $\sim 10^{44}$ erg, which may account for the frequency down-drifting feature observed in some FRBs (Kundu and Zhang, 2021).

3. External synchrotron absorption

For active repeaters surrounded by a persistent radio source (PRS) (Chatterjee *et al.*, 2017; C. H. Niu *et al.*, 2022), coherent FRB emission needs to pass through the PRS, which is likely powered by synchrotron radiation. Under certain conditions, FRBs could be absorbed by the PRS via synchrotron absorption, and the PRS source could subsequently be heated up by the absorbed FRBs (Yang, Zhang, and Dai, 2016).

Assuming that the nebula electrons have an initial differential number density spectrum $N(\gamma_e, 0) = K\gamma_e^{-p}$, one can estimate the synchrotron optical depth as

$$\tau_{\nu,\text{SR}} = \frac{e^2 KR}{4m_e c} \frac{1}{\nu_B} \left(\frac{\nu}{\nu_B}\right)^{-(p+4)/2} f(p), \qquad (115)$$

where $\nu_B = eB/(2\pi m_e c)$, R is the radius of electron acceleration region, and $f(p)$ is a function of order unity. Solving $\tau_{\nu,\text{SR}} = 1$, one can derive the synchrotron absorption frequency (Yang, Zhang, and Dai, 2016)

$$\nu_a = \nu_B \left[\frac{\pi}{2} \frac{eRK}{B} f(p)\right]^{2/(p+4)}. \qquad (116)$$

The spectrum of the nebula needs to be solved numerically by including electron injection, synchrotron cooling, and heating by FRBs, which would give rise to complicated spectra for both electrons and photons. The predicted spectra (Yang, Zhang, and Dai, 2016) turn out to share the general shape of the later observed PRS spectrum of rFRB 20121102A (Chatterjee *et al.*, 2017; Marcote *et al.*, 2017), as shown by Li, Yang, and Dai (2020). The small nebula size and not too high a synchrotron self-absorption frequency constrain the parameter space for such models in general (Metzger, Berger, and Margalit, 2017). Mode-dependent synchrotron absorption may change the polarization mode and enhance linear polarization (Qu and Zhang, 2023).

G. Ordered magnetic fields and strengths

The fact that FRB emission is linearly polarized with a high polarization degree poses a generic constraint, namely, there must be ordered magnetic fields in the FRB emission region. Indeed, current leading models to interpret FRBs invoke either magnetospheres of magnetized central engines or relativistic shocks with ordered magnetic fields. See Qu and Zhang (2023) for a recent survey of various emission mechanisms to produce high polarization in FRBs.

Further constraints on the strength of magnetic fields have been discussed in the literature (Kumar, Lu, and Bhattacharya, 2017; Lyutikov, 2017). The argument is that the electromagnetic wave energy density in the emission region should not exceed the magnetic energy density of the emitter in the same region before the FRB is emitted. Such a constraint can be placed if the FRB emission originates from dissipation of magnetic fields, or if the magnetic field in the emission region confines the generated FRB emission. Note that such a condition in general is not always necessary for producing intense electromagnetic radiation. For example, the fireball model for GRBs does not require one to abide by such a condition, with the electromagnetic energy of radiation generated from the thermal energy or the dissipated kinetic energy in the fireball (Zhang, 2018c). In the case of coherent radiation, on the other hand, many models require that ordered B fields should remain ordered during the emission processes. As a result, this condition is relevant.

The electromagnetic wave energy density, regardless of the emission frequency, can be estimated as $L_{\text{iso}}/4\pi R_{\text{FRB}}^2 c$, where R_{FRB} is the radius where FRB emission is radiated. The condition

$$\frac{L_{\text{iso}}}{4\pi R_{\text{FRB}}^2 c} < \frac{B^2}{8\pi} \qquad (117)$$

gives

$$B > \sqrt{\frac{2L_{\text{iso}}}{c}} \frac{1}{R_{\text{FRB}}} \simeq (8.2 \times 10^{15} \text{ G}) L_{\text{iso},42}^{1/2} R_{\text{FRB}}^{-1}. \qquad (118)$$

The key is how to estimate R_{FRB}. If one assumes that $R_{\text{FRB}} = cW_i = (3 \times 10^7 \text{ cm})W_{\text{ms}}$, one obtains $B > (2.7 \times 10^8 \text{ G})L_{\text{iso},42}(W_{\text{ms}})^{-1}$, which leads to the conclusion that the emission region has to be within the magnetosphere of a neutron star (Lyutikov, 2017). This argument, however, is flawed since R_{FRB} cannot always simply be estimated as cW_i. If the emitter is moving relativistically with a bulk Lorentz factor Γ, as is envisaged in the synchrotron maser models, one has $R_{\text{FRB}} = \Gamma^2 cW_i = (3 \times 10^{13} \text{ cm})\Gamma_3^2 W_{-3}$. The B-field constraint becomes

$$B > \sqrt{\frac{2L_{\text{iso}}}{c}} \frac{1}{\Gamma^2 cW_i} \simeq (2.7 \times 10^2 \text{ G})L_{\text{iso},42}^{1/2} \Gamma_3^{-2} W_{-3}^{-1}. \qquad (119)$$

Note that the magnetic field strength at the light cylinder of a magnetar is $B_{\text{lc}} \simeq B_*(cP/2\pi R_*)^{-3} = (9.2 \times 10^3 \text{ G})B_{*,15}P^{-3}R_{*,6}^3$. Thus, this estimate allows the emission region to be outside of a neutron star magnetosphere.

H. Afterglow

A generic constraint can be placed on the brightness of the multiwavelength afterglows of FRBs. Afterglow observations for GRBs have been essential in identifying their multi-wavelength counterparts and host galaxies as well as measuring their redshifts. In the case of FRBs, the isotropic energy is typically more than 10 orders of magnitude smaller than that of GRBs ($E_{\mathrm{iso,FRB}} \sim 10^{39}$ erg vs $E_{\mathrm{iso,GRB}} \sim 10^{52}$ erg). The expected FRB afterglow emission is expected to be much fainter (Yi, Gao, and Zhang, 2014). One possible way of enhancing afterglow emission is to assume that the FRB radiative efficiency η_r is low so that the afterglow kinetic energy can be boosted by a factor of η_r^{-1}. According to the standard GRB afterglow model (Mészáros and Rees, 1997; Sari, Piran, and Narayan, 1998; Zhang, 2018c), the characteristic synchrotron frequency of injected minimum-energy electrons and the peak synchrotron specific flux for a relativistic jet decelerated by a constant-density medium read

$$\nu_m = (3.3 \times 10^8 \text{ Hz})(1+z)^{1/2} t_d^{-3/2} \epsilon_{B,-2}^{1/2}$$
$$\times [\epsilon_{e,-1}(p-1)/(p-2)]^2 (E_{\mathrm{FRB},38}/\eta_{r,-6})^{1/2}, \quad (120)$$

$$F_{\nu,\mathrm{max}} = (1.6 \times 10^{-8} \text{ mJy})(1+z)\epsilon_{B,-2}^{1/2}$$
$$\times (E_{\mathrm{FRB},38}/\eta_{r,-6}) n^{-1} D_{\mathrm{L},28}^{-2}, \quad (121)$$

where the blast wave kinetic energy is normalized to 10^{44} erg (which assumes $\eta_r = 10^{-6}$ for $E_{\mathrm{FRB}} = 10^{38}$ erg), ϵ_e and ϵ_B are shock equipartition parameters for the electrons and magnetic fields, respectively, p is the power-law index of the injected electrons, n is the medium density, t_d is the observing time in days, and $D_{\mathrm{L},28}$ is the luminosity distance of the source in 10^{28} cm. One can see that the afterglow emission peaks in the radio band and is extremely faint. Detailed calculations (Yi, Gao, and Zhang, 2014) suggested that a detection is possible only if the source is very near and the FRB is extremely energetic (i.e., the radio efficiency is low), for instance, $E = E_{\mathrm{FRB}}/\eta_r = 10^{47} E_{\mathrm{FRB},40}\eta_{r,-7}$ erg. For a relativistic, mildly magnetized jet, the reverse shock emission could be brighter than the forward shock emission, which would ease the detection of the afterglow (Yi, Gao, and Zhang, 2014).

No confirmed FRB afterglow has been detected thus far (even for the Galactic FRB 200428). This is consistent with theory and suggests that η_r is not extremely low. Note that in the synchrotron maser model invoking external shocks (Metzger, Margalit, and Sironi, 2019) the multiwavelength counterpart associated with the FRB could be regarded as its own "afterglow," even though the electron energy distribution is assumed to be thermal rather than a power law. No Fermi acceleration of particles is envisaged, which could be a problem theoretically. The two hard spikes observed in the x-ray counterpart (Mereghetti et al., 2020; C. K. Li et al., 2021) of FRB 200428 (Andersen et al., 2020; Bochenek, Ravi, and Dong, 2021) can be interpreted within this model as the external shock emission (Margalit et al., 2020), even though it is more naturally interpreted as emission within the

magnetar magnetosphere (Ioka, 2020; Lu, Kumar, and Zhang, 2020; Yang and Zhang, 2021).

V. COHERENT RADIATION MECHANISMS

Coherent radiation mechanisms invoke fundamental plasma physics that can be shared among different source models. For example, coherent curvature radiation by bunches has been discussed in many different contexts involving magneto-spheres, such as radio emission from the inner magneto-spheres of pulsars and magnetars (Ruderman and Sutherland, 1975; Katz, 2014; Kumar, Lu, and Bhattacharya, 2017; Yang and Zhang, 2018), from ejected magnetospheres from "blit-zars" (Falcke and Rezzolla, 2014; Zhang, 2014), from kinetic-energy "combed" magnetospheres (Zhang, 2017), from magnetospheres during asteroid-NS collisions (Geng and Huang, 2015; Dai et al., 2016; Dai, 2020), and from the global magnetospheres formed by merging charged objects (Zhang, 2016). The synchrotron maser mechanism in relativistic shocks, on the other hand, has been invoked in the magnetar internal (Beloborodov, 2017, 2020) or external (Lyubarsky, 2014; Metzger, Margalit, and Sironi, 2019) shock models, shocks from low-B compact objects (Waxman, 2017; Long and Pe'er, 2018), and even black hole accreting systems (Sridhar, Metzger et al., 2021). Therefore, it is reasonable to detach radiation models from source models and discuss the general physics behind each radiation model. That is the task of this section.

A. Coherent radio emission overview

Following the discussion in Sec. IV.E, I can summarize two fundamental properties of a coherent radiation mechanism: (1) the observed luminosity L_{obs} exceeds the sum of the emitted power P_e for individual particles, i.e., $L_{\mathrm{obs}} > N_e P_e$, where N_e is the total number of electrons, and (2) the observed luminosity is not subject to self-absorption, so Eq. (107) is satisfied.

There are several ways to classify coherent radiation mechanisms. Based on differences in general physics, one can classify the mechanisms as the following three types (Melrose, 1978). Each mechanism has its emission properties and backreaction mechanisms.

- *Coherent emission by bunches (or the "antenna" mechanism).*—In this mechanism, emitting particles are physically clustered in six-dimensional phase space, i.e., in both 3D position space and 3D momentum space. This is how coherent emission is emitted from antennae in radio stations. Within this mechanism, microscopic particles (such as electrons) are physically bunched together to radiation as a global particle with a total charge $N_{e,b}e$, where $N_{e,b}$ is the number of charges in each bunch, typically distributed within a unit volume defined by the wavelength of the radio waves ($N_{e,b} \sim n_e \gamma^2 \lambda^3$, where n_e is the charge number density, λ is the wavelength, and γ is the bulk Lorentz factor of the bunch). The emission power of the bunch, depending on the degree of coherence, can reach a maximum of $N_{e,b}^2 P_e$ (Yang and Zhang, 2018). The total luminosity of the system would be $\sim N_{e,b}^2 N_b P_e$, where $N_b \sim N_e/N_{e,b}$

is the number of bunches in the emission region. The backreaction effects of such bunched emission are twofold: owing to internal Coulomb repulsion, bunches tend to disperse in space. The radiation reaction may also make the particles disperse in the momentum space (Melrose, 1978).

- *Hydrodynamic instabilities (or "plasma masers").*—In this mechanism, some oscillation modes in a plasma exponentially grow with time, with macroscopic particles clustering in the momentum space. The magneto-hydrodynamic (MHD) waves eventually escape in the form of electromagnetic waves in the radio band. The backreaction effect is that, as the mode grows, dispersion in the momentum space occurs and the instability would suppress itself.
- *Kinetic instabilities (or "vacuum masers").*—In this mechanism, electromagnetic waves detached from the plasma fluid would undergo negative absorption in an energy-population-inverted medium such that the amplitude of emission grows with distance, reaching a high brightness temperature. The effect of backreaction is that masers tend to reduce population inversion such that the instability also suppresses itself.

Only a few types of objects are observed to emit coherent radio emission, for instance, the Sun, Jupiter, astronomical maser sources, pulsars, and FRBs. The mechanisms operating in different types of objects can achieve different degrees of coherence (i.e., different values of T_b). Melrose (2017) reviewed the mechanisms of coherent emission in different types of objects and suggested that they have different origins: (1) Plasma emission at the plasma frequency ω_p, which invokes Langmuir plasma waves (longitudinal oscillations) through a streaming instability as the trigger mechanism, likely applies to solar radio bursts; (2) electron cyclotron maser emission at the cyclotron frequency ω_B, which invokes a cyclotron plasma instability, likely applies to Jupiter and Earth aurora; and (3) pulsar coherent emission must have a different mechanism, which has at least four possibilities: curvature emission by bunches, linear acceleration emission, relativistic plasma emission, and anomalous Doppler emission. However, all four mechanisms encounter difficulties, and the pulsar coherent mechanism remains an enigma after more than half a century of study.

The prospect of understanding FRB coherent emission is not bright either, since it involves more extreme processes to produce coherent emission. In any case, many mechanisms have been discussed in the literature, including some that were reviewed by Zhang (2020b), Lyubarsky (2021), and Xiao, Wang, and Dai (2021). In the following, I present a critical review on various FRB coherent radiation models, which are generally grouped into two types based on the emission region: those involving magnetospheres (also called close-in or pulsarlike models) and those invoking relativistic shocks far outside of the magnetospheres (also called faraway or GRB-like models).

B. Magnetospheric models

Most pulsarlike mechanisms for FRBs, as expected, have been proposed to interpret pulsar radio emission. In the following, I discuss these mechanisms in turn, each with an introduction within the pulsar context, and then with a critical evaluation on its motivations and issues to account for FRB emission. Some pulsar mechanisms that have not been reinvented for FRBs are discussed at the end.

1. Pulsar magnetosphere basics

Before going over detailed pulsarlike models, it is informative to review the basic physics of pulsar magnetospheres. Consider a pulsar that carries a plasma-loaded magnetic field and rotates with an angular velocity $\vec{\Omega}$. We make two idealized assumptions here: (1) The plasma has infinite conductivity, so the net force received by each particle is zero, i.e., $e(\vec{E} + (1/c)[(\vec{\Omega} \times \vec{r}) \times \vec{B}]) = 0$ (the ideal MHD condition, which is also the force-free condition, as later explained), and (2) the rotating magnetosphere is in a steady state such that the $\partial/\partial t$ terms in Maxwell equations are zero (this strictly applies to a uniformly rotating $\vec{\Omega} \times \hat{\mu}_B = 0$ rotator, where $\hat{\mu}_B$ is the direction of the magnetic axis, which is either parallel or antiparallel to the direction of the spin axis $\vec{\Omega}$). From Maxwell equations and with some basic vector calculus, one can derive that everywhere in the magnetosphere within the light cylinder radius

$$R_{lc} = \frac{c}{\Omega} = \frac{cP}{2\pi} = (4.8 \times 10^9 \text{ cm})(P/1 \text{ s}). \quad (122)$$

The net charge density as observed in the inertial frame of an observer who watches the star rotate is the Goldreich-Julian (GJ) density (Goldreich and Julian, 1969),

$$\rho_e = \rho_{GJ} \equiv -\frac{\vec{\Omega} \cdot \vec{B}}{2\pi c} \frac{1}{1 - (\vec{\Omega} \times \vec{r}/c)^2} \simeq -\frac{\vec{\Omega} \cdot \vec{B}}{2\pi c}, \quad (123)$$

where $\vec{B}$ is the local magnetic field at a location in the magnetosphere, and for a dipolar field its strength falls with radius r as $B \simeq B_s(r/R)^{-3}$, where R is the neutron star radius and B_s is the surface magnetic field strength. The last approximation applies to the region well within the light cylinder. This corresponds to a net charge number density

$$n_{GJ} = \rho_{GJ}/e \sim (6.9 \times 10^{10} \text{ cm}^{-3})B_{12}P^{-1}. \quad (124)$$

By definition, with such a density there is no $\vec{E}$ component parallel to the local $\vec{B}$ vector (i.e., $E_\parallel = 0$), and the $\vec{E} \times \vec{B}$ drift velocity is simply the velocity $\vec{v}$ to allow particles to be frozen in the magnetic fields and corotate with the star, i.e., $(\vec{E} \times \vec{B})/B^2 = \vec{v}/c$. The local current density can be denoted as $\vec{j} = \rho_e \vec{v}$, so the ideal MHD condition $\vec{E} + (1/c)(\vec{v} \times \vec{B}) = 0$ can also be translated to the "force-free" condition $\rho_e \vec{E} + (1/c)(\vec{j} \times \vec{B}) = 0$ (Contopoulos, Kazanas, and Fendt, 1999; Timokhin, 2006). For an oblique rotator ($\vec{\Omega} \times \hat{\mu}_B \neq 0$), the $\partial/\partial t = 0$ assumption is no longer satisfied, but particle-in-cell (PIC) simulations showed that the GJ density is still an excellent description of the local charge density in a force-free magnetosphere (Spitkovsky, 2006). Note that the

Goldreich-Julian density does not depend on the specific assumption regarding the magnetic field configuration.

A force-free magnetosphere is uninteresting, with no particle acceleration and emission. In reality, however, maintaining a force-free magnetosphere is not easy. One needs to have abundant electron-positron pairs with a number density $n_\pm = \xi n_{GJ}$ and a multiplication factor $\xi \gg 1$ in order to maintain a net charge density matching the GJ density everywhere in the magnetosphere. Without copious pair production, deviation from the GJ density would be quickly built up, even if initially a GJ magnetosphere is realized. This is because the centrifugal force drives particles away due to the rapid spin of the star. As a result, various charge deficit regions, or "gaps," where $|\rho| < |\rho_{GJ}|$ is satisfied would form in the magnetosphere (Ruderman and Sutherland, 1975; Arons and Scharlemann, 1979; Cheng, Ho, and Ruderman, 1986; Muslimov and Tsygan, 1992). In these gaps, $E_\parallel$ no longer vanishes. Charged particles are accelerated and radiate curvature radiation or inverse Compton scattering, producing $e^\pm$ pairs via either the γB or $\gamma\gamma$ QED processes (Daugherty and Harding, 1996; Zhang and Harding, 2000; Hibschman and Arons, 2001). The pairs subsequently redistribute in the $E_\parallel$, forming an opposite $E_\parallel$ field, and eventually "screen" the original $E_\parallel$. The magnetosphere then again approaches the GJ force-free configuration. Such processes are likely to be unsteady, driving refreshed generation of pairs. Production of pairs has long been regarded as the necessary condition to power pulsar radio emission, with the radio pulsar "death line" defined such that pair production conditions fail (Ruderman and Sutherland, 1975; Zhang, Harding, and Muslimov, 2000).

Another way to modify the GJ magnetosphere is to introduce a global current $\vec{J}$ in the magnetosphere (Thompson, Lyutikov, and Kulkarni, 2002; Beloborodov, 2009). In this case, the net charge density as observed by a lab-frame observer becomes (Thompson, Lyutikov, and Kulkarni, 2002)

$$\rho_e = \rho_{GJ} + \rho_{\text{twist}},\tag{125}$$

where

$$\rho_{\text{twist}} = \frac{1}{4\pi c}\vec{\Omega}\cdot[\vec{r}\times(\nabla\times\vec{B})] \simeq \frac{1}{c^2}\vec{\Omega}\cdot(\vec{r}\times\vec{J})\tag{126}$$

describes a new charge density component to induce a twisted magnetic field component around the current (Ampère's law). A twisted magnetosphere can be still force free but is not in a steady state and would gradually untwist via dissipation within the twist-supported current with a nonzero potential (Beloborodov, 2009). Chen and Beloborodov (2017) showed from PIC simulations that an electric gap with an unscreened parallel electric field can form in a twisted magnetar magnetosphere, which continuously accelerates particles and maintains pair production. Twisted magnetospheres are usually discussed within the context of the magnetars after x-ray flares, which undergo secular untwisting in an extended period of time.

Recent PIC simulations revealed that besides charge-depleted gaps for pair starved magnetospheres, another promising energy dissipation and particle acceleration site for a pair-rich magnetosphere is the equatorial current sheet region outside the light cylinder (Kalapotharakos, Harding, and Kazanas, 2014; Kalapotharakos et al., 2018; Philippov and Spitkovsky, 2018). This region is regarded as a possible new site for high-energy emission from pulsars.

Phenomenological studies and geometric modeling of pulsar radio emission suggest that there are potentially three types of pulsar radio emission:

- *Inner magnetospheric radio emission*.—Radio emission from old, slowly rotating pulsars is consistent with emission from the inner magnetosphere in the open field line regions. The double-peak pulse profile and its "radius-to-frequency mapping" (wider separations at lower frequencies) as observed in a large sample of pulsars strongly support this geometric configuration. Modeling suggests that the radius of the emission is approximately tens of stellar radii (Rankin, 1993).

- *Outer magnetospheric radio emission*.—Young pulsars such as the Crab pulsar have a pair of pulses that align with the high-energy γ-ray and x-ray pulses (Hankins and Eilek, 2007). Since the latter has to be emitted from the outer magnetosphere (the predicted high-energy cutoff due to γB pair production from inner magnetosphere models for γ-ray emission was not detected), this radio component must be generated from the outer magnetosphere or even in the current sheet region outside the magnetosphere.

- *Magnetar radio emission*.—Magnetars are poor radio emitters and usually do not emit radio pulses during the quiescent state. However, they can become transient radio pulsars after bursting activities. When they emit, the radio pulses sometimes show a broad pulse profile and a flat or even rising spectrum, in apparent contrast to the pulses from normal pulsars (Camilo et al., 2007). SGR J1935+2154 was detected by FAST to show a pulsar phase five months after FRB 200418, with 795 pulses detected in 16.5 h over 13 d (Zhu et al., 2023). Unlike the radio pulses of radio pulsars, these pulses have an opposite phase with respect to the x-ray pulses from the magnetar. It is unclear whether magnetar radio emission shares the same origin as one of the two mechanisms operating in normal pulsars or has its distinct origin.

FRB emission has a typical luminosity ~ 10 orders of magnitude higher than pulsar radio emission. It is unclear whether any of the three aforementioned mechanisms can apply to FRBs.

2. Coherent curvature radiation by bunches

This mechanism has been widely discussed in both the pulsar and FRB fields. Within the pulsar context, Ruderman and Sutherland (1975) suggested that unsteady vacuum gap discharges release "sparks" composed of secondary electron-positron pairs that collide at a distance of tens of neutron star radius. Two-stream instabilities drive the formation of bunches (Usov, 1987; Melikidze, Gil, and Pataraya, 2000), which radiate coherently in curved magnetic field lines to produce pulsar radio emission from the inner magnetosphere.

The mechanism was found to be user friendly to account for the phenomenology of pulsar radio emission, including the characteristic frequency, radius-to-frequency mapping, polarization properties, etc. (Ruderman and Sutherland, 1975). The formation and maintenance of the bunches were regarded as the main drawbacks for such a mechanism (Melrose, 1978), but various suggestions to overcome these criticisms have been discussed in the literature (Melikidze, Gil, and Pataraya, 2000).

The application of this mechanism to FRBs was discussed by Katz (2014, 2018a, 2020b), Kumar, Lu, and Bhattacharya (2017), Lu and Kumar (2018), Yang and Zhang (2018), Lu, Kumar, and Zhang (2020), Wang and Lai (2020), Yang *et al.* (2020), Cooper and Wijers (2021), Wang, Jiang *et al.* (2022), and Wang, Yang *et al.* (2022). Because of the extremely high T_b of FRB emission, some novel aspects of the mechanism have been noticed. The key ingredients of such a mechanism can be summarized as follows:

- *Characteristic frequency.*—According to Eq. (94), the frequency of curvature radiation is $\nu_{CR} \sim (0.72\,\text{GHz})\gamma_{e,2}^3\rho_7^{-1}$. For 1 GHz radiation, the required electron Lorentz factor is

$$\gamma_e \simeq 110\nu_9^{1/3}\rho_7^{1/3}, \qquad (127)$$

which is in the range of 10^2–10^3 for a curvature radius ρ ranging widely from $\sim 10^7$ cm ($10R_{\text{NS}}$) to $\sim 10^{10}$ cm (around the light cylinder radius).

- *Emission power of a bunch.*—The emission power of an individual electron is

$$
\begin{aligned}
P_e &= \frac{2}{3}\frac{\gamma_e^4 e^2 c}{\rho^2} \\
&\simeq (4.6\times10^{-15}\ \text{erg s}^{-1})\gamma_{e,2}^4\rho_7^{-2} \\
&\simeq (7.2\times10^{-15}\ \text{erg s}^{-1})\nu_9^{4/3}\rho_7^{-2/3}. \qquad (128)
\end{aligned}
$$

A bunch of $N_{e,b}$ electrons would emit with a power $\sim N_{e,b}^2 P_e$. [Strictly this is the maximum value (Yang and Zhang, 2018).] The number $N_{e,b}$ in a bunch can be estimated as

$$N_{e,b} = A_b\lambda n_e \simeq A_b\lambda\zeta n_{GJ} \simeq 3\times10^{21}A_{b,9}\nu_9^{-1}\zeta_1 n_{GJ,10}, \qquad (129)$$

where ζ is the net-charge multiplicity with respect to the Goldreich-Julian density and A_b is the cross section of the bunch, whose radial size is fixed roughly as the wavelength λ of the emission (Fig. 9). The most conservative estimate gives $A_{b,\min} \sim \pi(\gamma_e\lambda)^2$, which requires the transverse coherence region to cover the wavelength in the electron comoving frame (Kumar, Lu, and Bhattacharya, 2017; Wang and Lai, 2020). The bunch cross section can in principle be much larger, up to the radius whose projection in the direction of line of sight is λ, i.e., $r_{\perp,1} \sim \sqrt{r_0\lambda}$ (the Fresnel length, Fig. 9), but is limited to the casually connected region size $r_{\perp,2} \sim \rho/\gamma$. Therefore, one can write
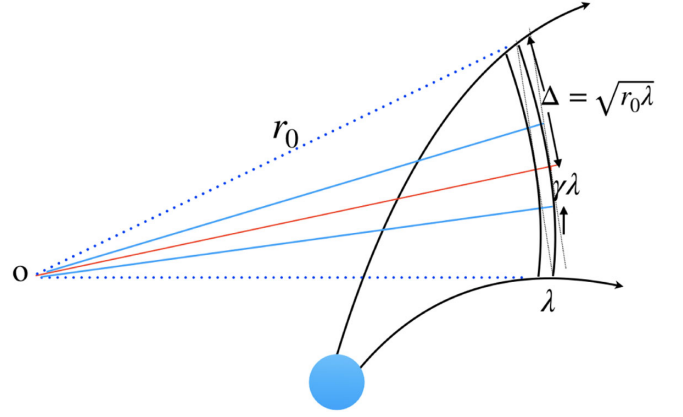

FIG. 9. Illustration of the shape of bunch. The radial size is approximately limited by the wavelength, i.e., $\sim\lambda$. The maximum transverse size is at least $\sim\gamma_e\lambda$ but can be as large as the Fresnel length $\sim\sqrt{r_0\lambda}$. Note that in order to show the geometry clearly the bunch size is greatly exaggerated. In reality, the distances from the two edges of the bunch to the NS as well as r_0 are similar to each other.

$$
\begin{aligned}
A_{b,\max} &\simeq \min[\pi r_0\lambda, \pi(\rho/\gamma)^2] \\
&\simeq \min[(9.4\times10^8\ \text{cm})\,r_{0,7}\nu_9^{-1}, (3.1\times10^{10}\ \text{cm})\rho_7^2\nu_9^{-2}].
\end{aligned}
$$
$$(130)$$

In Eq. (130) r_0 is the distance between the FRB emission region and the effective origin of the field line tangents.[16] This is especially the case when field lines are nearly parallel in the outer magnetospheres.

- *Observed luminosity.*—Because of the light propagation effect discussed in Sec. IV.A, the observed power of an individual emitting electron is greater than its emitted power by a factor of $\sim(1-\beta_e\cos\theta)^{-1} \sim \gamma_e^2$ (when $\theta \lesssim 1/\gamma_e$). Considering the possible existence of N_b independent bunches that contribute to the observed luminosity at an epoch, one can write the total true luminosity (not isotropic equivalent) as

$$
\begin{aligned}
L &\simeq N_b N_{e,b}^2 P_e\gamma_e^2 \\
&\simeq (7.8\times10^{38}\ \text{erg s}^{-1})N_{b,6}A_{b,9}^2\zeta_1^2 n_{GJ,10}^2, \qquad (131)
\end{aligned}
$$

where N_b, A, and n_{GJ} are normalized to their respective typical values [N_b can be estimated as $\Delta r/\lambda = (3.3\times10^5\ \text{cm})\Delta r_7\nu_9$, where Δr is the depth of the field line that contributes to instantaneous radiation]. Note that ν_9 and ρ_7 are apparently canceled out in Eq. (131). This "true" luminosity from the model can be compared with the beaming corrected luminosity derived from the observed isotropic luminosity, as discussed in Sec. IV.D, i.e.,

---

[16] The introduction of r_0 is for a purely geometric purpose to estimate the maximally allowed size of the bunch. Physically, particles are ejected from the inner magnetosphere of the neutron star, and whether there is transverse coherence up to $\pi r_0\lambda$ depends on the detailed particle injection and bunch formation processes.

$$L \simeq L_{\rm iso} \max[\theta_j^2/4, (4\gamma_e^2)^{-1}], \qquad (132)$$

where the solid angle of an individual FRB $\delta\Omega$ is written as $\pi\theta_j^2$, with θ_j the half opening angle of the min-jet. Note that when $\theta_j \leq \gamma_e^{-1}$, our treatment is consistent with that of Kumar, Lu, and Bhattacharya (2017), who used a γ_e^4 parameter to make a connection between the emitted power and the observed isotropic luminosity. Our treatment is more general and includes the $\theta_j > \gamma_e^{-1}$ regime. One can see that for plausible parameters, the observed FRB isotropic-equivalent luminosity can be reproduced.

- *Cooling time and the required $E_\parallel$.*—Kumar, Lu, and Bhattacharya (2017) first pointed out that for models invoking curvature radiation by bunches a steady $E_\parallel$ is needed in the magnetosphere to continuously inject energy into the bunches to maintain the observed luminosity for the typical FRB duration. Consider a bunch of $N_{e,b}$ electrons radiating coherently. The total energy is $E_b = N_{e,b}\gamma_e m_e c^2$ and the total emission power is $N_{e,b}^2 P_e$. Thus, the cooling timescale is

$$t_c = \frac{\gamma_e m_e c^2}{N_{e,b} P_e} \simeq (4.5 \times 10^{-12} \text{ s}) A_{b,9}^{-1} \rho_7 \zeta_1^{-1} n_{\rm GJ,10}^{-1}. \qquad (133)$$

This is much shorter than the typical FRB duration. To maintain FRB emission power, the electrons need to continuously gain energy from an electric field $E_\parallel$ such that $(N_{e,b}e)E_\parallel c = N_{e,b}^2 P_e$. This gives

$$E_\parallel = \frac{N_{e,b} P_e}{ec} \simeq (1.4 \times 10^6 \text{ esu}) \nu_9^{1/3} \rho_7^{-2/3} A_{b,9} \zeta_1 n_{\rm GJ,10}. \qquad (134)$$

The existence of such a field is required to apply the coherent curvature radiation in bunches to explain FRB emission. Kumar and Bošnjak (2020) proposed that such an $E_\parallel$ may be provided by the propagation of Alfvén waves to a charge starved region at an altitude of tens of neutron star radii. Lu, Kumar, and Zhang (2020) argued that such a mechanism can account for FRBs with a wide range of luminosities. Cooper and Wijers (2021) investigated the maximum luminosity of this mechanism by considering the effect of the induced current of the emitting bunches. They confirmed that the mechanism can generate emission with FRB luminosities. Qu, Zhang, and Kumar (2023) showed that the existence of such an $E_\parallel$ is essential to overcome the plasma suppression effect for bunched coherent emission (Gil, Lyubarsky, and Melikidze, 2004; Lyubarsky, 2021).

- *Spectrum.*—The radiation spectrum of coherent curvature radiation by three-dimensional bunches in a realistic pulsar magnetosphere was calculated by Yang and Zhang (2018) and Wang, Yang et al. (2022). The spectrum was found to be in the form of a broken power law separated by a few characteristic frequencies defined by the length and the opening angle of the bunch. The spectral indices

of different segments depend on the relative ordering among the characteristic frequencies, and the high-frequency spectral index depends on the power-law index of the emitting electrons p. The possible self-absorption effect by other bunches was studied by Ghisellini and Locatelli (2018). If charges are spatially separated, the shape of the coherent spectrum would have a narrower peak than the regular case (Yang et al., 2020). In general, to achieve narrow spectra for the bunch models, one needs to invoke convolution of the intrinsically broad spectrum of individual bunched charges and their spatial distribution (Katz, 2018a).

- *Polarization.*—Both *O*-mode and *X*-mode polarized waves can be generated with curvature radiation (Wang, Wang, and Han, 2012; Kumar, Lu, and Bhattacharya, 2017). A nearly 100% linear polarization degree is expected if the observer is within the $1/\gamma_e$ cone of the electron emission beam, but circular polarization can develop outside the emission cone (Tong and Wang, 2022; Wang, Jiang et al., 2022; Wang, Yang et al., 2022; Qu and Zhang, 2023). Depending on the location of the emission region, the polarization angle can either display a swing (for an inner magnetospheric location and/or a rapid rotation of the magnetosphere), as seen in radio pulsars within the framework of the rotating vector model (Radhakrishnan and Cooke, 1969), or stay nearly flat (for an outer magnetospheric location and/or a slow rotation of the magnetosphere).

- *Radius-to-frequency mapping and frequency down-drifting.*—Wang et al. (2019) showed that there is a simple interpretation of the frequency down-drifting feature observed in some FRBs. Since charged bunches need to be radiation-reaction limited within this model (balance between $E_\parallel$ acceleration and curvature cooling), γ_e may maintain a roughly constant value along field lines. Since the curvature radius continuously increases as the bunches move away from the magnetosphere, the curvature radiation frequency continuously decreases with increasing height. Suppose that several bunches in adjacent field lines were launched simultaneously from the base. As the magnetosphere rotates, the line of sight always catches emission from lower altitudes (and hence with a higher frequency) first and the emission from higher altitudes (and hence with a lower frequency) later, so frequency down-drifting should be commonly expected.[17] Allowing that the bunches can be ejected at somewhat different times, Wang, Xu, and Chen (2020) showed that occasionally a frequency up-drifting FRB may be observed, but the down-drifting pattern should prevail. This is consistent with observations (D. J. Zhou et al., 2022).

Despite the success of this simple model to interpret a broad range of pulsar and FRB phenomenology, the mechanism has been criticized by several authors:

---

[17]Lyutikov (2020b) later proposed a similar idea to interpret frequency down-drifting using radius-to-frequency mapping, even though the radiation mechanism was not specified.

- Melrose (1978) pointed out that coherent curvature radiation by bunches suffers from the difficulties of bunch formation and maintenance. The bunch formation mechanisms have been explored extensively in the pulsar field. The common ingredient of the models is a two-stream instability (Melikidze, Gil, and Pataraya, 2000), which is likely realized in the violent event that powers an FRB. The maintenance of bunches is more difficult to realize. Strong repulsion forces within the bunches tend to disperse the bunch spatially and the radiation reaction tends to disperse the bunch in momentum space (Katz, 2018a, 2020b). However, since the FRB duration is short, the maintenance mechanism only needs to apply for a millisecond duration.

- Lyubarsky (2021) emphasized that the plasma effect, which tends to limit brightness temperature and is moderately severe for pulsar radio emission (Gil, Lyubarsky, and Melikidze, 2004), becomes substantial in suppressing coherent emission from FRBs. If the bunch moving with γ_e is surrounded by a plasma moving with γ_p, Lyubarsky (2021) suggested that the emission power of the bunch $N_{e,b}^2 P_e$ is suppressed by a large factor of the order of 10^{-10}. Qu, Zhang, and Kumar (2023) revisited the arguments of Gil, Lyubarsky, and Melikidze (2004) and Lyubarsky (2021) and found that the plasma suppression effect is not important in FRB problems. If a strong $E_\parallel$ exists in the emission region, as expected in the realistic FRB models (Kumar, Lu, and Bhattacharya, 2017), there is essentially no suppression if the bunch is in the radiation-reaction-limited regime for coherent curvature radiation.

- The curvature radiation spectrum, like the synchrotron spectrum, might be too broad to interpret the narrowband spectrum observed in some FRBs, especially the repeaters. Charge separation can alleviate this criticism (Katz, 2018a; Yang et al., 2020).

3. Coherent ICS emission by bunches, free-electron laser, and linear acceleration emission

Besides curvature radiation, there is another family of models that invokes vacuumlike coherent mechanisms that do not intrinsically depend on the dispersive properties of the plasma. Within these models, bunched particles resonate coherently in some low-frequency waves, of either the electromagnetic or the electrostatic type, and inverse Compton scatter the waves to higher frequencies to make FRBs. A relatively simple model is to invoke low-frequency electromagnetic waves, which might be excited near the neutron star surface by crustal oscillations (Zhang, 2022). Usually it is believed that crustal oscillations would excite Alfvén waves, and indeed the bulk of the energy that eventually powers an FRB is likely carried by Alfvén waves. On the other hand, if a small amount of oscillation energy would be converted to electromagnetic waves by coherently oscillating charges in the near-surface magnetosphere, then the waves (all modes for a quasiparallel configuration and X mode only for a quasiperpendicular configuration) would penetrate through the magnetosphere unimpeded. Suppose that there are relativistic bunched charges moving with a bulk

Lorentz factor γ. The low-frequency electromagnetic waves with angular frequency ω_0 and frequency $\nu_0 = \omega_0/2\pi \sim 10^4$ Hz would be upscattered to a frequency

$$\omega = \gamma^2 \omega_0 (1 - \beta \cos\theta_i), \tag{135}$$

$$\nu = (1 \text{ GHz}) \gamma_{2.5}^2 \nu_{0,4} (1 - \beta \cos\theta_i), \tag{136}$$

where θ_i is the incident angle. This inverse Compton scattering (ICS) model has been considered to interpret pulsar radio emission (Qiao and Lin, 1998; Xu et al., 2000; Qiao et al., 2001), and its promise to interpret FRB emission was discussed by Zhang (2022).

The advantage of the ICS mechanism is that the emission power of a single particle $P_e^{\text{ICS}} \sim (1.6 \times 10^{-7} \text{ erg s}^{-1})(\delta B_{0,6})^2 r_8^{-2}$ (where δB_0 is the oscillation amplitude of the magnetic field of the electromagnetic waves and r is the radius of the emission region) is much greater than that of the curvature radiation $P_e^{\text{CR}} \sim (4.6 \times 10^{-15} \text{ erg s}^{-1})\gamma_{2.5}^4 \rho_8^{-2}$. As a result, the required degree of coherence to interpret the FRB high brightness temperature is greatly reduced. Indeed, even if one adopts the most conservative bunch cross section $A_{b,\min} = \pi(\gamma\lambda)^2$, the required $N_{e,b}$ is so low that a charge number density of the order of n_{GJ} is already enough to account for the FRB luminosity. As a result, the bunches do not need to have a large plasma density, and the criticism of bunch emission suppression due to the plasma effect (Lyubarsky, 2021) is greatly alleviated (Qu, Zhang, and Kumar, 2023). Even a small fluctuation in charge number density with respect to the background Goldreich-Julian density (Yang and Zhang, 2018) would be adequate to produce bunched ICS radiation such that the criticisms of bunch formation and maintenance (Melrose, 1978) would also be alleviated. The frequency of the scattered waves [Eq. (136)] depends on ω_0, γ, and θ_i. All could be nearly constant within an FRB (γ is radiation-reaction limited), so the bunched coherent ICS mechanism has the advantage of generating narrower spectra than curvature radiation does, which is consistent with observations (D. J. Zhou et al., 2022). The frequency down-drifting feature may also be produced via a radius-to-frequency mapping feature or the intrinsic damping of the low-frequency waves toward longer wavelengths (Zhang, 2022). This mechanism can also produce intrinsic circular polarization with a proper viewing geometry (Qu and Zhang, 2023).

In the case that vacuumlike electromagnetic waves are not excited from the near-surface region, coherent radio emission may still be excited by relativistic particles scattering off an oscillating electric field along the magnetic field line via the amplified linear acceleration emission (ALAE) or off Alfvén waves via the free-electron laser (FEL) mechanism.

ALAE was introduced by Melrose (1978) as a mechanism to replace bunched curvature radiation to interpret pulsar radio emission. It was further developed by Rowe (1995). It invokes an oscillating $E_\parallel$ along the direction of particle motion, with particles radiating coherently in such an accelerating field. This mechanism has not been investigated in detail within the FRB context. Since the emission occurs nearly at the neutron star surface, it is unclear whether the mechanism can produce

the observed high T_b of FRBs without being absorbed or scattered within the inner magnetosphere (Ioka, 2020; Beloborodov, 2021a).

The FEL mechanism invokes the interaction between an Alfvén wave disturbance (also called a wiggler) and a relativistically moving bunch. This mechanism has been studied intensively in the laboratory (Benford and Weatherall, 1992) and was discussed by Fung and Kuijpers (2004) within the pulsar radio emission context. It was investigated by Lyutikov (2021) within the FRB context. The characteristic angular frequency of emission is defined by

$$\omega \simeq 4\gamma^2(ck_w), \qquad (137)$$

where k_w is the wave number of the low-frequency wiggler waves, similar to the direct ICS case Eq. (135), where ck_w is replaced by ω_0. The trajectory of bunched relativistic electrons in wiggling Alfvén waves can be solved. The resulting emission spectrum has a narrow band, which can interpret the spectral feature of the Crab pulsar and the narrow spectra of repeating FRBs (Lyutikov, 2021). The mechanism is also more powerful than curvature radiation, and hence satisfies the brightness temperature constraint more easily. In general the FEL mechanism (Lyutikov, 2021) and coherent ICS mechanism with bunches (Zhang, 2022) are intrinsically similar mechanisms that share several common features and advantages in interpreting FRB coherent radio emission.

4. Magnetospheric maser mechanisms

The previously discussed bunching mechanisms do not invoke negative absorption or growth of plasma modes that depend on the dispersive properties of the plasma. In this section, I discuss several magnetospheric maser mechanisms for coherent radio emission. These mechanisms include vacuum masers that invoke negative absorption of electromagnetic radiation as if in an vacuum, and plasma masers that invoke growth of plasma modes. For the latter models to work, several requirements are needed: (1) The plasma should support modes whose frequency falls into the observed frequency band (for instance, gigahertz), (2) there should be an unstable particle distribution in the relevant frequency band, which should resonate with the plasma mode, (3) the mode should grow rapid enough to reach the desired amplitude to account for the high brightness temperature, and (4) the plasma mode should eventually escape the region as electromagnetic waves. To date none of these magnetospheric models have been found suitable to interpret FRB radio emission. As a result, even though the following mechanisms have been introduced to interpret coherent radio emission from other astronomical objects, thus far they have not been found to be successful in interpreting FRB emission; see Lu and Kumar (2018) for a critical study of maser mechanisms within the context of FRBs. Nonetheless, they are listed here for completeness:

- *Relativistic plasma emission.*—Plasma emission is a multistage process (Melrose, 2017). The first step is to drive a longitudinal Langmuir wave through a streaming instability between a fast beam and a background plasma. The subsequent stages include amplification of the Langmuir turbulence and the conversion of the plasma mode to electromagnetic waves that could eventually escape the magnetosphere. The characteristic emission frequency should be the plasma frequency ω_p or the boosted plasma frequency $\Gamma\omega_p$ in the relativistic version. Even though plasma emission has been identified as the main mechanism producing coherent solar radio bursts, it has not been successful in interpreting pulsar radio emission. The main reason for this is that the instability growth rate is too small due to the limitation of the relatively small plasma property gradients.

- *Electron cyclotron maser emission.*—This mechanism involves plasma maser emission at the nonrelativistic cyclotron frequency ω_B and its harmonics $s\omega_B$, with decreasing amplitudes at higher s values. The mechanism was found to be responsible for the decametric radio emission of Jupiter and the auroral kilometric radiation of Earth (Melrose, 2017). However, within a neutron star magnetosphere (especially for a magnetar) ω_B is usually much higher than the radio frequency, so this mechanism is usually not relevant for magnetospheric models.[18]

- *Curvature radiation maser.*—A curvature radiation maser is not possible for a rotating dipole because there is no solution for negative absorption. However, if the pulsar magnetosphere is distorted, under certain conditions negative absorption would be possible for curvature radiation (Luo and Melrose, 1995). Such a model is not attractive for interpreting FRBs, since it is unclear how the specific magnetospheric configuration might be realized in an FRB-emitting source.

- *Anomalous cyclotron-Cherenkov and Cherenkov drift resonances.*—Instabilities occur when a dispersion relation has a term whose denominator approaches zero, which is termed a resonance. In a pulsar magnetosphere, maser-type plasma instabilities can operate at the anomalous cyclotron-Cherenkov resonance $\omega - k_\parallel v_\parallel + \omega_B/\gamma = 0$ (γ is the plasma Lorentz factor in the pulsar frame) and the Cherenkov drift resonance $\omega - k_\parallel v_\parallel - k_\perp u_d = 0$ (u_d is the drift velocity). Even though this mechanism is a plausible candidate to account for pulsar radio emission (Lyutikov, Blandford, and Machabeli, 1999), they are not favored in interpreting FRBs, because the conditions for the maser mechanisms to operate either cannot be realized or demand unreasonable parameters (Lu and Kumar, 2018).

5. Other magnetospheric mechanisms

Two more magnetospheric coherent mechanisms have been proposed to interpret FRB emission that deserve special discussion. The first model was proposed by Lyubarsky (2020). This model invokes a large-scale magnetic perturbation to form a magnetic pulse, which strongly compresses the magnetospheric plasma and pushes it away. The pulse propagates from the flare site within the magnetosphere

---

[18]For slow rotating nonmagnetar pulsars, the condition may be satisfied. However, the energetics of the neutron star would not be large enough to power FRBs.

outward and eventually reaches the current sheet that separates the oppositely oriented magnetic fields beyond the light cylinder. The FRB is powered by the enhanced magnetic reconnection in the current sheet region. It is conjectured that coalescence of magnetic islands in the reconnection current sheet produces magnetosonic waves that propagate on top of the magnetic pulse and eventually escape as electromagnetic waves. The characteristic frequency is defined by the dimension of the magnetic islands $\xi a'$, where a' is the width of the current sheet, such that

$$\omega = \delta\omega' = \delta\frac{c}{\xi a'}, \tag{138}$$

where the primed quantities are measured in the rest frame of the magnetic pulse and δ is the Doppler factor of the pulse. To match the observed FRB frequency, $\xi \sim 10$–100 is required. The emission is polarized along the rotation axis of the magnetar. The advantage of this model is that the emission site is slightly beyond the light cylinder, which negates the criticisms regarding FRB propagation within the magnetosphere (Beloborodov, 2021a). PIC numerical simulations of such a scenario have been carried out that show the excitement of narrowband gigahertz emission (Mahlmann *et al.*, 2022). An alternative radiation mechanism within this scenario is bunched ICS of relativistic electrons accelerated from the current sheet off the low-frequency waves generated from the inner magnetosphere (Zhang, 2022).

The second model is the direct electromagnetic wave generation from nonuniform pair production across different field lines. Within the framework of radio pulsars, Timokhin (2010) and Timokhin and Arons (2013) showed that unsteady pair production is the norm near pulsar polar caps, regardless of whether there is a strong binding of particles from the pulsar surface. Through 1D simulations, they showed the existence of broadband superluminal electrostatic waves in the unsteady pair-screening region, which they suspected was a candidate pulsar radio emission mechanism. Philippov, Timokhin, and Spitkovsky (2020) showed from large-scale two-dimensional kinetic plasma simulations that such non-steady pair production and screening of electric fields along the magnetic field lines by freshly produced pairs can naturally generate electromagnetic waves that can escape the magnetosphere. They proposed that such a mechanism could be responsible for the coherent radio emission of radio pulsars. Within the context of FRBs, Wadiasingh *et al.* (2020) speculated that such a mechanism may power FRBs from a magnetar magnetosphere. Yang and Zhang (2021) developed an analytical toy model for this process and showed that the mechanism can indeed apply to FRBs given that nonsteady, nonuniform pair production can be realized in an FRB environment. They argued that crustal oscillations of a magnetar could be the engine for such nonsteady, nonuniform pair production processes.

6. Transparency of FRBs from magnetospheres

One criticism regarding the magnetospheric mechanism of FRBs is that the FRB waves may undergo strong scattering by the magnetospheric plasma such that a high brightness temperature would not be achievable (Beloborodov, 2021a). Owing to their high intensities, FRB waves have a large oscillation amplitude for the wave $\vec{E}_w$ field (and also the wave $\vec{B}_w$ field) such that the dimensionless amplitude parameter (Luan and Goldreich, 2014)

$$a \equiv \frac{eE_w}{m_e c\omega} \simeq \frac{eB_w}{m_e c\omega} = \frac{\omega_{B,w}}{\omega} \gg 1 \tag{139}$$

in the magnetosphere; see Sec. VIII.C for further discussion of the large-amplitude-wave effect. This amplitude factor a denotes how fast an electron moves in response to the waves, and when $a \gg 1$ the electron speed approaches the speed of light. Without an external magnetic field, the electron would move under both the oscillating E_w field and the Lorentz force due to B_w, with its trajectory taking a figure-eight shape (Sarachik and Schappert, 1970; Yang and Zhang, 2020). The electron is accelerated by a Lorentz factor of the order of a. The scattering cross section can be generally defined as $\sigma = P/S$, where P is the emitting power and S is the received photon flux. Because of the relativistic motion of the electron, the emitted power is enhanced by a factor of $\sim a^2$ with respect to Thomson scattering such that (Sarachik and Schappert, 1970; Yang and Zhang, 2020)

$$\sigma \sim a^2 \sigma_T. \tag{140}$$

In a neutron star magnetosphere with background B, the situation is more complicated. When $B \gg B_w$, the electron motion is dictated by B rather than B_w, so the enhancement of σ [Eq. (140)] would not occur. In a magnetosphere, since $B \propto r^{-3}$ for a dipolar configuration and $B_w = \sqrt{L/cr^2} \propto r^{-1}$ for an EM wave, there will be a point where B drops below B_w. Recalling that $\omega_B = eB/m_e c$, this condition can also be written as

$$a > \frac{\omega_B}{\omega}. \tag{141}$$

The scattering cross section is greatly increased and the optical depth is greatly enhanced,

$$\tau_{es} \sim n\sigma r_c \simeq 0.4\tilde{\sigma}L_{42}^2\xi B_{s,15}^{-1}\nu_9^{-2}P^{-1}R_6^{-4}. \tag{142}$$

In Eq. (142) $n = \xi n_{GJ}$, $\tilde{\sigma} = \sigma/[a(r_c)]^2\sigma_T$ is the cross section normalized to $a^2\sigma_T$, and $r_c = (B_s R^3)^{1/2}(c/L)^{1/4} \simeq (4.2 \times 10^8 \text{ cm})L_{42}^{-1/4}B_{s,15}^{1/2}R_6^{1/2}$, which is the critical radius at which $B_w = B$. This estimate suggests that the FRB waves would indeed become opaque to Thomson scattering in a magnetar magnetosphere if L and ξ are large (Beloborodov, 2021a). The situation worsens since the relativistic motion of electrons in complicated trajectories would radiate γ rays, which may produce additional pairs to increase the opacity.

However, the aforementioned arguments are based on two assumptions: (1) the magnetospheric plasma is essentially at rest and (2) the angle between wave propagation and the local B field θ_{kB} is nearly 90°, i.e., the FRB is trying to penetrate through the closed field line region. Qu, Kumar, and Zhang (2022) argued that both assumptions are likely to be invalid in

realistic magnetospheric emission models for FRBs. Various mechanisms (the standard pulsar mechanism, Alfvén wave propagation, and ponderomotive force acceleration) likely drive a relativistically moving plasma in the open field line region of a magnetar magnetosphere. The propagation of the intense FRB waves also tends to align the $\vec{k}$ and $\vec{B}$ vectors such that θ_{kB} is likely $\ll 1$. Both effects would reduce the scattering optical depth significantly and it has been shown that FRBs are transparent in a magnetar magnetosphere even for high-luminosity FRBs with a large pair multiplicity if the plasma Lorentz factor $\gamma_p > 10^2$ (Qu, Kumar, and Zhang, 2022).

FRBs are likely associated with x-ray and γ-ray photons emitted from a magnetar magnetosphere. The transparency of FRBs depends on the competition between the FRB and x-ray luminosities. Ioka (2020) showed that FRB photons can break out of the pair-rich magnetopshere with radiation pressure if the FRB emission radius is larger than a few tens of NS radii. As long as the work done by the FRB waves on the $e^{\pm}$ is small compared to the initial FRB energy, the FRB can successfully break out the magnetosphere. Ioka (2020) showed that the breakout condition is satisfied in the high-L_{FRB} low-L_X regime. According to this result, SGR giant flares may not be associated with successful FRBs, since the bright x-ray emission would likely choke the FRB jet; see Katz (2016) for discussion of alternative possibilities of nondetection of an FRB associated with the SGR 1806-20 giant flare. This is consistent with the radio luminosity upper limit of the SGR 1806-20 giant flare (Tendulkar, Kaspi, and Patel, 2016).

C. Relativistic shock models

The second general type of models invokes relativistic shocks to generate coherent radio emission. The term *synchrotron maser* has been adopted to describe several significantly different scenarios. I now discuss the three versions of the model in decreasing order according to their relevance to the "synchrotron maser," which incidentally is also in reverse order of popularity.

1. Vacuum synchrotron maser

The first model is literally the synchrotron maser. For a synchrotron-emitting source, the synchrotron absorption coefficient can be written in the form (Rybicki and Lightman, 1979; Ghisellini, 2017; Waxman, 2017; Lu and Kumar, 2018)

$$\alpha_\nu = -\frac{1}{2m_e\nu^2}\int_1^\infty \gamma^2 j_\nu(\gamma,\psi)\frac{\partial}{\partial\gamma}\left(\frac{dN/d\gamma}{\gamma^2}\right)d\gamma, \qquad (143)$$

where $j_\nu(\nu,\psi)$ is the viewing-angle-dependent emissivity for a single electron (in $\mathrm{erg\,s^{-1}Hz^{-1}\,sr^{-1}}$, unlike the volume emissivity commonly defined). One can also write the net absorption cross section per particle as (Ghisellini and Svensson, 1991; Ghisellini, 2017; Lu and Kumar, 2018)

$$\sigma_{a,\nu} \simeq \frac{1}{2m_e\nu^2}\frac{1}{\gamma^2}\frac{\partial}{\partial\gamma}[\gamma^2 j_\nu(\gamma,\psi)]. \qquad (144)$$

A vacuum maser is possible when either $\sigma_{a,\nu}$ is negative [$\gamma^2 j_\nu(\gamma,\psi)$ is a decreasing function of γ] or α_ν is positive (the $dN/d\gamma$ distribution is steeper than γ^{-2}, i.e., there is population inversion).

Ghisellini (2017) found that if the emission region has an extremely ordered magnetic field and if the emitting electrons have a narrow distribution for both pitch angle and energy, $\sigma_{a,\nu} < 0$ is possible in a certain range of the viewing angle $\psi > 1/\gamma_e$, where γ_e is the electron Lorentz factor. Even though relativistic shocks are not specified in the model discussed by Ghisellini (2017), the required magnetic field strength B and electron energy γ_e for the characteristic synchrotron frequency to fall into the FRB band are consistent with the typical values for shock models. The plasma effect is not important in this model, so the emission is of the "vacuum" type.

Even though the mechanism is clean and straightforward, the difficulties of the model include how to maintain an extremely ordered B field (within a $1/\gamma_e$ angle), how to accelerate particles to maintain a narrow pitch angle distribution (again within a $1/\gamma_e$ angle), and how to accelerate particles to maintain a narrow energy distribution. Known astrophysical particle acceleration mechanisms, such as relativistic shocks and magnetic reconnection, usually accelerate particles to a power-law energy distribution, and the accelerated relativistic electrons typically have a wide angular distribution with respect to the local B field. Perturbations usually introduce wiggles of magnetic field lines. As a result, this mechanism may not be realized in nature due to the contrived physical conditions required.

2. Plasma synchrotron maser in nonmagnetized relativistic shocks

Accelerated particles in relativistic shocks usually have an energy distribution $dN/d\gamma \propto \gamma^p$ with $p \sim -2$ above the minimum Lorentz factor γ_m. Maser emission is therefore impossible for the frequency range defined by $\gamma > \gamma_m$ since α_ν is positive. Nonetheless, population inversion ($p > 2$) may be possible at $\gamma < \gamma_m$ (Sagiv and Waxman, 2002; Waxman, 2017). In the extreme case, a sharp cutoff of the γ distribution below γ_m mimics a δ function, which is much steeper than γ^2. In the frequency space, maser emission occurs at (Sagiv and Waxman, 2002)

$$\nu < \nu_{R^*} = \min[\gamma_m, (\nu_p/\nu_B)^{1/2}]\nu_p, \qquad (145)$$

where ν_{R^*} is the modified Razin frequency below which the plasma effect becomes dominant, $\nu_p = \omega_p/2\pi$, and $\nu_B = \omega_B/2\pi$. The relativistic beaming effect for synchrotron radiation is suppressed because of the role played by the refractive index n_r (Rybicki and Lightman, 1979). The traditional synchrotron radiation is suppressed, but the possibility for maser emission is opened. This mechanism is a plasma version of the synchrotron maser, and it applies to a weakly magnetized plasma with $\omega_B \ll \omega_p$. In a hydrodynamical shock, one usually defines the microscopic parameters ϵ_e and ϵ_B as the fraction of shock internal energy that are distributed in electrons and magnetic fields. Observations of GRBs show that typically $\epsilon_B \ll \epsilon_e \ll 1$; see Kumar and

Zhang (2015) and references therein. Since $\nu_p/\nu_B = \omega_p/\omega_B \sim (\epsilon_e/\epsilon_B)^{1/2}$, the condition for plasma synchrotron maser emission is satisfied.

For this model to work, a weakly magnetized central engine is preferred. Demanding model parameters to satisfy FRB observational constraints, Long and Pe'er (2018) showed that neutron stars with surface magnetic fields $B_* \leq 10^{11}$ G are preferred. This is at odds with the observational constraint making magnetars responsible for at least some FRBs. In addition, since the emission region is weakly magnetized, such a model does not predict the extremely high polarization degree that is observed in the majority of FRBs. As a result, this mechanism, if relevant, would not be responsible for the majority of FRBs.

3. Bunched coherent cyclotron and synchrotron radiation in highly magnetized relativistic shocks

Another version of the relativistic shock models invokes a highly magnetized upstream. The upstream magnetic field lines are highly ordered. As the shock propagates into the magnetized medium, magnetic fields are amplified and particles coherently gyrate around these field lines, forming a "ring" in the momentum space, even though they can spread in a wide position space. They then radiate coherently as a global bunch at the gyration frequency $\sim \omega_B' = eB'/m_e c$ and its harmonics, where B' is the downstream magnetic field strength in the comoving frame of the fluid. The observed frequency is Doppler boosted by a factor of the bulk Lorentz factor Γ if the shock moves toward the observer relativistically. This mechanism, even still called the synchrotron maser, is in fact more analogous to a bunched coherent cyclotron and synchrotron radiation mechanism (the electron Lorentz factor is typically a few), even though bunching occurs in the momentum space. The mechanism was introduced to the FRB field by Lyubarsky (2014) and studied by various teams to interpret FRB observations (Beloborodov, 2017, 2020; Metzger, Margalit, and Sironi, 2019; Lu, Kumar, and Zhang, 2020; Margalit, Metzger, and Sironi, 2020; Margalit *et al.*, 2020; Yu *et al.*, 2021). The physical process of this mechanism has been verified via particle-in-cell numerical simulations (Plotnikov and Sironi, 2019; Babul and Sironi, 2020; Sironi *et al.*, 2021). This mechanism is physically robust (with some requirements such as an ordered B field and cold plasma) and user friendly in interpreting observations. As a result, it is the most competitive mechanism within the relativistic shock model category.

The features, strengths, and weaknesses of this model can be summarized as follows:

- The most important condition for such a mechanism to operate is the existence of ordered magnetic fields in the upstream. Such a feature allows electrons to gyrate coherently in momentum space so that their cyclotron or synchrotron radiation power could be coherently added. A commonly suggested scenario is that an FRB magnetized pulse collides with a magnetized magnetar wind that carries a global ordered B field. The FRB is emitted in the forward shock region. There are two versions of this model: the external shock type in which the upstream is an electron-ion wind produced from a previous

magnetar flare (Metzger, Margalit, and Sironi, 2019) and the internal shock type in which the upstream is a relativistic rotationally powered electron-positron pair wind (Beloborodov, 2020). In any case, because of the highly ordered magnetic field, a high linear polarization degree is expected (Qu and Zhang, 2023). The linear polarization angle is expected to stay constant during each burst, as has been observed with some repeaters (Michilli *et al.*, 2018; Jiang *et al.*, 2022). For the same reason, the conditions for this maser mechanism to operate under are also demanding. Irregularities in the field configuration would greatly suppress coherent emission. In addition, a rapid swing of the linear polarization angle across individual bursts (Luo, Men *et al.*, 2020) poses a significant challenge to such a model.

- Another condition for such a mechanism to operate is that the upstream media should remain cold. Random motion of electrons in a hot plasma would smear up or even destroy the ring in the momentum space, leading to suppression of the coherent emission (Babul and Sironi, 2020). As a result, this feature poses a constraint on the waiting time of successive FRBs within the external shock model. Shortly after a collision, both the shocked wind and the shocked FRB ejecta would be hot. The magnetic field configurations may also be distorted due to the irregularities introduced during the collision. If another FRB pulse collides into this remnant of a previous collision, strong coherent emission would likely be suppressed. A long waiting time of the order of $\sim$100 s would be reasonable (Metzger, Margalit, and Sironi, 2019), which is consistent with the second peak of the waiting time distribution for active repeaters (D. Li *et al.*, 2021; Xu *et al.*, 2022). However, active repeaters also have another peak in the waiting time distribution, which is of the order of milliseconds (D. Li *et al.*, 2021; Xu *et al.*, 2022). These closely connected bursts, also known as burst storms (Hewitt *et al.*, 2022) or burst clusters (D. J. Zhou *et al.*, 2022), pose a challenge to the external shock version of this model. This is not an issue for magnetospheric models, since different pulses are related to different emission regions in a rotating magnetosphere as they sweep across the line of sight.

- The magnetization parameter

$$\sigma \equiv \frac{B^2}{4\pi\Gamma\rho c^2} = \frac{B'^2}{4\pi\rho' c^2} \tag{146}$$

is defined as the Poynting-flux-to-kinetic-flux ratio in the lab frame or the magnetic internal energy density (magnetic energy density plus magnetic pressure) over mass density in the comoving frame. For an electron-positron plasma, one also has $\sigma = \omega_B'^2/\omega_p'^2 = \omega_B^2/\omega_p^2$, where $\omega_B = eB/\Gamma m_e c$ and $\omega_p = (4\pi n e^2/\Gamma m_e)^{1/2}$. For this mechanism to operate efficiently, the upstream σ value should be in the Goldilocks zone, with a value $\sigma \sim 1$. At smaller σ values, since magnetic energy is not dominant, global magnetic fields are likely subject to turbulent perturbation, so the field lines tend to be more

tangled. The coherent mechanism cannot operate efficiently. At higher σ values, the fraction of energy carried by particles reduces (most energy is still in magnetic fields), so the efficiency of making coherent emission also drops. PIC simulations suggest that the maser efficiency scales as $\eta \sim 10^{-3}\sigma^{-1}$ (Sironi *et al.*, 2021).[19] One interesting question regarding these models is to address why $\sigma \sim 1$ is achieved by chance at the FRB emission radius. Pulsar wind theories suggest that a pulsar wind with an initial magnetization $\sigma_0 \gg 1$ tends to reach $\sigma \sim \sigma_0^{2/3}$ at the sonic point where the wind speed is as high as the fast sonic wave speed such that the magnetic "piston" losses pressure to accelerate the outflow (Li, Chiueh, and Begelman, 1992). Beyond this radius, magnetic acceleration is slow (unless there is an external pressure confinement to maintain a significant magnetic pressure gradient), so it is difficult to reduce σ down to unity. In general this mechanism predicts a relatively low radio emission efficiency $\eta \ll 10^{-3}$, suggesting that FRBs should be accompanied by bright high-energy emission in x rays (Margalit *et al.*, 2020) or optical emission (Beloborodov, 2020). It also suggests that the total energy budget required in the shock models is generally higher than that required in the magnetospheric models. It turned out that the Galactic FRB 200428 has an x-ray-to-radio-luminosity ratio of the order of $\sim 10^4$, which can be accounted for from both models (Lu, Kumar, and Zhang, 2020; Margalit *et al.*, 2020). However, active repeaters rFRB 20121102A and rFRB 20201124A already have a high total energy budget in the radio band during their active bursting periods. This requires that the radio efficiency not be much smaller than 10^{-3} in order to satisfy the total energy budget of the magnetars (D. Li *et al.*, 2021; Xu *et al.*, 2022; Zhang *et al.*, 2022).

- In the downstream comoving frame the characteristic frequency for maser emission is ω'_{B} (Sironi *et al.*, 2021), which is defined by the strength of upstream magnetic field B at the emission radius R_{FRB}, bulk Lorentz factor Γ, and the central engine parameters (such as the surface magnetic field B_s and the spin period P of the magnetar). Demanding the observed frequency $\Gamma\omega'_{\mathrm{B}}$ to be approximately in the gigahertz regime and combining it with other constraints (for instance, R_{FRB} as the deceleration radius defined by the FRB energy, ambient density, and Γ and the duration of the FRB defined by $w = R_{\mathrm{FRB}}/c\Gamma^2$), one can place constraints on model parameters. This has been done for the Galactic FRB 20200428 (Lu, Kumar, and Zhang, 2020; Margalit *et al.*, 2020; Yu *et al.*, 2021). The general conclusion is that the observations can be

reproduced, even though some physical conditions have to be satisfied. To overcome such a fine-tuning issue, Metzger, Margalit, and Sironi (2019) argued that the peak of the FRB spectrum sweeps across a wide frequency range as it decelerates and the observer sees them only when the peak is in the radio band. This idea is also used to interpret the spectral downdrifting observed in repeating FRBs (Metzger *et al.*, 2022). On the other hand, observationally there is no systematic peak-frequency time evolution among adjacent bursts or a duration-spectral width correlation to support this speculation (D. J. Zhou *et al.*, 2022).

D. Summary

The discussion in this section can be summarized as follows:

- There are many coherent radio emission models proposed in the literature to interpret FRB emission; they generally fall into one of two categories: magnetospheric (closer-in, pulsarlike) models or relativistic shock (far-out, GRB-like) models. Some models (such as the bunched curvature radiation model and the magnetized synchrotron maser model) have been extensively studied and have demonstrated the ability of interpreting certain FRB data. Some other models (such as magnetospheric maser models and two other versions of shock maser models) have suffered from some significant criticism and thus may not be strong candidates to power FRBs. Some other models (such as bunched ICS and FEL mechanisms, reconnection in the current sheet, and nonsteady pair-production-induced radiation) deserve closer investigation and confrontation with the data. Current observations cannot pin down exactly which mechanism is at play in powering FRBs.
- Purely from a theoretical perspective, none of the proposed models are free of issues or difficulties. Within the magnetospheric models, the bunching coherent curvature radiation or ICS models demand an $E_\parallel$ to continuously inject energy into the bunches to satisfy the energy budget constraint. The origin of the $E_\parallel$ is not well identified. Various particle–low-frequency wave interaction models assume the existence of these low-frequency waves. Their existence can be justified for a neutron star model (for instance, through star quakes or glitches) but may not be justified in all types of central engine models (for instance, black hole engines). Magnetospheric models in general need to address the opacity of high-luminosity bursts, which demands a relativistically moving plasma in the magnetopshere (Qu, Kumar, and Zhang, 2022). The magnetized synchrotron maser model in relativistic shocks need to address the origin of the demanding requirements, including ordered, cold upstream plasma, the Goldilocks σ value, and model parameters required from the data.
- From the observational perspective, data can be used to differentiate among some models. In particular, the following four criteria (Zhang, 2020c) would be helpful:

---

[19]Plotnikov and Sironi (2019) suggested $\eta = 7 \times 10^{-4}\sigma^{-2}$ from an earlier 1D simulation. The results of 3D simulations by Sironi *et al.* (2021) are generally consistent with the 1D results. The difference in σ dependence is different frames used. The σ^{-2} dependence applies to the shock frame, while the σ^{-1} dependence applies to the downstream frame, which is more relevant in estimating the maser efficiency (Sironi, 2021).

1. *Polarization angle swings.*—Even though a flat PA curve can be accounted for by both shock and magnetospheric models, a significant PA swing is consistent with magnetospheric models but poses great difficulty to the shock models.
2. *Radio efficiency.*—A high-low radio emission efficiency may offer support to the magnetospheric and shock models. The constraints on efficiency may be based on the energy of the high-energy counterpart of the FRB (for instance, the x-ray burst associated with FRB 200428) or the theoretically derived total energy budget.
3. *Beaming angle.*—Magnetospheric models predict a narrower emission beam than the shock model. Therefore, the identification of narrow beaming for certain FRBs may offer support to the magnetospheric models. Evidence in support of narrow beaming may include the lack of FRBs associated with most x-ray bursts from SGR 1935+2154 (Lin *et al.*, 2020), possible detection of off-beam FRBs, or slow radio bursts (Zhang, 2021; Chen and Zhang, 2023), and the frequency-dependent periodic window of rFRB 20180916B (Li and Zanazzi, 2021).
4. *Rapid variability.*—Since $\delta t \sim R/c\Gamma^2$ [Eq. (98)], a small δt would point toward a small R (if Γ is constrained) (Beniamini and Kumar, 2020). The 60-ns variability (Nimmo *et al.*, 2021) observed in rFRB 20200120E from a globular cluster in M81 disfavors a shock origin of the FRB (Lu, Beniamini, and Kumar, 2022).

Looking ahead, upcoming abundant FRB data may shed light on the radiation mechanism of FRBs. It is optimistic to believe that data may provide clues on the location of the FRB emission (magnetospheres versus shocks), but the identification of the coherent mechanism(s) may not be easy, as the experience in understanding pulsar radio emission mechanism speaks itself. The current available data seem to support the magnetospheric origin of at least some FRBs. It is possible that both magnetospheric and shock models operate (for instance, the latter works for the most energetic bursts, while the former works for less energetic ones), but the current data of burst properties have not yet demanded an explanation involving dichotomy.

VI. SOURCE MODELS

In this section, I discuss various source models for FRBs. Since repeaters seem to be common and there is no proof that intrinsically one-off FRBs (those associated with cataclysmic events) exist [see Moroianu *et al.* (2022)], this entire section except for Sec. VI.G discusses sources for repeating FRBs. Unlike the previous theoretical review (Platts *et al.*, 2019), which lists models in a stamp-collecting manner,[20] I provide critical comments on these models. Sections VI.A–VI.C discuss the neutron star models, which are the most likely models. This is followed by other non-neutron-star astrophysical models (Sec. VI.D) and more exotic models

(Sec. VI.E) for repeating FRBs. Finally, cataclysmic models are discussed in Sec. VI.F.

A. Magnetars

The leading source model for FRBs is the magnetar model. Magnetars (Katz, 1982; Duncan and Thompson, 1992; Thompson and Duncan, 1995, 1996) may generally be defined as neutron stars with dipolar surface magnetic fields exceeding $\sim 10^{14}$ G, but there is no clear separation line between magnetars and high-B pulsars. Observationally they appear to be SGRs and anomalous x-ray pulsars (AXPs), which both have quiescent x-ray luminosities exceeding their spin-down luminosities, with the former displaying repeated soft γ-ray and hard x-ray bursts (Kaspi and Beloborodov, 2017). Later observations suggest that some neutron stars emit SGR-like bursts but have surface dipolar magnetic fields below 10^{14} G (Rea *et al.*, 2010). These sources may have strong multipolar magnetic fields near the surface and are also included in the magnetar population. There are 30 magnetars currently known,[21] including 16 SGRs and 14 AXPs. On another research front in transient astrophysics, a type of millisecond magnetar has been hypothesized (Usov, 1992) that powers GRBs and SLSNe (Zhang and Mészáros, 2001; Kasen and Bildsten, 2010; Woosley, 2010; Metzger *et al.*, 2011).

The connection between FRBs and magnetars has been discussed by many within different contexts. The earliest suggestion was by Popov and Postnov (2010), who interpreted the Lorimer burst (Lorimer *et al.*, 2007) as SGR hyperflares. Thornton *et al.* (2013) reported four additional FRBs, discussed several possibilities, and pointed out that the inferred FRB rate is consistent with the rate of SGR flares. The SGR-like model was further discussed by Kulkarni *et al.* (2014) and Katz (2016). Interactions between magnetar flares and an ambient wind were introduced by Lyubarsky (2014) as a mechanism to generate FRBs. Prompted by the discovery of the active repeater rFRB 20121102A that resides in a dwarf-star-forming galaxy similar to the hosts of long GRBs and SLSNe, Metzger, Berger, and Margalit (2017) suggested that millisecond magnetars could be the engine of active repeating FRBs. This model was further developed by Beloborodov (2017, 2020), Margalit and Metzger (2018), and Metzger, Margalit, and Sironi (2019) within the framework of the synchrotron maser model. Kumar, Lu, and Bhattacharya (2017) and Yang and Zhang (2018), on the other hand, considered the requirement of producing FRB emission from neutron star magnetospheres and drew the conclusion that the isolated neutron stars that can power FRBs are likely magnetars. Wadiasingh and Timokhin (2019) proposed that magnetars with a low twist of magnetic fields would initially not have enough pairs to screen $E_\parallel$ such that a pair cascade could be triggered to eventually power an FRB. Wadiasingh *et al.* (2020) discussed the line of death of FRB emission from magnetars and suggested that FRB emission is favored in magnetars with long periods. Lyubarsky (2020) proposed that enhanced magnetic reconnection in the current sheet region of a magnetar could power FRBs. Recent developments in

---

magnetar FRB models include the coherent inverse Compton scattering model (Zhang, 2022), the free-electron laser model (Lyutikov, 2021), and a direct emission model from a magnetized shock (Thompson, 2022). Prompted by the discovery of FRB 200428 associated with SGR J1935+2154 (Andersen *et al.*, 2020; Bochenek *et al.*, 2020), many studies have been carried out to investigate how the magnetar model could produce FRBs within the magnetosphere (Lu, Kumar, and Zhang, 2020; Yang *et al.*, 2020; Yang and Zhang, 2021) or in relativistic shocks (Margalit, Metzger, and Sironi, 2020; Yu *et al.*, 2021). The 0.286-s period of FRB 20191221A offers strong support to the magnetospheric magnetar models (Andersen *et al.*, 2022; Beniamini and Kumar, 2022), at least for this special source.

Various versions of the magnetar models have the following common ingredients:

- *Energy budget.*—These models make use of one of two energy reservoirs: either the rotation energy of the magnetar

$$E_r = \tfrac{1}{2}I\Omega^2 \simeq (2.0 \times 10^{46} \text{ erg})I_{45}P^{-2} \quad (147)$$

or the magnetic energy of the magnetar[22]

$$E_B \lesssim \tfrac{1}{6}B_s^2 R^3 \simeq (1.7 \times 10^{47} \text{ erg})B_{s,15}^2 R_6^3, \quad (148)$$

where I is the moment of inertia, P is the spin period, B_s is the surface dipolar magnetic field at the pole, and R is the radius of the neutron star. One can immediately see that the rotation energy reservoir becomes smaller than the magnetic energy reservoir when $P > (0.34 \text{ s})I_{45}^{1/2}B_{s,15}^{-1}R_6^{-3/2}$ is satisfied. The total energy of the bursts for repeating FRBs should be bound by these limits. For example, rFRB 20121102A emitted a total amount of energy $\sim 3.4 \times 10^{41}$ erg in the radio band, assuming isotropic emission from 1652 bursts detected in 59.5 h in a 47-d time span (D. Li *et al.*, 2021). Correcting the observational duty cycle, the total energy emitted would exceed $(6.4 \times 10^{45} \text{ erg})F_{b,-1}\eta_{r,-4}^{-1}$ assuming a radio efficiency $\eta_r \sim 10^{-4}$ and a global beaming factor $F_b = 0.1$. This is a substantial fraction of the magnetic energy available from a magnetar. The magnetar models involving a wide beaming angle and a low radiative efficiency (such as the synchrotron maser shock model) are greatly constrained by the data. Magnetospheric models invoke a smaller global beaming factor and a higher η_r, which are both favored (Zhang, 2020c).

- *Energy loss or dissipation rate.*—The average FRB emission luminosity should be bound by the average energy loss or dissipation rate of the magnetar. The energy loss rate due to magnetic dipole spin-down is

$$\dot{E}_r = \frac{B_s^2 R^6 \Omega^4}{6c^3} \simeq (10^{37} \text{ erg s}^{-1})B_{s,15}^2 P^{-4}R_6^6, \quad (149)$$

and the average energy dissipation rate of the magnetic energy can be estimated as

$$\dot{E}_B = \frac{E_B}{\tau_d} \simeq (3.2 \times 10^{35} \text{ erg s}^{-1})E_{B,47}\tau_{d,4}^{-1} \quad (150)$$

where $\tau_d = (10^4 \text{ yr})\tau_{d,4}$ is the characteristic decay time-scale of magnetic fields (Colpi, Geppert, and Page, 2000). Note that since FRB emission has a low duty cycle (even for highly active repeaters), the luminosities of individual bursts are not subject to these average energy loss or dissipation rate bounds as long as the average FRB energy emission rate is below this. For example, the active episode of rFRB 20121102A occurring in 2019 emitted on the order of 10^{41} erg energy in radio band in 47 d. Considering that the source may have an ~ 160-d period (Rajwade *et al.*, 2020) and that the source is not active in some of the projected cycles, one can roughly estimate the average radio-band energy emission rate as $\sim 10^{41} \text{ erg}/2 \text{ yr} \sim 1.6 \times 10^{33} \text{ erg s}^{-1}$. This is smaller than both $\dot{E}_r$ and $\dot{E}_B$. However, the requirement on η_r is tight, i.e.,

$$\eta_r > \begin{cases} (5 \times 10^{-3})E_{B,47}^{-1}\tau_{d,4}, & E_B \text{ budget,} \\ (1.6 \times 10^{-4})B_{s,15}^{-2}P^4R_6^{-6}, & E_r \text{ budget.} \end{cases} \quad (151)$$

Models with a low η_r are again disfavored unless E_B is much larger or τ_d is much shorter.[23]

- *Triggering mechanism.*—All magnetar FRB models, regardless of how the radio waves are emitted, rely on some common trigger mechanisms. One commonly discussed trigger mechanism is crust cracking at the neutron star surface (Thompson and Duncan, 2001; Beloborodov and Thompson, 2007; Wang *et al.*, 2018; Wadiasingh and Timokhin, 2019; Dehman *et al.*, 2020; Yang and Zhang, 2021), even though some have suggested that crust cracking may not proceed in an abrupt way (Levin and Lyutikov, 2012). Alternative trigger mechanisms include elastic deformation and magnetar oscillations without exceeding the yield strain of the crust (Wadiasingh and Chirenti, 2020) or fast ambipolar diffusion in the core (Beloborodov, 2017). In any case, oscillations of the crust would send Alfvén waves to the magnetosphere, triggering various processes that might be related to FRB production [such as bunched curvature radiation (Kumar, Lu, and Bhattacharya, 2017; Yang and Zhang, 2018; Cooper and Wijers, 2021) or inverse Compton scattering (Zhang, 2022), direct electromagnetic wave generation due to nonuniform pair production (Philippov, Timokhin, and

---

[22]This estimate includes the dipolar magnetic field only. Magnetars may store a toroidal magnetic field component that may be stronger than the poloidal component. Thus, this estimate is a lower limit.

[23]Beloborodov (2017) and Margalit, Berger, and Metzger (2019) argued that magnetars different from the Milky Way known population with a larger core magnetic field and a shorter magnetic decay timescale may exit in other galaxies to power active repeaters.

Spitkovsky, 2020; Yang and Zhang, 2021), enhanced reconnection in the current sheet region outside the magnetosphere (Lyubarsky, 2020), and ejection of magnetic pulses outside the magnetosphere to produce FRBs via magnetized relativistic shocks (Yuan *et al.*, 2020)]. Alternative trigger mechanisms include sudden magnetic reconnection events in the magnetosphere (Popov and Postnov, 2010), sudden discharge of vacuum gaps (Katz, 2017a), or sudden triggers from an external event (Zhang, 2017; Dai, 2020).

The proposed magnetar models also differ in several aspects:

- *Emission site.*—From small to large distance from the neutron star surface, there are four versions of magnetar models: (1) models invoking the FRB emission region inside the magnetosphere, typically tens to hundreds of neutron star radii (Kumar, Lu, and Bhattacharya, 2017; Yang and Zhang, 2018, 2021; Wadiasingh and Timokhin, 2019; Kumar and Bošnjak, 2020; Lu, Kumar, and Zhang, 2020; Lyutikov, 2021; Zhang, 2022), (2) models invoking the current sheet region outside the light cylinder as the FRB emission site (Lyubarsky, 2020; Mahlmann *et al.*, 2022), (3) models invoking internal shocks due to collisions between magnetic blobs (Beloborodov, 2017, 2020), and (4) models invoking external shocks[24] formed when magnetic shells are decelerated by the magnetar wind (Metzger, Margalit, and Sironi, 2019; Margalit, Metzger, and Sironi, 2020; Thompson, 2022).

- *Radiation mechanism.*—Many mechanisms discussed in Sec. V have been proposed for various versions of the magnetar models. The magnetospheric models invoke bunched curvature radiation (Kumar, Lu, and Bhattacharya, 2017; Yang and Zhang, 2018; Lu, Kumar, and Zhang, 2020; Cooper and Wijers, 2021), bunched inverse Compton scattering (Zhang, 2022), free-electron laser (Lyutikov, 2021), or direct EM generation due to nonuniform pair production (Philippov, Timokhin, and Spitkovsky, 2020; Yang and Zhang, 2021) as radiation mechanisms. In the current sheet region, magnetosonic waves excited by coalescence of magnetic islands (Lyubarsky, 2020) or coherent inverse Compton scattering (Zhang, 2022) are invoked to produce FRB emission. In both the magnetic internal and external shock regions, the specific version of the synchrotron maser (bunched coherent cyclotron or synchrotron radiation) mechanism is invoked to produce FRB emission (Plotnikov and Sironi, 2019; Sironi *et al.*, 2021).

There are many open questions regarding the magnetar models for FRBs. Besides the previously discussed question regarding the trigger mechanism, emission site, and radiation mechanism, the following are some other examples of open questions:

- *Can magnetars produce all FRBs in the Universe?*— Shortly after the discovery of FRB 200428 in association with the Galactic magnetar SGR 1935+2154, the enthusiasm and confidence of interpreting all FRBs in the Universe as being generated by magnetars have grown tremendously (Lu, Kumar, and Zhang, 2020; Margalit *et al.*, 2020). The assumption is that all FRBs are intrinsic repeaters. Regular magnetars such as those observed in the Milky Way may be responsible for the apparently nonrepeating FRBs and those repeaters with a low repetition rate, while young magnetars may be responsible for active repeaters observed in cosmological distances. The fact that there are no active repeating FRB sources from the Milky Way is interpreted as the lack of young magnetars in the Galaxy (or if there is any, the FRB emission beam does not point toward Earth). The repeaters in association with the old population such as globular clusters (Kirsten *et al.*, 2022; Nimmo *et al.*, 2022) were interpreted as a new population of young magnetars born from accretion-induced collapse or mergers of binary neutron stars (Margalit, Berger, and Metzger, 2019; F. Y. Wang *et al.*, 2020), binary white dwarfs (WDs) (Kremer, Piro, and Li, 2021), or NS-WD binaries (Zhong and Dai, 2020). However, growing evidence suggests that this most conservative "magnetars make them all" suggestion for the FRB origin may not be adequate to account for all the FRB observational data. For example, the rFRB 20200120E–like sources may be common. However, none of the known Galactic magnetars are associated with globular clusters. The magnetars make them all scenario likely runs into the event rate issue. The general delay with respect to the star-formation rate required for the inferred FRB redshift distribution (Hashimoto *et al.*, 2022; Qiang, Li, and Wei, 2022; Zhang and Zhang, 2022) also raises a flag to this simple scenario.

- *Does FRB emission favor young or old magnetars?*— Active repeaters are widely interpreted as being produced by newborn magnetars. The arguments in support of this idea include the association of a dwarf-star-forming galaxy (Tendulkar *et al.*, 2017) with rFRB 20121102A, the associations of a persistent radio source with rFRB 20121102A (Chatterjee *et al.*, 2017; Marcote *et al.*, 2017) and rFRB 20190520B (C. H. Niu *et al.*, 2022), as well as a larger energy reservoir (both magnetic and spin energies) and probably a faster decaying rate (Beloborodov, 2017; Metzger, Berger, and Margalit, 2017) in young magnetars. The issues with having young magnetars as prolific FRB emitters include significant free-free absorption and induced Compton scattering in a dense environment associated with supernova remnants or pulsar wind nebulae around the newborn magnetars. On the other hand, charge starvation seems to be favorable for magnetars to make FRBs within their magnetospheres. Older magnetars tend to more easily reach charge starvation because of the reduced pair production due to slow spin and low twist (Wadiasingh and Timokhin, 2019; Beniamini, Wadiasingh, and Metzger, 2020; Wadiasingh *et al.*, 2020).

- *What is the mechanism for $E_\parallel$ in magnetar magnetospheres?*—A charge starved region in a magnetar magnetosphere is where $E_\parallel$ is developed and particles are

---

[24]Under certain conditions, the emission radius of the model of Metzger, Margalit, and Sironi (2019) can be smaller than that of the internal shock model (Beloborodov, 2020).

accelerated. Magnetospheric FRB models require the existence of an $E_\parallel$ to continuously supply energy to otherwise rapidly cooling particle bunches (Kumar, Lu, and Bhattacharya, 2017; Zhang, 2022). The exact mechanism to generate $E_\parallel$ in the FRB emission region is not identified. One possibility is that $E_\parallel$ can be developed as Alfvén waves propagate to the outer magnetosphere, where the $e^\pm$ density is not sufficient to supply the current required to sustain the Alfvén waves (Kumar and Bošnjak, 2020). Another mechanism is the traditional pulsar mechanism that opens various types of gaps in the pulsar magnetosphere (Ruderman and Sutherland, 1975; Arons and Scharlemann, 1979; Cheng, Ho, and Ruderman, 1986; Zhang et al., 1997; Harding and Muslimov, 1998; Muslimov and Harding, 2004). The energetics of these gaps, on the other hand, are limited by the spin-down power of the magnetars, which is not large enough to power FRBs for slow rotators. Sudden crust cracking may excite global readjustment of the magnetospheric configuration, leading to temporarily enhanced gaps with large $E_\parallel$, which could be another mechanism to power FRBs.

- *What is the role of Alfvén waves?*—Various FRB models invoke Alfvén waves as an important ingredient. The role of Alfvén waves varies in different models. Kumar and Bošnjak (2020) and Lu, Kumar, and Zhang (2020) invoked Alfvén waves as the agent to produce $E_\parallel$ at a large enough radius to accelerate bunched particles to power FRB emission. A. Y. Chen et al. (2022) questioned this possibility by a numerical simulation that shows that particles are advected without forming a significant charge starved region. Kumar, Gill, and Lu (2022) performed simulations for a longer duration and found that an $E_\parallel$ of the order of a few percent of the Alfvén wave amplitude can indeed be generated. Yuan et al. (2020) showed that low-amplitude Alfvén waves from a magnetar quake propagate to the outer magnetosphere and convert to "plasmoids" (closed magnetic loops). The plasmoids are accelerated from the star, driving blast waves into the magnetar wind. Lyubarsky (2020) invoked Alfvén waves to significantly compress the current sheet region outside the light cylinder to enhance relativistic magnetic reconnection, which may facilitate the generation of FRBs in the reconnection region (Lyubarsky, 2020; Mahlmann et al., 2022; Zhang, 2022).

B. Other isolated neutron star models

Besides magnetars, the following other types of isolated neutron stars have been discussed as the source of FRBs:

- *Giant pulses from young pulsars.*—Giant radio pulses have been observed with certain young pulsars, such as the Crab pulsar. The brightest giant pulse (GP) observed thus far has a peak amplitude $S_{\nu,\max} = 2.2$ MJy at 1 GHz and a pulse width < 0.4 ns, corresponding to a brightness temperature $T_b \gtrsim 10^{41.3}$ K (thanks to its short duration) (Hankins and Eilek, 2007). An immediate inference is that similar GPs from nearby galaxies would be detected as FRB-like events by observers on Earth

(Connor, Sievers, and Pen, 2016; Cordes and Wasserman, 2016). Unlike magnetar-powered FRBs that possibly consume magnetic energy of the parent star, these GP-like FRBs likely consume the spin energy of the parent star. Placing GP-emitting pulsars at larger distances suggests that they could be detected up to $\sim$100 Mpc but not at larger cosmological distances, as suggested by the DM excess of most FRBs. Therefore, FRBs in these models are also called extragalactic radio bursts (Cordes and Wasserman, 2016). It has been confirmed that most FRBs originate from cosmological distances greater than 100 Mpc (Tendulkar et al., 2017; Macquart et al., 2020; Bhandari and Flynn, 2021). The simplest version of this model is incapable of interpreting the data unless much brighter GPs are invoked.

- *Pulsar lightening.*—Katz (2017a) argued that the FRB phenomonology is similar to atmosphere lightening and conjectured that FRBs are produced when vacuum gaps in pulsar magnetospheres break down to suddenly drive currents in the magnetosphere. The FRB energetics in this model is also limited by spin-down power of the underlying pulsar.

C. Interacting neutron star models

A number of FRB models invoke neutron stars interacting with an external agent. These interacting neutron star models come in different flavors depending on the energy budget that is invoked to explain FRB emission. In the extreme versions of the interaction models, the ultimate energy comes externally from the gravitational energy of a falling object or the kinetic energy of an external moving fluid. In milder versions of the models, the ultimate energy still comes from the neutron star itself (for instance, the spin or magnetic energy), but the external agent may play the role of triggering FRB emission or shaping the detectability of FRBs. I now discuss several such models from the literature.

- *Comet-asteroid interaction models.*—One suggested way of making FRBs is through interactions between comets or asteroids and a neutron star. The direct impact model (Geng and Huang, 2015; Dai et al., 2016; Bagchi, 2017; Smallwood, Martin, and Zhang, 2019; Dai, 2020; Dai and Zhong, 2020) invokes a gravitational energy budget,

$$E_g = \frac{GMm}{R} \simeq (1.9 \times 10^{40} \text{ erg})$$
$$\times \left(\frac{M}{1.4M_\odot}\right)\left(\frac{m}{10^{20} \text{ g}}\right) R_6^{-1}, \quad (152)$$

to power FRBs, where M and R are the mass and radius of the neutron star and m is the mass of the small body. One can see that the Galactic FRB 20200428 from SGR 1935+2154, which has a radio luminosity and energy smaller by orders of magnitude than cosmological FRBs, already requires a small body mass[25] $m \sim 10^{20}$ g.

---

[25]Beaming correction is usually not considered in these models, because the emission solid angle is expected to be large.

Scaling the required mass up based on the luminosities to cosmological FRBs, one finds that the demanded comet-asteroid mass is immense. For example, take the 2019 active episode of rFRB 20121102A (D. Li *et al.*, 2021). The total radio energy emitted in 1652 bursts detected in 59.5 h over 47 d is $\sim 3.4 \times 10^{41}$ erg. Counting on the missed FRBs outside of the FAST observing window, the total radio energy would be $\sim 6.4 \times 10^{42}$ erg. Recall that the Galactic FRB 20200428 has a radio energy of a few 10^{35} erg (Andersen *et al.*, 2020, Bochenek *et al.*, 2020). The total small body mass to power the rFRB 20121102A for that emission episode is already a few times 10^{27} g, which is of the order of Earth's mass. Thus, the comet-asteroid collision model is an expensive mechanism that consumes substantial mass. The total mass in the Kuiper belt of the Solar System is about 2% of Earth's mass (Pitjeva and Pitjev, 2018). Furthermore, a significant fraction of comets and asteroids are dynamically ejected when a neutron star enters the comet-asteroid belt (Smallwood, Martin, and Zhang, 2019). The large mass budget and short waiting times (as short as several miliseconds) between some bursts (D. Li *et al.*, 2021; Xu *et al.*, 2022; Zhang *et al.*, 2022) essentially rule out the direct impact model at least for rFRB 20121102A.

Another version of the comet-asteroid interaction model does not invoke direct impact. Mottez and Zarka (2014) suggested that small bodies orbiting a pulsar at low orbits could periodically interact with the pulsar winds to drive two stationary Alfvénic structures called Alfvén wings. The destablization of the plasma by the Alfvén wing's current may excite coherent radiation and make FRBs. Mottez and Zarka (2014) estimated that a multijansky level radio burst could be generated if the source is at a distance of $D = 1$ Mpc and if the small body is $r = 1$ A.U. from the pulsar (the flux depends on r^{-2}). Interpreting cosmological FRBs within this model requires narrow beaming and low orbits. In general this model is energetically much more efficient than the direct impact models since it does not require the small body to be destroyed. Nonetheless, since the ultimate emission power comes from the spin energy of the pulsar, the same energy requirements for single neutron stars also applies to this model. Observationally it may be difficult to distinguish this model from certain isolated neutron star models.

- *Cosmic comb model*.—Zhang (2017) suggested that a sudden interaction between a fluid flow (also called an astronomical stream) and a nearby source of an otherwise isolated neutron star can result in coherent radio emission. An FRB is seen by an observer on Earth when the combed magnetosphere sweeps across the line of sight. The sources of the stream could be energetic events such as supernovae, gamma-ray bursts, and tidal disruption events, or more moderate events such as AGN flares or even erratic outflows from a companion. As a result, an FRB may or may not be associated with bright counterparts, depending on the source of the astronomical stream. Note that the specific version of

this model invoking interaction between a supernova and a neutron star was proposed earlier (Egorov and Postnov, 2009) and was overlooked by Zhang (2017). rFRB 20121102A was interpreted as a repeatedly combed regular neutron star near a massive black hole (Zhang, 2018b). The ultimate energy power of this model comes from the kinetic energy of the astronomical stream. The kinetic luminosity received by the neutron star can be estimated as

$$L_{\rm kin} \sim \frac{L}{4\pi r^2} \pi \left(\frac{cP}{2\pi}\right)^2, \qquad (153)$$

where L is the luminosity of the source of the astronomical stream, r is the distance of the neutron star from that source, and P is the spin period of the neutron star ($cP/2\pi$ is the light cylinder radius). The condition for a cosmic comb event to happen is that the ram pressure must exceed the magnetic pressure at the light cylinder, i.e.,

$$\rho v^2 > \frac{B_s^2}{8\pi} \left(\frac{2\pi R}{cP}\right)^6, \qquad (154)$$

where ρ and v are the density and velocity of the stream at the interaction radius and B_s and R are the surface magnetic field and radius of the neutron star, respectively.

The 16-d period of rFRB 20180916B (Amiri *et al.*, 2020) can be interpreted as the orbital period of a binary system containing an FRB pulsar (or magnetar) and a massive star or neutron star companion (Ioka and Zhang, 2020; Lyutikov, Barkov, and Giannios, 2020). For a total mass $M_{\rm tot} = 10 M_\odot$ in the binary, the separation between the two stars is $\sim 4 \times 10^{12}$ cm. The kinetic luminosity received by the FRB pulsar is $L_k = (3.6 \times 10^{32} \text{ erg s}^{-1}) L_{39} P^2$, where $L = (10^{39} \text{ erg s}^{-1}) L_{39}$ is the companion's kinetic luminosity normalized to its Eddington luminosity. Such a luminosity is too small to interpret the repeated FRBs from rFRB 20180916B unless an extremely narrow beam or a much greater luminosity than the Eddington value are assumed. As a result, the original version of the cosmic comb model is not adequate to interpret the observations of at least rFRB 20180916B.

- *Binary comb models*.—Ioka and Zhang (2020) proposed the binary comb model for periodically repeating FRBs. The role of the companion is no longer to directly provide the power of FRBs. Rather, the interaction between the companion wind and the FRB pulsar magnetosphere defines a funnel from which FRBs, intrinsically produced by the FRB pulsar itself, can escape and be detected from Earth. The similar scenario was independently proposed by Lyutikov, Barkov, and Giannios (2020), who also displayed the companion-wind-defined funnels through numerical simulations. Wada, Ioka, and Zhang (2021) expanded on the funnel mode of Ioka and Zhang (2020) and identified two more modes (the τ-crossing mode and inverse funnel mode) to

define the FRB escaping window for periodic FRBs. Even though within the binary comb model the companion wind plays only a passive role of defining the detectability of the bursts, it was nonetheless speculated (Ioka and Zhang, 2020) that the so-called aurora particles entering the magnetosphere of the FRB pulsar may play an active role in driving coherent radio emission and powering FRBs.

- *Magnetospheric interaction models*.—It is possible that direct interactions between the magnetospheres of two neutron stars may make FRBs. Possible FRB-like electromagnetic field signals have been discussed in the context of binary neutron star mergers shortly before the merger (Hansen and Lyutikov, 2001; Lai, 2012; Piro, 2012; Wada, Shibata, and Ioka, 2020; Wang *et al.*, 2016). The commonly discussed energy release mechanism is the unipolar effect as a neutron star with a weak magnetic field travels in the magnetosphere of another neutron star with a stronger magnetic field. Gourgouliatos and Lynden-Bell (2019) studied several configurations between the two magnetospheres of two neutron stars in the premerger phase and discussed possible energy dissipation. They mentioned the possibility of connecting these interactions with repeating FRBs. Zhang (2020b) showed that for typical parameters similar to the double pulsar system (Kramer and Stairs, 2008) strong magnetosphere interactions between two inspiring neutron stars occur decades to centuries before the merger. Zhang (2020b) argued that such systems could be ideal candidates for producing repeating FRBs through magnetic reconnection with the expense of the magnetic energy (and ultimately the spin energy) of the two neutron stars. Invoking the beaming effect (which is expected from magnetospheric-interaction-induced events), Zhang (2020b) argued that the energy budget in the system is more than enough to power rFRB 20121102A–like active repeaters. The model has several predictions (Zhang, 2020b): (1) The activity level elevates with time as the two neutron stars get closer with time. (2) Active repeaters could be megahertz gravitational wave sources detectable by future spaceborne GW observatories such as LISA (Amaro-Seoane *et al.*, 2017), Taiji (Ruan *et al.*, 2018), and TianQin (Luo *et al.*, 2016). (3) There could be quasiperiodic signals at the orbital period, which is typically hundreds of seconds. The environment of the globular cluster rFRB 20200120E (Kirsten *et al.*, 2022; Nimmo *et al.*, 2022) is consistent with that of a binary neutron star merger, even though models invoking binary neutron stars (BNSs) require the source to have a much longer duration, for instance, 10^6 yr (Kremer, Piro, and Li, 2021; Lu, Beniamini, and Kumar, 2022).

- *White-dwarf-fed neutron star model*.—Gu *et al.* (2016) and Gu, Yi, and Liu (2020) delineated a scenario that invokes a compact NS-WD binary in which the WD already fills its Roche lobe such that matter from the WD can be channeled toward the NS. They speculated that magnetic reconnection may be triggered by episodic accretion of WD materials approaching the NS surface. Curvature radiation is then envisaged to happen as

relativistic particles stream out along the magnetic field lines. Such a scenario is speculative since known neutron star accreting systems (such as x-ray pulsars) tend to produce thermal emission in the accretion column. In general it is difficult to produce delicate magnetospheric coherent radio emission in an accreting system.

D. Non-neutron-star astrophysical models

- *Stellar-mass black hole sources*.—Besides neutron stars, the only other kind of objects whose sizes are small enough to accommodate millisecond durations of FRBs are stellar-mass black holes. The difference between a black hole engine and a neutron star (for instance, a magnetar) engine is that the former may or may not have as clean a magnetosphere as the latter because of the dirty accretion environment, so the magnetospheric radiation mechanisms associated with neutron star models may not be straightforwardly applied. Nonetheless, Katz (2017b, 2022a) speculated that the accretion disk of a black hole could collimate a "funnel" from which jetlike emission could be released. To account for the short duration of the FRBs, Katz (2020a) speculated that the jet may be rapidly wandering and that the duration of the FRB corresponds to the duration when the narrow FRB jet sweeps across the line of sight. Katz (2020a) further argued that the lack of periodicity in repeating FRBs at the typical neutron star spin period favors the black hole origin of FRBs; see Sec. IV.C for counterarguments. Katz did not specify the FRB emission site and the coherent radiation mechanism. L.-B. Li *et al.* (2018) suggested that the accretion system involving a black hole and a white dwarf with Roche lobe overflow could launch magnetic blobs and produce FRBs via the synchrotron maser mechanism. Sridhar, Metzger *et al.* (2021) proposed a detailed model for periodic FRBs invoking an accreting black hole binary similar to the black hole (BH) ultraluminous x-ray (ULX) sources. The FRB mechanism is hypothesized as the synchrotron maser mechanism in relativistic, magnetized shocks similar to GRB-like models for magnetars. Such a model makes some specific predictions (for instance, some known ULX sources will someday produce FRBs). Since these models rely on the synchrotron maser models as the radiation mechanism, the general theoretical and observational caveats discussed in Sec. V.C also apply to these models.

- *Supermassive black hole (SMBH) sources*.—The supermassive black holes in the center of galaxies or AGNs have a characteristic timescale, i.e., $r_s/c \sim (10^3 \text{ s})(M/10^8 M_\odot)$ (where $r_s = 2GM/c^2$ is the Schwarzschild radius of a black hole with mass M), that is much longer than milliseconds. Therefore, it is not straightforward to invoke a SMBH to power FRBs unless emission is confined in a region much smaller than the event horizon. Nonetheless, some suggestions have indirectly made use of SMBHs to power FRBs. Romero, del Valle, and Vieyro (2016) and Vieyro *et al.* (2017) proposed that FRBs could be produced through interactions between a relativistic electron beam from an

AGN jet and a turbulent plasma. The emitters (called cavitons) have a much smaller scale than the SMBH so that they can make millisecond-duration bursts. In this model, coherent radio emission is produced through Langmuir-wave-driven intense electrostatic soliton emission, which can be broadly defined as one of the "bunching" mechanisms discussed in Sec. V. Within the framework of the cosmic comb model Zhang (2017, 2018b) invoked the episodic wind from a SMBH interacting with a neutron star to interpret the large RM and persistent radio emission associated with rFRB 20121102A. Gupta and Saini (2018) applied a similar scenario to make episodic AGN winds to interact with a Kerr stellar-mass black hole to launch episodic jets that power FRBs. Wada, Ioka, and Zhang (2021) studied rFRB 20121102A within the framework of the binary comb model and constrained the allowed parameters of the companion of the FRB pulsar. They found that a SMBH could be a plausible companion of this FRB source. The host galaxy data of localized FRBs already rule out AGNs or galactic centers as the sources of the majority of FRBs. As a result, models attempting to interpret the bulk FRB population invoking AGNs or galactic centers are ruled out. Nonetheless, invoking AGNs or galactic centers for individual FRB sources within the scope of broader models (such as binary combs) remains possible.

- *Stellar flares.*—For a short period of time flares from Galactic stars were considered as the sources of at least some FRBs (Loeb, Shvartzvald, and Maoz, 2014). The suggestion faced the issue of the free-free absorption constraint (Luan and Goldreich, 2014) and the duration limit ($R/c \gg 1$ ms for stars). The localization of rFRB 20121102A in a distant galaxy (Chatterjee *et al.*, 2017; Marcote *et al.*, 2017; Tendulkar *et al.*, 2017) quickly disqualified this model and any model invoking origins inside the Galaxy.

E. Exotic repeater models

Many FRB models have invoked hypothetical objects or phenomena to interpret FRBs, which I summarize in this section. The confirmation of the existence of any of these objects or phenomena would have profound implications for astrophysics and physics in general. However, since some of the aforementioned models (such as magnetars and isolated or interacting neutron stars) have provided reasonable interpretations to most of the FRB phenomenology, I regard these models as exotic. Instead of critically commenting on the validity of each model, I simply list them now. Our only comment on all of these models is the well-known quotation from Carl Sagan, "Extraordinary claims require extraordinary evidence."

- *Strange quark stars.*—Strange quark stars are hypothetical compact stars made up of three flavor (u, d, s) quarks (Alcock, Farhi, and Olinto, 1986). Ouyed, Leahy, and Koning (2020, 2021) suggested that conversion from neutron stars to quark stars would make quark novae that can account for an array of astrophysical transients such as GRBs and FRBs. In particular, FRBs are produced when the quark nova ejecta chunks collide with the ambient medium. Strange stars may have a thin normal-matter crust (Alcock, Farhi, and Olinto, 1986). Episodic-accretion-induced collapses of the crust have also been suggested to power repeating FRBs (Zhang, Geng, and Huang, 2018; Geng, Li, and Huang, 2021).

- *Primordial black holes.*—Primordial black holes (PBHs) are hypothetical black holes formed shortly after the big bang that can carry a wide mass distribution not subject to stellar evolution, including masses much smaller than $M_\odot$. Abramowicz, Bejger, and Wielgus (2018) proposed a PBH-NS interaction model for repeating FRBs. After a PBH enters the center of a NS, the NS will be accreted and eventually swallowed by the PBH. During the process, the NS magnetosphere is continuously reconfigured, making repeating FRBs.

- *Superconducting cosmic strings.*—Cosmic strings are hypothetical stringlike topological structures in the Universe that are the macroscopic manifestation of string solutions in field theories. Like elastic, current-carrying wires, cosmic strings are envisaged to carry energy, to be dynamically evolving, and to be superconducting. Vachaspati (2008) suggested that oscillations at the "cusps" (points on an idealized string that reach speed of light for an instant) would radiate FRB-like emission. Other suggestions include collisions of string structures [cusps and kinks (Cai, Sabancilar, and Vachaspati, 2012; Cai *et al.*, 2012; Ye, Wang, and Cai, 2017)], interactions with a current-carrying loop in the local magnetic field (Yu *et al.*, 2014), and decay of string cusps (Brandenberger, Cyr, and Varna Iyer, 2017).

- *Axion stars, axion clumps, and axion quark nuggets.*— The axion is a hypothetical elementary particle and a promising candidate for cold dark matter in the Universe. If axions exist, it is hypothesized that they can form gravitationally bound axion clumps or axion stars (typically with a mass of $\sim 10^{-12} M_\odot$). It has been suggested that FRBs could be generated when axion stars collide with neutron stars or black hole accretion disks (Iwazaki, 2015, 2021). Other ideas include the induced collapse of axion clumps ("miniclusters") by the strong magnetic field of a compact star (Tkachev, 2015), a black hole laser powered by axion superradient instabilities (Rosa and Kephart, 2018), and even magnetic reconnection in a neutron star magnetosphere triggered by the falling of "axion quark nuggets" (Van Waerbeke and Zhitnitsky, 2019).

- *Macroscopic dipole collisions.*—Thompson (2017a, 2017b) conjectured that macroscopic, superconducting magnetic dipoles might have formed around the time of cosmic electroweak symmetry breaking. The collisions of these large superconducting dipoles (LSDs) may make small explosions to power FRBs. The collisions more preferably happen near massive black holes where LSDs have higher densities. Both repeaters and non-repeaters can be produced with this mechanism.

- *Dicke superradiance.*—In quantum optics, Dicke super-radiance (DSR) (Dicke, 1954) is a phenomenon that occurs when a group of excited (population inverted) atoms or molecules interact with a triggering event (such

as a light) to radiate coherently. The phenomenon was well tested in the laboratory (Skribanowitz *et al.*, 1973). Houde, Mathews, and Rajabi (2018) hypothesized that DSR can occur on the Galactic scale involving $\sim 10^{30}$–10^{32} entangled molecules over distances spanning 100–1000 A.U., which can power FRBs. Houde *et al.* (2019) further suggested that a pulsar located from ~ 100 pc away from the entangled molecules could serve as the trigger for DSR.

- *Alien technology.*—Lingam and Loeb (2017) speculated that FRBs could be artificial beam-powered light sails of extragalactic aliens. Zhang (2020a) suggested that observed FRBs are of astronomical origins, but communicative extraterrestrial intelligence (CETI) in the Milky Way Galaxy may choose to emit FRB-like signals if it wants to broadcast its existence. The nondetection of any artificial FRB-like signals from the Galaxy in a decade with all-sky radio monitors may place a meaningful upper limit on the average emission rate of such signals by CETI in the Galaxy. To produce a 1-ms Jy signal on Earth, the required emission power for aliens at a typical distance of 10 kpc is $\sim (10^{22} \text{ W}) f_{b,-3} (d/10 \text{ kpc})^2$, where $f_b \sim 10^{-3}$ is the beaming angle.

F. Cataclysmic progenitor models

Even though the majority of detected FRBs are not observed to repeat, the cataclysmic progenitor models for FRBs are not taken as seriously as repeater models. The main arguments against these ideas to become the mainstream FRB models include the following: (1) Since the energy budget of FRBs is much smaller than the energy available in cataclysmic events and since repeaters have been detected, it is essentially impossible to prove that the apparently one-off FRBs will never repeat. (2) The FRB event rate density is much greater than the rate densities of all known cataclysmic events (Ravi, 2019). The most common cataclysmic events in the Universe is core-collapse supernovae with $R_{\rm CC} \sim 10^5 \text{ Gpc}^{-3} \text{ yr}^{-1}$, whereas the FRB event rate density above $10^{37} \text{ erg s}^{-1}$ is a few $R_{\rm FRB}(L > 10^{37} \text{ erg s}^{-1}) \sim 10^7$–$10^8 \text{ Gpc}^{-3} \text{ yr}^{-1}$ (Lu, Kumar, and Zhang, 2020). If any cataclysmic channels are relevant, they must account for only a small fraction of FRBs, perhaps above a particular luminosity [where the rate density becomes smaller, for instance, $R_{\rm FRB}(L > 10^{42} \text{ erg s}^{-1}) \sim 3.5 \times 10^4 \text{ Gpc}^{-3} \text{ yr}^{-1}$ (Luo *et al.*, 2020)], or spread out in a wider luminosity range but with negligible contribution to the observed event rate density.

Nonetheless, some cataclysmic models are quite attractive, since these events are destined to produce brief electromagnetic radiation signals, whether or not they are FRBs. Two leading models include the blitzar scenario invoking implosion of supramassive neutron stars (SMNSs) and various CBC models invoking mergers of NSs and BHs. I now highlight these models.

- *Blitzars.*—SMNSs are spin-supported massive neutron stars whose nonspinning mass already exceeds the maximum NS mass allowed by the NS equation of state. The existence of an SMNS is therefore temporary. The

NS will inevitably collapse to a BH as it is spun down via magnetic dipolar radiation or even gravitational wave radiation. As the bulk of the NS enters the horizon during its collapse to a BH, the closed magnetic field lines would detach from the star and get ejected (the open field lines penetrating the hole may stay longer). Falcke and Rezzolla (2014) suggested that such a magnetosphere ejection process would power an FRB and termed the phenomena blitzars. The process was numerically simulated (Most, Nathanail, and Rezzolla, 2018), and a millisecond-duration episode of significant Poynting flux injection was indeed observed, suggesting the robustness of the mechanism. Falcke and Rezzolla (2014) envisaged that a significant amount of SMNSs could be produced from a few percent of core-collapse supernovae. Assuming that these SMNSs do not carry a strong magnetic field, they suggested that collapse happens thousands to a million years after the birth of the SMNSs, so no bright counterpart is expected in association with FRBs. Zhang (2014) pointed out that the so-called internal x-ray plateaus observed in both long and short GRBs are best interpreted as the collapse of SMNSs born during the GRB events. Zhang (2014) therefore suggested that FRBs should be produced hundreds to thousands of seconds after some GRBs if the blitzar mechanism is valid. One concern is whether the produced FRB can escape the messy environment near a GRB. Zhang (2014) also suggested that this is not a concern, since the relativistic GRB jet has cleared a funnel to facilitate the propagation of the FRB. Since internal plateaus are more commonly observed following short GRBs (Rowlinson *et al.*, 2010,2013; Lü *et al.*, 2015), Zhang (2014) noted that there could be interesting triple associations among FRBs, short GRBs, and gravitational waves. Follow-up radio observations to search FRB-like events have been carried out for some FRBs (Bannister *et al.*, 2012; Palaniswamy *et al.*, 2014; Rowlinson and Anderson, 2019; Bouwhuis *et al.*, 2020), even though no confirmed association has been reported [see Bannister *et al.* (2012) for two untriggered events whose occurring epochs are consistent with the suggested epoch of Zhang (2014)]. An interesting association between a nonrepeating FRB 20190425A and a BNS merger gravitational wave event GW190425 was claimed by Moroianu *et al.* (2022) with a chance coincidence of $\sim 1.9 \times 10^{-4}$. The FRB is delayed by 2.5 h from the GW event. This association, if it is indeed physical, is consistent with the suggested scenario of Zhang (2014). The potential host galaxy of FRB 20190425A is also found to be consistent with that of a BNS merger (Panther *et al.*, 2023).

- *NS-NS mergers.*—There are many suggested associations between one-off FRBs and NS-NS mergers. Most of these suggested processes occur right before the merger. Hansen and Lyutikov (2001) considered possible electromagnetic precursor emission before the merger caused by magnetospheric interactions between the two NSs and estimated the x-ray and radio luminosities. Lai (2012) and Piro (2012) studied the premerger magnetospheric interaction processes using the unipolar inductor

model and estimated a brief EM signal with luminosity up to 10^{46} erg s^{-1} within 1 s of the merger. Totani (2013) suggested that an FRB may be made right before the merger as the magnetospheres of the two merged NSs synchronize to orbital motion. The unipolar inductor model was specifically applied to interpret FRBs by Wang *et al.* (2016), who showed that many of the observed FRB properties could be reproduced within this model. Sridhar, Zrake *et al.* (2021) proposed a premerger FRB model specifically invoking the synchrotron maser model. Cooper *et al.* (2022) discussed a merger-induced pulsar magnetospheric emission mechanism to produce a one-off FRB before a NS-NS merger. The general charged compact binary coalescence (cCBC) model (Zhang, 2016; Zhang, 2019) (which is discussed later) also applies to NS-NS mergers since NSs are generally charged, even though its signal may be outshone by some of the other previously discussed signals. One common issue for all the premerger NS-NS models for FRBs is that the neutron-rich ejecta launched due to tidal effect would make the environment "dirty" such that the FRB emission can escape only in a small solid angle. This further reduces the detection rate of these events, making NS-NS mergers incapable to interpret the majority of FRBs.

The postmerger blitzar scenario (Zhang, 2014) gives another possibility for NS-NS merger association with one-off FRBs. Short GRB observations and theoretical modeling suggest that the collapse of the postmerger SMSN happen 100 to 10^4 s after the merger (Lasky *et al.*, 2014; Ravi and Lasky, 2014; Lü *et al.*, 2015; Gao, Zhang, and Lü, 2016). This provides a time window of interest for the search of FRBs associated with NS-NS mergers. The GW190425–FRB 20190425A association with a 2.5-h time difference is consistent with this scenario (Moroianu *et al.*, 2022).

Finally, if a NS-NS merger leaves a stable massive magnetar behind, the standard magnetar mechanism may operate to power repeating FRBs (Yamasaki, Totani, and Kiuchi, 2018; Margalit, Berger, and Metzger, 2019; F. Y. Wang *et al.*, 2020).

- *WD-WD mergers.*—Even though the size of a white dwarf is too large to accommodate the millisecond duration of FRBs, Kashiyama, Ioka, and Mészáros (2013) proposed that mergers of two white dwarfs would lead to synchronization of the magnetic fields and produce millisecond radio bursts from the polar region of a postmerger magnetized white dwarf. This model predicts type Ia supernova–FRB associations, which have never been observed.

- *NS-BH mergers.*—For CBCs, if at least one of the members is charged, one gets a Poynting flux with luminosity rising sharply toward merger (Zhang, 2019). Such cCBCs would naturally give rise to an FRB-like signal in association with the merger (with the FRB observationally delayed due to the plasma dispersion). Since spinning NSs (and all spinning magnetized objects) are globally charged (Michel, 1982), the cCBC signal must exist for neutron star mergers. Since the NS-NS merger systems are messy (see the previous discussion),

NS-BH mergers, especially those "plunging events" without tidal disruption of the NS, are ideal systems to observe these cCBCs. Zhang (2019) estimated that the total cCBC electromagnetic luminosity of these systems can reach 5×10^{42} erg s^{-1} for a dimensionless charge (a charge normalized to the critical charge defined by the mass of the merging member) $\hat{q} \sim 10^{-7}$. Another channel to power an EM counterpart in the plunging NS-BH merger systems is to invoke a charged BH due to its interaction with the magnetic field of the companion NS, making the system a black hole battery (Mingarelli, Levin, and Lazio, 2015; Levin, D'Orazio, and Garcia-Saenz, 2018). Dai (2019) showed that such a mechanism can produce a detectable EM transient (probably in the x-ray band), especially if the BH carries a rapid spin. The postmerger system of such NS-BH mergers may also release the BH spin energy to power a brief EM transient (Pan and Yang, 2019; Zhong, Dai, and Deng, 2019).

For nonplunging events, the standard magnetospheric interaction effect may not be important (unless the BH is charged, as I later discuss). However, if jetlike materials can be released before the merger, the synchrotron maser mechanism may still operate to produce FRB-like events (Sridhar, Zrake *et al.*, 2021).

- *BH-BH mergers.*—BH-BH mergers are not supposed to produce any EM counterparts unless they are surrounded by either matter or electromagnetic fields. In the former case, the EM signals should typically have long durations unless the matter density is close to the nuclear density.[26] In the latter case, brief FRB-like events may be emitted if at least one of the BHs is charged during the cCBC process (Zhang, 2016). This process has been robustly supported from numerical relativity simulations (Liebling and Palenzuela, 2016). Other related ideas include merger-induced discharge of Kerr-Newman BHs (Liu *et al.*, 2016) and direct electric dipole radiation from merging charged primordial BHs (Deng *et al.*, 2018). One commonly asked question involves how BHs attain and retain significant charges. Interesting facts are that collapse of a spinning neutron star would leave behind a spinning BH with charge, i.e., a Kerr-Newman BH, and that the charge does not appear to rapidly deplete (Nathanail, Most, and Rezzolla, 2017). The charge may be retained if a force-free magnetosphere is formed around the Kerr-Newman BH. Another possibility is that two BHs are merging in a magnetized environment (such as an AGN disk). The BHs will gain charges via the Wald mechanism (Wald, 1974) and launch a Poynting flux whose luminosity rapidly increases toward the merger (Kelly *et al.*, 2017).

There are other one-off FRB models. They either are exotic or have been significantly constrained by the observational data. I list some examples in the following:

---

[26]The free fall timescale, which is the shortest timescale in an accretion system, is proportional to $\rho^{-1/2}$, where ρ is the mass density. For a typical stellar density, this timescale is of the order of 10^2–10^3 s (Zhang, 2018c), which is much longer than the milliseconds relevant to FRBs.

- *Schwinger pairs at the birth of magnetars.*—Lieu (2017) suggested that at the birth of a rapidly spinning magnetar abundant pairs would be produced from the polar cap region with the Schwinger mechanism, i.e., pairs are drawn from vacuum by strong electric fields. The pairs produce FRBs by bunched coherent curvature radiation. The star would be quickly spun down in milliseconds, and the source is not expected to repeat. The main difficulty of such a model is that a new magnetar born during a massive star core collapse is buried inside the exploding star and the source is highly opaque when the suggested process happens. Even though it was not discussed in the original paper, one way to produce a naked magnetar might be through a NS-NS merger. Such a model would then fall into the previously discussed broad category of NS-NS merger models.

- *Primordial black hole evaporation.*—Primordial BHs with mass $M_c \sim 5 \times 10^{14}$ g (Rice and Zhang, 2017) are now supposed to evaporate. Besides making γ rays (Hawking, 1974), these events were suggested to emit radio waves as well (Rees, 1977). Keane et al. (2012) suggested that this mechanism could be one possibility to interpret FRBs. Since the total energetics of such an event is $\sim 10^{21} M_c \sim 5 \times 10^{35}$ erg (Rees, 1977), this model is relevant only if FRBs are nearby (for instance, within the Galaxy). The cosmological distance of FRBs and their much greater isotropic energies rule out this mechanism to interpret FRBs.

- *White hole explosions.*—White holes (WHs) are hypothetical objects in general relativity that have the opposite properties as black holes. Some quantum gravity theories predict black-to-white transition as a vast amount of energy falls into a black hole reaching the Planck density. The quantum gravity pressure would push the matter backward, making a white hole. Primordial BHs with mass $\sim 10^{26}$ g are expected to explode today as WHs, which may generate nonrepeating FRBs (Barrau, Rovelli, and Vidotto, 2014; Barrau, Moulin, and Martineau, 2018).

G. Summary

Even if there have been more than 50 FRB source models discussed in the literature, current observational constraints and the "Occam's razor" principle have actually significantly narrowed down the model options. One can summarize the state of the art of the source models as follows:

- Repeaters are likely powered by neutron stars that can provide a large enough energy budget and frequent enough triggers, from either isolated systems or interacting systems.
- Among isolated neutron star sources, the leading candidate is magnetars. However, it is unclear whether younger (rapid rotators) or older (slow rotators) objects are more favorable for producing FRBs. Arguments in favor of both cases have been discussed in the literature. More data are needed to draw a conclusion.
- Certain interaction processes may play a role in defining the observed properties of FRBs, and probably even in triggering the bursts.

- Non-neutron-star repeating sources are not needed but are not excluded. If these sources exist, they likely involve stellar-mass BHs.
- The existence of a small population of cataclysmic FRBs is not robustly established. If they exist, blitzars and CBCs are the best guesses.

VII. ENVIRONMENTAL MODELS

Since FRBs are extragalactic phenomena, their local environments are not well observed. Nonetheless, the association with a persistent radio source for rFRB 20121102A (Chatterjee et al., 2017) and rFRB 20190520B (C. H. Niu et al., 2022) and the large DM_{host} in these two and several other sources suggest that there could be compact nebulae near some FRB sources. This led to the speculation of the association of a supernova remnant or a pulsar or magnetar wind nebula with at least some FRB sources. In addition, the apparent periodicity observed in rFRB 20180916B (Amiri et al., 2020) and probably rFRB 20121102A (Rajwade et al., 2020) raised the speculation of a binary environment for at least some FRB sources. Rapid RM variations in some active repeaters rFRB 20201124A (Xu et al., 2022) and rFRB 20180520B (Dai et al., 2022; Anna-Thomas et al., 2023) have suggested a dynamically evolving magnetized environment of these FRBs. In this section, I discuss several environmental models for FRBs.

A. Persistent radio sources

PRSs are associated with at least two active repeaters, rFRB 20121102A (Chatterjee et al., 2017) and rFRB 20190520B (C. H. Niu et al., 2022). These two sources also possess the highest absolute values of RM among FRBs: $\sim 10^5$ rad m^2 for the former (Michilli et al., 2018) and $\sim 10^4$ rad m^2 for the latter (Dai et al., 2022; Anna-Thomas et al., 2023). Leading scenarios to interpret the PRSs include supernova remnants (SNRs), FRB-heated sources, pulsar wind nebulae (PWNe), magnetar wind nebulae, or even mini AGNs, which are discussed in Secs. VII.B and VII.C. Regardless of the detailed models, it is possible to present a generic discussion of the emission properties of PRSs, which gives a relation between the specific luminosity of the PRS L_ν^{PRS} and the RM associated with the FRBs (Yang, Li, and Zhang, 2020; Yang et al., 2022).

The radiation mechanism of PRSs is likely synchrotron radiation of relativistic particles from a nebula in the vicinity of the FRB source. Since the PRS emission is not rapidly varying, it is likely that the PRS does not possess a relativistic bulk motion (unlike GRB afterglows). One interesting property of synchrotron emission is that the specific emission power of each particle depends only on the magnetic field strength B (this is because the total emission power $P_e \sim (4/3)\gamma_e^2 \sigma c \beta (B^2/8\pi)$ and the characteristic frequency $\nu_{SR} \sim (3/4\pi)\gamma_e^2(eB/m_e c)$ [Eq. (92)] are both proportional to γ_e^2, so the dependence on the electron Lorentz factor γ_e is canceled out) (Rybicki and Lightman, 1979),

$$P_\nu \simeq \sqrt{3}\phi \frac{e^3}{m_e c^2} B, \quad (155)$$

where ϕ is a factor of order unity. The peak specific luminosity of the PRS can then be estimated as

$$L_{\nu,\max} \sim N_e^R P_\nu \sim \left(\frac{4\pi}{3}R_{\mathrm{PRS}}^3 n_e \zeta_e^R\right)\left(\sqrt{3}\phi\frac{e^3}{m_e c^2}B\right), \quad (156)$$

where n_e is the total ionized electron number density, ζ_e^R is the fraction of electrons that are accelerated to relativistic speeds, and the nebula is assumed as a filled sphere with a radius R_{PRS} and a uniform magnetic field B. From Eq. (74) and assuming that the observed RM of the source is contributed mostly by the nebula (which is reasonable since other RM components are typically much smaller than the RM of the PRS), one can write RM approximately as

$$|\mathrm{RM}| \sim \frac{e^3}{2\pi m_e^2 c^4}(n_e \zeta_e^{\mathrm{NR}})(b_\| B)R_{\mathrm{PRS}}, \quad (157)$$

where ζ_e^{NR} is the fraction of ionized electrons that contribute mainly to the RM and $b_\| = B_\|/B \lesssim 1$ is a fractional number denoting the parallel component of the magnetic field. One immediately sees that both $L_{\nu,\max}$ and $|\mathrm{RM}|$ linearly depend on n_e and B, so their ratio is independent of two key parameters of the PRS, i.e.,

$$\frac{L_{\nu,\max}}{|\mathrm{RM}|} \simeq \frac{8\pi^2\phi}{\sqrt{3}}\left(\frac{\zeta_e^R}{\zeta_e^{\mathrm{NR}}b_\|}\right)(m_e c^2)R_{\mathrm{PRS}}^2. \quad (158)$$

Assuming that R_{PRS} does not differ significantly among sources, Yang, Li, and Zhang (2020) and Yang et al. (2022) suggested that the reason for a detectable PRS for rFRB 20121102A was because of its relatively large $|\mathrm{RM}|$. The nondetection of PRSs for the majority of repeating FRBs is due simply to their relatively small $|\mathrm{RM}|$ values. This suggestion is supported by the recent detection of a PRS from rFRB 20190520B, with a relatively large $|\mathrm{RM}|$ (C. H. Niu et al., 2022).

B. Supernova remnants

The association of FRBs with SNRs was suggested in the early FRB literature (Connor, Sievers, and Pen, 2016; Murase, Kashiyama, and Mészáros, 2016; Piro, 2016; Kashiyama and Murase, 2017). Prompted by the discovery of the PRS of the first repeater rFRB 20121102A, Metzger, Berger, and Margalit (2017) suggested that repeating FRBs are powered by newborn magnetars from extreme explosions such as long GRBs and SLSNe. In such a picture, an FRB source should be surrounded by an SNR, which itself makes radio emission and whose evolution dictates the secular DM and RM evolution of the FRB source (Metzger, Berger, and Margalit, 2017; Yang and Zhang, 2017; Margalit and Metzger, 2018; Piro and Gaensler, 2018; Metzger, Margalit, and Sironi, 2019). Such expected coordinated DM-RM evolution is not observed, and it is now clear that most FRB sources are not associated with dwarf-star-forming galaxies or active star-forming regions within the host galaxies, which are typical for long GRBs and SLSNe

(Bhandari et al., 2020; Heintz et al., 2020; Li and Zhang, 2020). The global FRB redshift distribution also does not seem to follow the star-formation history of the Universe; see Hashimoto et al. (2022), Qiang, Li, and Wei (2022), and Zhang and Zhang (2022), but see Shin et al. (2022). Therefore, most FRBs are probably not associated with SNRs. In any case, a small fraction of FRBs, especially the active repeaters (Chatterjee et al., 2017; C. H. Niu et al., 2022), may be associated with SNRs.

A dense SNR initially blocks FRBs due to various absorption and attenuation processes. The detailed optically thinning conditions depend on the explosion parameters (ejecta energy, mass, and speed) and the ambient medium density profile [a constant density (Piro and Gaensler (2018) or a preexplosion wind profile with $n \propto r^{-2}$ (Metzger, Berger, and Margalit (2017)]. In any case, the general condition is that the SNR's age needs to be of the order of a year or decade in order to allow FRBs to escape freely without suffering from various attenuation processes, as discussed in Sec. IV.F.

The interaction between an SNR blastwave and an ambient medium could be one source of synchrotron emission that powers the observed PRS emission observed from rFRB 20121102A and rFRB 20190520B. Metzger, Berger, and Margalit (2017) applied a parametrized self-absorbed synchrotron spectrum in the form of $F_\nu = F_0(\nu/\nu_a)^{5/2}\{1 - \exp[-(\nu/\nu_a)^{-(p+4)/2}]\}$ to fit the observed spectrum of the PRS of rFRB 20121102A and showed that it can roughly interpret the data.

An SNR around an FRB source provides a testable prediction about the secular evolution of DM and RM, as well as their temporal evolution rates (Metzger, Berger, and Margalit, 2017; Yang and Zhang, 2017; Piro and Gaensler, 2018). The detailed scaling relations, on the other hand, depend on several factors, including the density profile of the ambient medium, whether the ejecta is fully ionized, the density profile of the ejecta itself, and the ionization status of the preshocked medium. In general the evolution of an SNR includes four stages: (1) the free-expansion stage when the ejecta velocity remains constant, i.e., $v \propto t^0$; (2) the Sedov-Taylor stage after the ejecta accumulates enough mass from the medium and adiabatically decelerates with the total energy in the blast wave conserved; (3) the snowplow phase when the ejecta decelerates with significant radiative cooling, which is characterized by momentum conservation; and (4) the disappearance stage in which the SNR is mixed with the ISM. The transition radius R_{dec} between the free-expansion phase and the Sedov-Taylor phase occurs when the swept mass from the medium becomes comparable to the original mass in the ejecta, with the transition time defined by $t_{\mathrm{dec}} = R_{\mathrm{dec}}/v$, where $v = (2E/M)^{1/2}$ is the velocity of the blast wave with kinetic energy E and mass M. For a medium number density n and the mean molecular weight $\mu_m \sim 1.2$, one has

$$R_{\mathrm{dec}} = \left(\frac{3M}{4\pi n\mu_m m_p}\right)^{1/3} \simeq (0.43\ \mathrm{pc})\left(\frac{M}{M_\odot}\right)^{1/3}n_2^{-1/3}, \quad (159)$$

$$t_{\mathrm{dec}} = \frac{R_{\mathrm{dec}}}{v} \simeq (42\ \mathrm{yr})E_{51}^{-1/2}\left(\frac{M}{M_\odot}\right)^{5/6}n_2^{-1/3} \quad (160)$$

for a constant-density medium (Yang and Zhang, 2017) and

$$R_{\text{dec}} = \left(\frac{M}{4\pi A}\right)^{1/3} \simeq (100 \text{ pc})\left(\frac{M}{M_\odot}\right)A_*^{-1}, \quad (161)$$

$$t_{\text{dec}} = \frac{R_{\text{dec}}}{v} \simeq (1.0 \times 10^4 \text{ yr})E_{51}^{-1/2}\left(\frac{M}{M_\odot}\right)^{3/2}A_*^{-1} \quad (162)$$

for a wind medium [see also the expressions of Metzger, Berger, and Margalit (2017) in terms of v rather than E], where $A = \dot{M}_w/4\pi v_w$ is the wind parameter and $A_* \equiv A/(5 \times 10^{11}) \text{ g cm}^{-1}$ is the typical value of A (Chevalier and Li, 1999). Note that in reality the wind profile would not extend to infinite distances. It is likely that the medium density profile would already return to the constant case long before reaching the R_{dec} of the wind model. The transition from the Sedov-Taylor phase to the snowplow phase occurs thousands of years after the explosion (Draine, 2011; Yang and Zhang, 2017). If FRBs can only be made when the neutron star engine is young, only the transition from the free-expansion phase to the Sedov-Taylor phase is relevant.

In general an SNR may be separated into four regions. From outer to inner, they are (1) the unshocked medium (ISM or wind), (2) the shocked medium, (3) shocked ejecta, and (4) unshocked ejecta, or the inner boundary of the ejecta if the reverse shock already crosses the shell. I denote regions with their respective numbers and the separation radii using the two adjacent numbers (i.e., R_{12} as the forward shock radius, R_{23} as the contact discontinuity radius, and R_{34} as the reverse shock radius or the inner boundary of the ejecta). The total DM from an SNR system can in general be calculated as

$$\text{DM}_{\text{SNR}} = \int_{R_{34}}^{R_{23}} n_3 dr + \int_{R_{23}}^{R_{12}} n_2 dr + f\int_{R_{12}}^{R_i} n_1 dr, \quad (163)$$

where R_i is the ionization front in the unshocked medium, n_i is the total electron number density in region i, and f is the ionization fraction in region (1). After delineating how R_{12}, R_{23}, R_{34}, n_2, and n_3 evolve with time, one can derive the t dependence of DM_{SNR}.

The strengths of the magnetic field in regions (2) and (3) can also be estimated by assuming that a fraction ϵ_B of the internal energy in the respective region is stored in ordered magnetic fields. Making one additional assumption that $\langle B_\parallel \rangle$ is of the same order as B in the respective region, one can then calculate the total absolute value of RM in the SNR system via

$$|\text{RM}_{\text{SNR}}| = \int_{R_{34}}^{R_{23}} \langle B_{\parallel,3}\rangle n_3 dr + \int_{R_{23}}^{R_{12}} \langle B_{\parallel,2}\rangle n_2 dr$$
$$+ f\int_{R_{12}}^{R_i} \langle B_{\parallel,1}\rangle n_1 dr \quad (164)$$

and delineate its temporal evolution.

The predicted scaling laws by various researchers and their assumptions can be summarized as follows:

- For a constant-density medium, Yang and Zhang (2017) assumed that the entire region (3) is ionized and obtained

$$\text{DM}_{\text{SNR}}^{\text{FE}} \propto t^{-2}, \qquad d\text{DM}_{\text{SNR}}^{\text{FE}}/dt \propto t^{-3} \quad (165)$$

for the free-expansion phase, and

$$\text{DM}_{\text{SNR}}^{\text{ST}} \propto t^{2/5}, \qquad d\text{DM}_{\text{SNR}}^{\text{ST}}/dt \propto t^{-3/5} \quad (166)$$

for the Sedov-Taylor phase. Note that the DM evolution scaling does not depend on the medium profile during the free-expansion phase, so the same scaling equation (165) also applies to the case of a wind medium profile with $n \propto r^{-2}$ (Metzger, Berger, and Margalit, 2017). The assumption of a fully ionized region (3) may be reasonable in view of the existence of a repeating FRB source at the center such that any remaining neutral materials between the engine and R_4 should have been ionized by x-ray emission associated with the repeated bursts; see Sec. VII.C for further discussion. One interesting finding is that $\text{DM}_{\text{SNR}}^{\text{ST}}$ increases with time. This is because the DM increase rate in the shocked medium [region (2)] is larger than the DM decrease rate in the unshocked medium [region (1)] during the self-similar deceleration phase.

- Piro and Gaensler (2018) argued that the entire ejecta is not fully ionized. Rather, only the region between the reverse shock and the forward shock is ionized.[27] Properly following the evolution of the reverse shock and assuming an ordered magnetic field in the ejecta, they considered the DM and RM evolution relations for both a constant-density medium and a wind medium. For the constant-density (ISM) case, they obtained

$$\text{DM}_{\text{SNR}}^{\text{FE,ISM}} \propto t^{-1/2}, \qquad d\text{DM}_{\text{SNR}}^{\text{FE,ISM}}/dt \propto t^{-3/2}, \quad (167)$$

$$|\text{RM}_{\text{SNR}}^{\text{FE,ISM}}| \propto t^{-1/2}, \qquad d|\text{RM}_{\text{SNR}}^{\text{FE,ISM}}|/dt \propto t^{-3/2} \quad (168)$$

in the free-expansion phase, and

$$\text{DM}_{\text{SNR}}^{\text{ST,ISM}} \propto t^{2/5}, \qquad d\text{DM}_{\text{SNR}}^{\text{ST,ISM}}/dt \propto t^{-3/5}, \quad (169)$$

$$|\text{RM}_{\text{SNR}}^{\text{ST,ISM}}| \propto t^{-1/5}, \qquad d|\text{RM}_{\text{SNR}}^{\text{ST,ISM}}|/dt \propto t^{-6/5} \quad (170)$$

in the Sedov-Taylor phase. Note that the scaling in the Sedov-Taylor (ST) phase is the same as that given by Yang and Zhang (2017), who assumed full ionization since, in the ST phase, the shocked medium [region (2)] is the dominant region to contribute to the observed DM.

- For a wind medium, Piro and Gaensler (2018) obtained

$$\text{DM}_{\text{SNR}}^{\text{FE,wind}} \propto t^{-1}, \qquad d\text{DM}_{\text{SNR}}^{\text{FE,wind}}/dt \propto t^{-2}, \quad (171)$$

$$|\text{RM}_{\text{SNR}}^{\text{FE,wind}}| \propto t^{-2}, \qquad d|\text{RM}_{\text{SNR}}^{\text{FE,wind}}|/dt \propto t^{-3} \quad (172)$$

---

[27]This assumption requires scrutiny because, since a newborn SNR is likely hot, regions outside the shocked region are also likely ionized. FRB-associated x rays will also ionize any neutral atoms in the region.

in the free-expansion phase, and

$$DM_{SNR}^{ST,wind} \propto t^{-2/3}, \qquad d DM_{SNR}^{ST,wind}/dt \propto t^{-5/3}, \quad (173)$$

$$|RM_{SNR}^{ST,wind}| \propto t^{-4/3}, \qquad d|RM_{SNR}^{ST,wind}|/dt \propto t^{-7/3} \quad (174)$$

in the Sedov-Taylor phase.

C. Pulsar wind nebulae and FRB-heated nebulae

The FRB source, likely a young magnetar, would eject a wind through spin-down and may eject even stronger winds during flaring activities. The wind would interact with the surrounding supernova remnant to form a PWN. This PWN may play an important role in powering the FRB emission itself through synchrotron maser emission (Lyubarsky, 2014; Metzger, Margalit, and Sironi, 2019), may contribute to the observed DM or RM (Margalit, Berger, and Metzger, 2019; Metzger, Margalit, and Sironi, 2019), and may contribute to the emission of PRS as well.

Dai, Wang, and Yu (2017) argued that a repeating FRB source does not necessarily need to have a surrounding supernova remnant to generate a PRS. The wind from the FRB pulsar may interact with the surrounding medium to form a pulsar wind nebula and power persistent radio emission. However, to power a detectable PRS as observed from FRB 20121102A, the central pulsar needs to be rapidly spinning (for instance, $P \lesssim 10$ ms, to allow a large energy budget) and does not possess a strong magnetic field (to allow a long spin-down timescale).

Yang, Zhang, and Dai (2016) noticed that the interaction between the FRB ejecta and a surrounding synchrotron nebula could play an important role in both nebular emission and FRB emission. In particular, for certain parameters, the FRB frequency could be below the synchrotron self-absorption frequency of the nebula. These FRBs would be absorbed and could not reach the observer. Rather, they would heat up the synchrotron nebula and make a bump in the synchrotron spectrum near the absorption frequency. This prediction was found to be suitable for interpreting the spectrum of PRS of FRB 20121102A after the latter was discovered (Li, Yang, and Dai, 2020).

Within the framework of an accreting black hole central engine, Sridhar and Metzger (2022) proposed a "hypernebula" model for FRBs. The intense mass loss from a super-Eddington accretion disk produces an energetic, expanding bubble that acts like a magnetar wind to produce a synchrotron-emitting nebula. The model was found to be suitable for interpreting the PRSs of some repeating FRBs.

D. Binary systems

A widely discussed FRB source environment is binary systems, in which the companion (a massive star, another neutron star, or even a massive black hole) of the FRB source (likely a pulsar or magnetar) plays a noticeable role in shaping the properties of the detected bursts. Binary interaction was invoked as one of the mechanisms to trigger FRBs within the cosmic comb model (Zhang, 2017). Discussion of binary systems became popular after the discovery of the $\sim$16-d period of rFRB 20180916B (Amiri et al., 2020), as the

observed period may be interpreted as the orbital period of the binary system. It was quickly realized that the massive companion of the FRB pulsar could provide a strong, opaque wind to block FRBs in certain directions, so repeated bursts could only be observed in certain orbital phases (Ioka and Zhang, 2020; Lyutikov, Barkov, and Giannios, 2020). More generally Wada, Ioka, and Zhang (2021) discussed three possible modes for companion–FRB source interactions: (1) The *funnel mode* is the mode in which the companion wind is generally stronger than the FRB pulsar wind, so the latter can open a funnel only as the pressures of the two winds balance. The funnel is visible by the observer at certain orbital phases (Ioka and Zhang, 2020; Lyutikov, Barkov, and Giannios, 2020). (2) The *τ-crossing mode* is the mode in which the active window is defined by the orbital phases where the optical depth of FRB against Thomson scattering, free-free absorption, and induced Compton scattering becomes less than unity or a few. The FRB source pulsar crosses the photosphere twice during the orbital motion, and only when the orbit is above the photosphere could the FRB emission be observed. (3) The *inverse funnel mode* is the opposite case of the funnel mode in which the FRB pulsar wind is generally stronger than the companion wind and the active phase is greater than half of the period. Zhang and Gao (2020) studied various binary systems, including one NS companion using population synthesis models and found that a 16-d period is common and the companion is likely a *B*-type star. The frequency-dependent periodic window of rFRB 20180916B has been raised as evidence against the simple binary comb scenario (Pastor-Marazuela et al., 2021). However, several scenarios have been proposed to account for observations within various binary scenarios (Li and Zanazzi, 2021; Q.-C. Li et al., 2021; Wada, Ioka, and Zhang, 2021).

The complicated RM evolution as well as apparent Faraday conversion observed in rFRB 20201124A (Xu et al., 2022) does not directly point toward a binary system (due to the lack of periodicity). However, a detailed modeling of the polarization properties of the system requires multiple layers of plasma to contribute to RM and radio wave absorption, and a binary system is a likely possibility to account for the data (Wang, Zhang et al., 2022; Yang, Xu, and Zhang, 2022; Li et al., 2023).

An extreme version of binary systems is to have the FRB pulsar orbiting a massive or even a supermassive black hole. Zhang (2018b) suggested that rFRB 20121102 may reside near a supermassive black hole whose AGN-like activities may be powering the persistent radio emission of the source. It is interesting that the parameter space allowed for the binary comb model to interpret its $\sim$157-d period also prefers a supermassive black hole as its companion (Wada, Ioka, and Zhang, 2021). The large absolute RM value and sign change observed in rFRB 20190520B may also be interpreted by invoking a massive black hole in the vicinity of the source (Dai et al., 2022; Anna-Thomas et al., 2023).

VIII. PROPAGATION EFFECTS

Besides the standard dispersion and Faraday rotation, FRB radio waves undergo additional propagation effects before being detected on Earth. The propagation effects may leave imprints on the observed signals, and the observed information

may in turn be used to diagnose the physical properties of the medium through which FRB waves propagate.

A. Multipath effects: Scattering, scintillation, and RM scatter

One important feature of radio wave propagation is that the observed radio waves at a particular time are likely the superposition of rays from multiple paths. This is because the frequency-dependent propagation speed of radio waves depends on the plasma density the waves propagate through and because the densities along the multiple lines of sight likely have fluctuations, most likely because of turbulence that is ubiquitous in astrophysical environments. These fluctuations would spread the rays, blur the image, broaden the radio pulse, and smear the bandwidth. All these effects are characterized as scattering (describing pulse broadening) and scintillation (describing intensity fluctuation and bandwidth smearing) (Rickett, 1977,1990).

Scattering is often manifested as a temporal scattering tail in FRB pulses. Let the FRB and a thin plasma screen (lens) be located at the angular diameter distances D_s and D_l from Earth, respectively. Let the angular diameter distance between the source and the screen be D_{sl}, which is close to but not equal to $D_s - D_l$ for cosmological sources. The scattering half angle θ_s and the scattering timescale τ_s can be calculated as (Rickett, 1977, 1990; Macquart and Koay, 2013; Cordes *et al.*, 2016; Xu and Zhang, 2016; Yang *et al.*, 2022), i.e.,

$$\theta_s \simeq \frac{D_{ls}(\lambda/2\pi)}{D_s r_{\text{diff}}}, \tag{175}$$

$$\tau_s \simeq \frac{\lambda}{2\pi c}\left(\frac{r_F}{r_{\text{diff}}}\right)^2 = \frac{D_l D_s \theta_s^2}{c D_{ls}(1+z_l)}$$
$$= \frac{D_l D_{ls}(\lambda/2\pi)^2}{c D_s r_{\text{diff}}^2(1+z_l)} \overset{D_s = D_l}{=\!=\!=} \frac{D_{ls}(\lambda/2\pi)^2}{c r_{\text{diff}}^2(1+z_l)}, \tag{176}$$

where λ is the observed wavelength (longer by a factor of $1 + z_l$ than that at the scattering screen) and z_l is the redshift of the screen (lens). Because in the FRB case the screen is usually in the host galaxy, when relevant I also write the simpler expression in Eq. (176) for the case of $D_s = D_l$. Here there are two important length scales. One is the Fresnel scale,

$$r_F = \left[\frac{D_l D_{ls}(\lambda/2\pi)}{D_s(1+z_l)}\right]^{1/2} \overset{D_s = D_l}{=\!=\!=} \left[\frac{D_{ls}(\lambda/2\pi)}{1+z_l}\right]^{1/2}, \tag{177}$$

which is the geometric mean of the effective distance $D_{\text{eff}} = D_l D_{ls}/D_s$ and the rest-frame reduced wavelength $\lambdabar_s = \lambda/[2\pi(1+z_l)]$. For a spherical wave, this is the transverse scale of the wave front where the light path difference is $\lambdabar_s$ at a distance of D_{eff}.

A more important distance scale is the so-called diffractive length scale r_{diff}, which is the transverse scale of the wave front where the root-mean-square difference between the two rays is $\lambdabar_s$. Assume that the scattering effect is introduced by electron density fluctuations that arise from a turbulent cascade and that the relevant spectrum takes the power-law form in wave number k (Rickett, 1977; Cordes, Weisberg, and Boriakoff, 1985; Cordes and Lazio, 2002; Macquart and Koay, 2013; Xu and Zhang, 2016),

$$P_{\delta n_e}(k) = C_n^2 k^{-\beta}, \qquad 2\pi/L \leq k \leq 2\pi/l_0, \tag{178}$$

where l_0 and L are the inner (dissipation) and outer (injection) scales of the turbulent energy, C_n^2 is the spectral coefficient (the amplitude of turbulence) that describes the significance of the density fluctuations, and β is the spectral index, which equals 11/3 for the Kolmogorov turbulent spectrum but can take a more general value. The turbulence is short-wave dominated when $\beta > 3$ and long-wave dominated when $\beta < 3$. From the density variance $\langle(\delta n_e)^2\rangle = \int P_{\delta n_e}(k)d^3\mathbf{k}$ and $L \gg l_0$, one can write (Xu and Zhang, 2016)

$$C_n^2 \sim \frac{\beta - 3}{2(2\pi)^{4-\beta}}(\delta n_e)^2 L^{3-\beta}, \qquad \beta > 3, \tag{179}$$

$$C_n^2 \sim \frac{3 - \beta}{2(2\pi)^{4-\beta}}(\delta n_e)^2 l_0^{3-\beta}, \qquad \beta < 3. \tag{180}$$

It is convenient to define a *scattering measure* (SM) as the line integration of C_n^2 along the line of sight (Cordes, Weisberg, and Boriakoff, 1985; Cordes and Lazio, 2002)

$$\text{SM} = \int_0^D C_n^2 dl \simeq C_n^2 \Delta, \tag{181}$$

where in Eq. (181) it has been assumed that scattering happens only in a thin screen with thickness Δ. One can finally write the expression of r_{diff} in the two regimes (Xu and Zhang, 2016)

$$r_{\text{diff}} \sim (\pi r_e^2 \lambda^2 \text{SM} l_0^{\beta-4})^{-1/2}, \qquad r_{\text{diff}} < l_0, \tag{182}$$

$$r_{\text{diff}} \sim (\pi r_e^2 \lambda^2 \text{SM})^{1/(2-\beta)}, \qquad r_{\text{diff}} > l_0, \tag{183}$$

where $r_e = e^2/m_e c^2$ is the classical radius of the electron. After all these preparations, one can finally derive an observed scattering timescale that has the dependence (Xu and Zhang, 2016; Yang *et al.*, 2022)

$$\tau_{\text{sc}}^{\text{obs}} = (1+z_l)\tau_{\text{sc}}$$
$$\propto \begin{cases} \delta n_e^2 \Delta^2 \lambda^4 (1+z_l)^{-3}, & r_{\text{diff}} < l_0, \\ \delta n_e^{4/(\beta-2)} \Delta^{\beta/(\beta-2)} \lambda^{2\beta/(\beta-2)}(1+z_l)^{-(\beta+2)/(\beta-2)}, & r_{\text{diff}} > l_0, \end{cases} \tag{184}$$

regardless of the regime of β. For Kolmogorov turbulence with $\beta = 11/3$, the numerical value of the index is $2\beta/(\beta - 2) = 22/5 = 4.4$. The value of $\tau_{\text{sc}}^{\text{obs}}$ depends on the SM, and for FRB parameters the contribution of $\tau_{\text{sc}}^{\text{obs}}$ from the host galaxy or the immediate environment of the FRB source is much greater than those from the IGM and from the Milky Way (Cordes *et al.*, 2016; Xu and Zhang, 2016).

With the scattering timescale, one can immediately define a scintillation bandwidth

$$\Delta\nu_s \sim 1/\tau_{\rm sc} \sim (1 \text{ kHz})\tau_{-3}^{-1}, \tag{185}$$

which is too small to be identified in the observing band of the telescopes for millisecond scattering. On the other hand, scintillation band fringes are detected in the radio band, which should have a much different origin. For FRBs, the detected scintillation bandwidth is likely dominated by the multipath propagation effect within the Milky Way Galaxy.

The multipath effect can also affect the observed polarization properties. For linearly polarized FRB emission, the multipath effect can introduce an RM scatter (Feng *et al.*, 2022); i.e., different lines of path undergo different Faraday rotations such that the final observed emission is depolarized (Beniamini, Kumar, and Narayan, 2022; Yang *et al.*, 2022). The RM scatter may be estimated as (Yang *et al.*, 2022)

$$\sigma_{\rm RM} \simeq \frac{e^3}{2\pi m_e^2 c^4}(l_s\Delta)^{1/2}\delta(n_e B_\parallel)_{l_s}$$
$$= (0.81 \text{ rad m}^{-2})\left(\frac{\sqrt{l_s\Delta}}{1 \text{ pc}}\right)\left(\frac{\delta(n_e B_\parallel)_{l_s}}{1 \text{ cm}^{-3}\text{ μG}}\right), \tag{186}$$

where $\delta(n_e B_\parallel)_{l_s}$ is $\delta(n_e B_\parallel)$ on the scale of l_s and

$$l_s(\lambda) \simeq \frac{\lambda D_{ls}}{2\pi r_{\rm diff}} \tag{187}$$

is the maximum transverse scale of the multipaths. The effect of $\sigma_{\rm RM}$ is to introduce a frequency-dependent polarization degree, with the fractional reduction of the linear polarization amplitude defined by $f_{\rm RM,depol} \equiv 1 - \exp(-2\lambda^4\sigma_{\rm RM}^2)$ (O'Sullivan *et al.*, 2012; Feng *et al.*, 2022). This effect presents an interpretation of the frequency-dependent linear polarization degree of a sample of repeating FRBs (Feng *et al.*, 2022).

One prediction of the RM scatter theory is that it is positively correlated to the observed scattering timescale, i.e., $\sigma_{\rm RM} \propto \tau_{\rm sc}^\alpha$, with $\alpha \sim 0.5$–0.8 (Yang *et al.*, 2022). This is qualitatively consistent with the observational data (Feng *et al.*, 2022).

Another mechanism to scatter FRB emission is through filamentation of the FRB waves in a magnetar wind. This may induce additional modulation in the emission with a $\tau_{\rm sc} \propto \nu^{-2}$ scattering dependence, which is not widely observed (Sobacchi, Lyubarsky, Beloborodov, and Sironi, 2022). On the other hand, such an effect may induce large scintillation bandwidths of ∼100 MHz as observed, which corresponds to an undetectable nanosecond-duration scattering timescale (Sobacchi, Lyubarsky, Beloborodov, and Sironi, 2022).

B. Plasma lensing and gravitational lensing

An extreme version of the plasma multipath effect is plasma lensing (Cordes *et al.*, 2017). In general a denser lens with a positive electron column density would serve as a diverging lens, but rays passing through different parts of the lens,

especially from voids, may converge to generate caustics that amplify burst signals. Since plasma lenses may be dynamically evolving, the lensed bursts can allow different spectral behaviors, in contrast to gravitational lensing, which retains a spectral shape.

The simplest model is a 1D Gaussian plasma lens model (Clegg, Fey, and Lazio, 1998) that can be described as $\text{DM}(x) = \text{DM}_l \exp(-x^2/x_0^2)$, where x_0 is the characteristic transverse scale of the lens and x is the transverse coordinate. Let the transverse coordinates in the source, lens, and observer's planes be given by x_s, x, and $x_{\rm obs}$, respectively, and define the dimensionless coordinates $u_s = x_s/x_0$, $u = x/x_0$, and $u_{\rm obs} = x_{\rm obs}/x_0$. The lens equation in geometric optics can be expressed as

$$u(1 + \alpha e^{-u^2}) = u' \tag{188}$$

through the Kirchhoff diffraction integral of the Gaussian lens (Cordes *et al.*, 2017). In Eq. (188)

$$u' = (D_l/D_s)u_s + (D_{ls}/D_s)u_{\rm obs} \tag{189}$$

and

$$\alpha = \frac{\lambda^2 r_e \text{DM}_l}{\pi x_0^2}\left(\frac{D_{ls}D_l}{D_s}\right) \tag{190}$$

is a dimensionless parameter. The amplification factor can be written as

$$G = |1 + \alpha(1 - 2u^2)e^{-u^2}|^{-1}, \tag{191}$$

which has a maximum

$$G_{\rm max} \sim x_0/r_{\rm F} \tag{192}$$

at the caustics where $\alpha = \alpha_{\rm min}$. Cordes *et al.* (2017) constrained the lens parameters required to have caustics, which read $\text{DM}_l D_{ls}/x_0^2 \gtrsim 0.65 \text{ pc}^2 \text{ A.U.}^{-2} \text{ cm}^{-3}$. They argued that the apparently more active repetition behavior of rFRB 20121102A compared to other sources may be a consequence of significant plasma lensing. The discoveries of several more active repeaters cast doubt on interpretations of all of them with the plasma lensing effect and tend to suggest that different FRBs may have different active levels, and that some of them (perhaps young magnetars) are intrinsically more active than others. Nonetheless, plasma lensing may leave certain imprints in FRB observations. For example, Er, Yang, and Rogers (2020) argued that frequency-dependent delay due to the geometric effect could be comparable to the dispersion delay, so the measured DM could be overestimated if signals propagate through a high-density gradient clump of plasma.

Like other astronomical objects, FRBs can undergo gravitational lensing. The high event rate of FRBs makes it plausible for lensed FRBs to be detected as the detected sample increases quickly with time (Li and Li, 2014). Since gravitational lenses are not dynamically evolving, multi-images

of the lensed bursts would be more analogous to each other with a strict delay timescale for all the bursts from the same repeater source. The combination of observing multiple images with VLBI and the time delay of the images would allow a direct probe of the proper motion of a repeating FRB, which directly constrains the physical conditions at the source (Dai and Lu, 2017).

C. Large-amplitude-wave effects

One unique property of FRB waves, thanks to their high luminosities in radio frequencies, is that at a small enough radius from the engine the amplitude of the electromagnetic waves is so large that electrons interacting with the waves move with a relativistic speed. For an FRB with luminosity L, the Poynting flux at a distance r from the source is $F = L/4\pi r^2$, which can also be written in terms of the EM wave amplitude $F = cE_w^2/8\pi \simeq cB_w^2/8\pi$. As a result, the wave amplitude can be written as

$$E_w \simeq B_w = \sqrt{\frac{2L}{cr^2}} = (820 \text{ esu or G})L_{42}^{1/2}r_{13}^{-1}. \quad (193)$$

One can define a dimensionless parameter

$$a \equiv \frac{eE_w}{m_e c\omega} = \frac{\omega_{B_w}}{\omega} \quad (194)$$

of a wave for its amplitude (where $\omega_{B_w} = eB_w/m_e c = eE_w/m_e c$), which is essentially the dimensionless oscillation velocity $v_{\rm osc}/c$ of an electron in response to the wave in which $a < 1$. Plugging in the typical FRB parameters, one has

$$a = 2.3L_{42}^{1/2}r_{13}^{-1}\nu_9^{-1}. \quad (195)$$

One can see that for an $L = 10^{42}$ erg s^{-1} FRB, the amplitude factor is $a \gg 1$ when $r \ll 10^{13}$ cm. In such a large-amplitude-wave regime, a series of propagation effects not shared by low-amplitude radio waves are introduced. Similar effects apply to laboratory lasers, which can require large intensities to reach the relativistic regime. The importance of large-amplitude effects within the context of FRBs was first pointed out by Luan and Goldreich (2014) and later discussed in various contexts by Gruzinov (2019), Beloborodov (2020), Kumar and Lu (2020), Lu and Phinney (2020), and Yang and Zhang (2020). In analogy to the large-amplitude-wave effects for laboratory lasers, Yang and Zhang (2020) systematically studied the large-amplitude effects for FRBs, which can be summarized as follows:

- *Enhancement of emission cross section.*—In the $a \gg 1$ regime, an electron moves in a "figure-eight" trajectory because, besides the traditional harmonic motion due to the oscillating E_w, it is also affected by the Lorentz force from the oscillating B_w (Sarachik and Schappert, 1970). In the oscillation-center rest frame, the electron moves with a Lorentz factor $\gamma' = a/\sqrt{2}$. As with synchrotron radiation, the emission power of the electron is $P \sim a^2 P_T$, where $P_T = e^4 E_w^2/3m_e^2 c^3$ is the power received given by the Thomson formula. Considering that

the Poynting energy flux in the waves is $S = cE_w^2/8\pi$ and that the cross section is defined as $\sigma = P/S$, one obtains (Yang and Zhang, 2020)

$$\sigma = \frac{P}{S} \sim a^2 \sigma_T. \quad (196)$$

With the existence of a background magnetic field B, as is the case for FRBs emitted from a magnetar magnetosphere, the problem becomes more complicated. In the inner magnetosphere where $B \gg B_w$ is satisfied, the large-amplitude effect is suppressed since the electron is confined by the much stronger background B. In a dipolar field, one has $B \propto r^{-3}$, which decays faster than $B_w \propto r^{-1}$. As a result, the large-amplitude effect would become important when B becomes smaller than B_w (Beloborodov, 2021a, 2021b). Detailed numerical results suggest that σ/σ_T is typically greater than a^2, with a dependence on the angle between the wave vector k and the B vector and the relationship between ω_B/ω and a (Qu, Kumar, and Zhang, 2022). When the plasma streams outward relativistically, bright FRBs can propagate through it and successfully escape the plasma (Qu, Kumar, and Zhang, 2022).

- *Transparency of strong waves.*—In the $a \gg 1$ and weak magnetic field regime (far from the magnetosphere), the dispersion relation for a circularly polarized wave is modified as (Yang and Zhang, 2020)

$$\omega^2 = k^2 c^2 + \frac{\omega_p^2}{\gamma}, \quad (197)$$

where $\gamma = (1 + a^2/2)^{1/2}$. This effectively reduces the near-source plasma frequency by a factor of $\sqrt{\gamma}$ or reduces the plasma density by a factor of γ. This would reduce the DM contribution from the vicinity of the FRB source (for instance, within 1 A.U. for a $L = 10^{42}$ erg s^{-1} burst) by a factor of $\sim\gamma$, making the FRB more transparent (Lu and Phinney, 2020; Yang and Zhang, 2020). The FRB-induced medium filamentation (Sobacchi *et al.*, 2022) would further modify the dispersion relation [Eq. (197)] and further reduce the near-source DM.

- *Relativistic self-focusing.*—In the $a \gg 1$ regime, the nonlinear refractive index is $n_r = c/v_p = \sqrt{1 - \omega_p^2/\gamma(a)\omega^2}$, which is intensity dependent. Consider a beamed FRB with a decreasing intensity from the center. The propagation effect naturally "squeezes" the light, making the FRB more beamed (Yang and Zhang, 2020). Such an effect is especially important for a high-density emitter, for instance, in the synchrotron maser scenario. The squeezing effect becomes negligible in a magnetosphere environment (Lyutikov, 2020a).

- *Ponderomotive force electron acceleration in wakefield waves.*—An electromagnetic pulse with a nonuniform energy density (as in the case of an FRB) would exert a ponderomotive force $\vec{F}_p = -m_e c^2 \nabla(1 + \langle \vec{a}^2 \rangle)^{1/2}$ in the relativistic regime, where $\vec{a} = e\vec{A}/m_e c^2$ ($\vec{A}$ is the vector

potential, i.e., $\vec{B} = \nabla \times \vec{A}$) is a dimensionless vector whose amplitude is comparable to a for the ambient plasma. Electrons would be more easily expelled away from equilibrium due to the radiation pressure, forming an oscillating electrostatic field in the plasma. This is the so-called wakefield wave. Such a field would accelerate electrons. However, this effect is too small to be observationally interesting (Yang and Zhang, 2020).

IX. FRBS AS ASTROPHYSICAL AND COSMOLOGICAL PROBES

Regardless of their physical origins, FRBs are effective cosmic probes that can be used to study various problems in astrophysics, cosmology, and even fundamental physics. In this section I summarize some proposed applications of FRBs as cosmological probes. Reviews on these subjects were also given by Bhandari and Flynn (2021) and Xiao, Wang, and Dai (2021).

A. Missing baryons: Ω_b and f_{IGM}

Most of the following probes make use of the salient feature of the $\langle DM_{IGM} \rangle$-z relation [Eq. (10)], which makes a connection between two observables DM and z. The complication is that there are multiple components that contribute to DM [Eq. (9)]. However, in most cases DM_{IGM} is the dominant term. If one can properly deduct other components, one can directly measure $\Omega_b f_{IGM}$ from the data [Eq. (10)]. This has been done with a small sample of FRBs (Macquart et al., 2020). The results are consistent with indirectly inferred Ω_b from cosmic microwave background and big bang nucleosynthesis measurements (Boesgaard and Steigman, 1985; Aghanim et al., 2020). This solves the long-standing "missing baryon problem" and suggests that the majority of missing baryons are in the intergalactic medium. If one adopts the best-fit Ω_b from the cosmic microwave background (CMB) measurements, one can directly constrain f_{IGM}. The results inferred from FRBs [see Z. Li et al. (2020) and Fig. 4, right panel] are generally in agreement with previous results using other methods (Fukugita, Hogan, and Peebles, 1998).

B. IGM inhomogeneity

Equation (10) is an average relationship. For individual lines of sight, the measured DM at the same z could be much different because the IGM is inhomogeneous. Numerical simulations (McQuinn, 2014) showed that the standard deviation $\sigma[DM]$ of the DM distribution ranges from 180 to 400 cm^{-3} pc at $z = 1$ depending on whether the "missing" baryons lie around the virial radius of 10^{11}–$10^{13} M_\odot$ halos or farther out. Jaroszynski (2019) showed $\sim 13\%$ scatter of DM at $z = 1$ and $\sim 7\%$ scatter at $z = 3$ using Illustris simulation; see also Takahashi et al. (2021). Macquart et al. (2020) presented a sample of eight FRBs with z measurements, which indeed showed a large scatter and expected the range of scatter to increase with redshift. The current data for 21 z-known FRBs (Fig. 4, right panel) do not show such a trend. Li et al. (2019) reconstructed the DM-z relation for nearby FRBs using the observed optical galaxy data and the halo baryon distribution

models and found that the inferred DM_{IGM} values for individual FRBs indeed deviate significantly from the predicted values based on the average relation (10). A more detailed study of FRB 20190608 making use of both optical and radio data led to a reconstruction of the cosmic web along the line of sight (Simha et al., 2020). With a much larger sample of localized FRBs with z measurements, the scatter of the DM_{IGM}-z relation will be mapped directly from the data. This scatter is also important for deciding how good FRBs are to serve as other types of probes, as later discussed.

C. Circumgalactic medium

Individual galaxies are surrounded by a circumgalactic medium (CGM), which is the gas surrounding the galaxies outside their disks or ISM but inside the virial radii. The properties of the CGM are poorly studied. The amount of mass in the CGM would affect the scatter of the DM_{IGM}-z relation. FRBs can probe the CGM directly, for either the halo of our own Milky Way Galaxy or the halo of foreground galaxies along the line of sight of some FRBs. Low DM FRBs from nearby galaxies can be used to directly constrain DM_{halo} of the Milky Way (Prochaska and Zheng, 2019). Analyses of the radio data of FRB 20181112 have posed strong constraints on the properties of the halo of a foreground galaxy, which has a low net magnetization and turbulence (Prochaska et al., 2019). The studies in this direction will flourish as more data are accumulated.

D. FRB host galaxy and the surrounding medium

Another uncertainty that hinders the application of the DM_{IGM}-z relation to probe the Universe is the DM contribution from the FRB host galaxy as well as the immediate medium around the FRB source. Both are poorly known and difficult to measure because they are degenerate with DM_{IGM}, which itself has a large uncertainty. Nonetheless, DM_{host} and DM_{src} have been studied from different aspects. Theoretically Xu and Han (2015) simulated the DM distributions for three types of FRB hosts and different viewing angles. The DM contribution from a dense medium (such as a supernova remnant) around FRBs has been extensively modeled (Metzger, Berger, and Margalit, 2017; Yang and Zhang, 2017; Piro and Gaensler, 2018). Observationally some FRBs with an apparent excess DM [for instance, rFRB 20121102A (Tendulkar et al., 2017) and rFRB 20190520B (C. H. Niu et al., 2022)] have shown evidence of a large $DM_{host} + DM_{src}$. Information of the host galaxy type and relative position of the FRB in its host galaxy (Tendulkar et al., 2017; Bannister et al., 2019; Bhandari et al., 2020; Xu et al., 2022) can also help one to estimate the DM contribution to the host galaxy. If one assumes that the $DM_{host} + DM_{src}$ of a large sample of FRBs follow a normal distribution (which may be the case if the outliers such as rFRB 20190520B are removed), the average DM contribution from the host or source may be statistically inferred using the observed DM-fluence relation (Yang et al., 2017) or DM-z relation (Z. Li et al., 2020). With five FRBs with z measurements, Z. Li et al. (2020) estimated the local value of $DM_{host} + DM_{src}$ as $\sim 107^{+24}_{-45}$ pc cm^{-3} (the measured value is smaller by a factor

of $1 + z$). The larger sample of the current 21 FRBs leads to a similar constraint; see Fig. 4 and the related discussion. With a large enough sample, $DM_{host} + DM_{src}$ can also be directly inferred through a differential increase of the observed DM_E with z (Yang and Zhang, 2016). From cosmological simulations, it was found that DM_{host} is redshift dependent and that the median value ranges from ~ 35 pc cm^{-2} at $z = 0.1$ to ~ 106 pc cm^{-2} at $z = 1.5$ (G. Q. Zhang et al., 2020).

E. Dark energy

Supposing that a large sample of FRBs are localized and z measured, the IGM inhomogeneity and host or source DM contribution can be better quantified. This would create an opportunity to compare the data with different $\langle DM_{IGM} \rangle$-z models and constrain relevant model parameters. The first exciting prospect is to use FRBs to constrain the evolution of the Universe, in particular, the nature of dark energy as delineated by the $E(z)$ function in Eq. (7). Simulations (Gao, Li, and Zhang, 2014; Zhou et al., 2014; Walters et al., 2018) suggest that, depending on the degree of IGM inhomogeneity, meaningful constraints on dark energy may be achieved with a large enough sample, especially in combination with other cosmological probes such as type Ia supernovae, CMB, and baryon acoustic oscillations. The challenges for robustly extracting distance and the quantitative estimates of the systematics control needed for FRBs to be competitive distance probes were discussed by Kumar and Linder (2019).

F. Reionization history

Another prospect of using the $\langle DM_{IGM} \rangle$-z relation as a cosmological probe is to probe the reionization history of the Universe. This is because the observed DM is contributed only by free electrons. The relation [Eqs. (10) and (11)] carries the ionization fraction for both H and He (Deng and Zhang, 2014; Zheng et al., 2014). Theoretical modeling and observational constraints suggest that He might be fully ionized at $z \sim 3$ (Zheng et al., 2014), whereas H is ionized at $z > 6$ (Fan, Carilli, and Keating, 2006). The detailed ionization history, especially that of H ionization in the so-called dark ages, is not well constrained, and FRBs can potentially probe it directly. Detailed simulations (Caleb, Flynn, and Stappers, 2019; Bhattacharya, Kumar, and Linder, 2021) showed that He ionization from $z = 3$ to 6 can be differentiated with $(1.6 \times 10^3) - 10^4$ FRBs. For H reionization, the epoch of reionization may be constrained via an observed DM_{max} or 40 FRBs detected at redshifts $z \in (6, 10)$ (Beniamini et al., 2021).

G. Large-scale structure and turbulence

With the DM and spatial distribution of a large sample, one can perform a study of the angular correlation of DMs for FRBs, extracting their structure function and correlation function to probe the large-scale structure (Shirasaki et al., 2022), or even turbulence at large scales. The pre-CHIME sample showed preliminary evidence of possible large-scale turbulence (Xu and Zhang, 2020), which is not confirmed

with the larger CHIME sample (Xu, Weinberg, and Zhang, 2021). Nonetheless, the results are broadly consistent with the statistical modeling of the cosmological DM from numerical simulations (Takahashi et al., 2021). Rafiei-Ravandi et al. (2021) found a statistically significant cross-correlation between CHIME FRBs and galaxies in the redshift range $z \in (0.3, 0.5)$.

H. Source and intergalactic magnetic fields

Besides using DM to perform various constraints, a combination of DM and RM may place a constraint on magnetic fields under ideal situations. As in Eq. (9), one may decompose the observed RM to several terms

$$RM = RM_{ion} + RM_{MW} + RM_{IGM} + \frac{RM_{host} + RM_{src}}{(1+z)^2}, \quad (198)$$

where RM_{ion} is the contribution from Earth's ionosphere that gives a measurable small contribution and the $(1 + z)^2$ correction factor comes from the $\theta = \lambda^2 RM$ relation, where θ is the polarization angle. In general the observed RM is likely to be dominated by the near-source medium, which is likely a dynamically evolving magnetized environment (Michilli et al., 2018; Luo, Men et al., 2020; Feng et al., 2022; Xu et al., 2022). The observed DM, on the other hand, is dominated by the IGM term. As a result, the RM or DM is not a good probe of the average $B_\parallel$ along the line of sight (unlike pulsars). One can remove the Milky Way and IGM contributions to DM (with the caveat of a large uncertainty in DM_{IGM}) and estimate the average line-of-sight magnetic field in the host and source (most likely in the source region) as

$$B_\parallel^{src} \sim (1.23 \ \mu G)(1+z) \left| \frac{RM_{host,obs} + RM_{src,obs}}{DM_{host,obs} + DM_{src,obs}} \right|, \quad (199)$$

with the observed RM as a proxy of the numerator. The derived $\langle B_\parallel \rangle$ values for FRBs are on average consistent with those of pulsars and magnetars observed in the Milky Way (W.-Y. Wang et al., 2020), with the exception of rFRB 20121102A, which has a much higher value (Hilmarsson et al., 2021).

Another way of estimating $B_\parallel$ near the FRB source is to make use of the observed variations of the DM and RM, i.e.,

$$B_\parallel^{src} \sim (1.23 \ \mu G)(1+z) \left| \frac{\Delta RM}{\Delta DM} \right|. \quad (200)$$

Equation (200) assumed that the variation of $B_\parallel$ is not the dominant factor for RM variations. For rFRB 20201124A, the detection of significant ΔRM and the nondetection of ΔDM led to a constraint of $B_\parallel^{src} > 0.2$ mG (Xu et al., 2022). Some repeating FRBs (such as rFRB 20190520B) show significant RM reversals, suggesting the reversal of the magnetic field directions. In such cases, one has (Yang, Xu, and Zhang, 2022)

$$\frac{\Delta RM}{RM} \simeq \frac{\Delta DM}{DM} + \frac{\Delta B_\parallel}{B_\parallel}. \qquad (201)$$

Since both $\delta RM/RM$ and $\delta B_\parallel/B_\parallel$ are of the order of unity, the value of $B_\parallel$ cannot be constrained.

If the RM contribution from the host and source is small or its behavior can be well quantified for a large FRB sample, one may combine the observed DM and RM information to make a constraint on the poorly known IGM magnetic field. Hackstein et al. (2019) showed that fewer than 100 FRBs from magnetars in a stellar-wind environment hosted by starburst dwarf galaxies at $z \gtrsim 0.5$ would be able to differentiate among different IGM magnetic field models. Recent observations of more complicated FRB surrounding medium in terms of RM variations (Michilli et al., 2018; Luo, Men et al., 2020; Xu et al., 2022) and RM scatter (Feng et al., 2022) make it difficult to correct for the dominant RM contribution from the near-source region, rendering constraint of the IGM magnetic fields much more challenging.

I. Additional probes with gravitationally lensed FRBs: H_0, Ω_k, and dark matter

The high event rate of FRBs makes it likely that gravitationally lensed FRBs will be detected in the future. These lensed sources, especially the lensed repeating sources, offer new opportunities to probe cosmology using FRBs. Thanks to their short durations, the time delays between the images can be measured with an unprecedented precision. Since the gravitational lensing geometry involves the measurements of the angular diameter distances of the source and lens, which depend on the Hubble constant H_0 through z and the curvature of the Universe Ω_k, lensed FRBs can be used to directly measure H_0 and Ω_k (Z.-X. Li et al., 2018). Simulations showed that with about ten lensed repeating FRB systems H_0 can be measured to a subpercent precision level, and Ω_k can be measured to a precision of ~ 0.076 in a model-independent manner (Z.-X. Li et al., 2018).

FRBs can be microlensed by massive compact halo objects (MACHOs), which have been proposed as one type of contributor to dark matter. For $M_{MACHO} \gtrsim 20 M_\odot$, the delay time would be longer than 1 ms. If such lensed events are observed, one FRB with a single pulse would be observed as a double-pulse (lensed by one MACHO object) or triple-pulse burst (lensed by a MACHO binary). The nondetection of these events would place an upper limit on the abundance of these MACHOs (Muñoz et al., 2016; Wang and Wang, 2018; Laha, 2020). As a type of MACHO, the abundance of primordial black holes is already loosely constrained using the CHIME catalog database (H. Zhou et al., 2022). The constraints will be further improved as the FRB sample continues to grow.

A search for lensed FRBs was carried out with the first CHIME/FRB catalog with no detection (Kader et al., 2022). This posed a novel constraint on the abundance of primordial black holes (Leung et al., 2022). Connor and Ravi (2022) forecasted the detection rates of gravitational lensing of FRBs with delay timescales ranging from microseconds to years, corresponding to a wide range of the lens mass spanning 15 orders of magnitude.

J. Neutron star equation of state

The equation of state (EOS) close to or at the nuclear density is still poorly constrained. This leaves a large uncertainty in the neutron star (or even quark star) EOS (Lattimer and Prakash, 2007; A. Li et al., 2020). Some FRB observations may offer clues to the unknown EOS. For example, if the suggested GW190425–FRB 20190425A association is real, the production of FRB 20190425A will demand a relatively large neutron star maximum mass (M_{TOV}), which would eliminate some EOSs (Moroianu et al., 2022). As another example, if FRB bursts carry information of NS crustal oscillations, with a large enough sample one may offer a constraint on the neutron star EOS based on FRB burst morphology (Wadiasingh and Chirenti, 2020).

K. Fundamental physics: Weak equivalence principle, photon mass, and Lorentz invariance violation

Thanks to their short durations, FRBs have also been suggested as probes for fundamental physics because of the lack of spreading in time relative to the predictions of some theories. The first test is Einstein's weak equivalence principle (WEP), which states that all pointlike structureless particles fall along the same path within a gravitational field. This is the foundation of the general theory of relativity, a geometric description of gravitation. According to this principle, photons with different energies from the same source should travel along the same trajectory with the same speed to reach the observer. In the parametrized post-Newtonian (PPN) description, the deviation from the WEP is the PPN parameter γ deviating from 1. FRBs cannot be used to directly constrain γ but can be used to test the difference of γ values between two frequencies ν_1 and ν_2, which are usually the boundaries of the detection frequency band (Wei et al., 2015). Thanks to their large distances and short durations, one can constrain $\Delta\gamma$ with FRBs to be as small as $10^{-15} - 10^{-20}$ (Wei et al., 2015; Tingay and Kaplan, 2016; Xing et al., 2019; Hashimoto et al., 2021).

Another interesting constraint that FRBs can offer is the photon mass (Bonetti et al., 2016; Wu et al., 2016). If photons indeed have a nonzero rest mass, the lower-frequency photons (with a lower "Lorentz factor") should travel slightly slower than higher-frequency photons. The duration of an FRB therefore presents an absolute maximum delay due to such an effect. With a more sophisticated method, by combining the nonzero photon mass delay and the plasma dispersion delay (it turns out that the two dispersion relations have similar forms with different normalization factors and slightly different z dependences), a more stringent constraint can be reached with FRBs of known redshifts, especially with a sample of z-known FRBs using a Bayesian approach (Shao and Zhang, 2017). The most stringent upper limit of the photon mass posed by FRBs has already reached $m_\gamma \lesssim 5 \times 10^{-48}$ g (Bonetti et al., 2016; Wu et al., 2016; Shao and Zhang, 2017; Xing et al., 2019).

Another widely discussed fundamental physics constraint is Lorentz invariance violation due to the delay of high-energy photons as they travel through foamlike space at small scales. The effect is most significant at high energies,

so short-duration GRBs are much more suitable for posing meaningful constraints than FRBs, which have low photon energies.

X. PROBLEMS AND PROSPECTS

The rapid progress being made in the FRB field is accompanied by many open questions that continue to drive the field forward. I now discuss the three most pressing current questions.

A. Do all FRBs repeat?

This question is interesting from both observational and theoretical aspects. Observationally, it is much more difficult to prove that an FRB does not repeat than that it does. If one has not detected a repeated burst from the source yet, it could well be that (1) it repeated but the telescope has missed it; (2) it repeated, but the burst is below the telescope sensitivity; or (3) it simply has not repeated and the waiting time is longer than the observing time. If one adopts the two sub-bursts of FRB 20200428 from the Galactic magnetar SGR 1935+2154 (Andersen et al., 2020; Bochenek et al., 2020) as one burst, then the source may not yet be regarded as a repeating FRB source (many repeated radio bursts from the source are not bright enough to be detected as FRBs at cosmological distances), even though one is certain that it should be an FRB repeater because the magnetar source itself did not show significant differences before and after the FRB and there is no reason why the physical conditions to make FRB 20200428 would not be satisfied again to make another one. Theoretically this question is interesting because it is related to whether any of the cataclysmic FRB models are relevant.

There have been substantial efforts to address this question. (1) From the observational side, although repeater bursts are found to display some interesting characteristics [such as longer duration, down-drifting subpulses, and narrower spectra (Andersen et al., 2019)], there is still no definitive clue to suggest that apparent nonrepeaters are indeed different. (2) Machine-learning methods have been proposed to differentiate between repeaters and nonrepeaters (B. H. Chen et al., 2022; Luo, Zhu-Ge, and Zhang, 2023; Zhu-Ge, Luo, and Zhang, 2023), and the results seem to suggest that most apparently nonrepeating FRBs are indeed different from the repeating bursts. (3) A statistical study of the observational properties of repeaters and apparent nonrepeaters suggested that there might be two populations (Zhong et al., 2022). (4) With limited data in the pre-CHIME era, arguments have been made that rFRB 20121102A is much more active than any other nonrepeaters (Palaniswamy, Li, and Zhang, 2018; Caleb et al., 2019), so there might be two distinct classes (or at least two classes of repeaters with distinct activity levels). These arguments need to be revisited with the uniform, much larger database from CHIME. (5) One interesting test is to study the observed fraction of repeating sources from all FRBs $F_{r,obs}$. Ai, Gao, and Zhang (2021) showed that if there indeed are nonrepeaters and if repeaters repeat forever, $F_{r,obs}$ should approach a maximum after a certain observing time (when most repeaters are discovered) and then decline with time afterward. However, uncertainties in the repetition rate and its distribution in repeaters make this criterion not clean. In some cases, the required time to reach the maximum is longer than the astronomers' timescale (for instance, longer than 1000 yr). When the lifetime of the repeaters is considered, there is essentially no achievable maximum within the astronomers' timescale. In any case, continuously monitoring $F_{r,obs}$ may provide important clues to address this open question. The long-term CHIME observations seem to suggest a constant $F_{r,obs}$ over time (Andersen et al., 2023b), which may suggest the existence of nonrepeating FRBs.

In the long term, besides refining the previously mentioned analyses with a much larger dataset, a detection of an FRB robustly associated with a cataclysmic event (such as a gravitational wave event) would offer strong support to the existence of these special types of FRBs. The plausible GW190425–FRB 20190425A association (Moroianu et al., 2022) might be the first such case. Based on the event rate density arguments, these FRBs must be only a small fraction of all FRBs and may have some special properties. Another caveat is for individual cases, the robustness of the association must be addressed through various (for instance, temporal, spatial, and distance) chance coincidence probabilities as well as theoretical arguments (Moroianu et al., 2022). The new population may be established only after a sample of such association events is detected.

B. Is there more than one class of repeating FRBs?

This question actually has two aspects: First, observationally do we see different clustering properties among the observed repeaters? Second, physically is there more than one type of engine source that powers different repeaters? From the observational side, I would argue that there are already three types: (1) regular active repeaters in the cosmological distances (such as rFRB 20121102A, rFRB 20180916B, rFRB 20190520B, rFRB 20180301A, and rFRB 20201124A), which have not yet been found in the Milky Way Galaxy; (2) less energetic and less active magnetar repeaters such as SGR 1935+2154 that produced two subpulses in FRB 20200428; and (3) the globular cluster FRB 20200120E in M81, which has a high activity level but produces bursts with much lower luminosities than other cosmological active repeaters (Nimmo et al., 2022). Since the central source of the second type has already been identified as a magnetar, the general trend in the community is to attribute all three observationally identified types to magnetars, with different evolutionary stages and probably different formation channels as well. For example, the first type (active cosmological repeaters) might be younger magnetars formed from recent supernova explosions, and the third type may be magnetars produced from older formation channels such as WD-WD and NS-NS mergers or the accretion-induced collapse of WDs. Even though this "magnetars make them all" hypothesis is theoretically attractive and passes some observational constraints, it nonetheless suffers from some drawbacks. For example, the detection of FRB 20200120E from the M81 globular cluster suggests that these systems are common (Kremer, Piro, and Li, 2021; Lu, Beniamini, and Kumar, 2022). This seems to be inconsistent with the fact that none of the 30 discovered magnetars from the Milky Way or Large

Magellanic Cloud or SMC are associated with globular clusters. The fact that the CHIME DM distribution demands a dominant delayed population of FRBs with respect to star formation [see Hashimoto *et al.* (2022), Qiang, Li, and Wei (2022), and Zhang and Zhang (2022), but see Shin *et al.* (2022)] also suggests that if magnetars do it all, the old-population magnetar channel should be significant, in contrast to the known magnetar population data. Thus, the current data may have already suggested the existence of other nonmagnetar FRB engines.

C. FRB radiation mechanisms: Where and how?

Within the magnetar model of FRBs, there are uncertainties regarding the location of the emission region (for instance, magnetospheres versus relativistic shocks) and the radiation mechanism (bunched emission and plasma instabilities versus vacuum maser mechanisms). As discussed in Secs. V.B, V.C, and VI.A, active studies and intense debates exist in the field, and growing evidence suggests that the magnetospheric origin is relevant for at least some FRBs. It remains unclear whether more than one emission site and more than one coherent mechanism is operating in FRBs. Investigations in this direction will continue for years to come and the debates may not be settled in the near future, as the history of the study of the radiation mechanism of radio pulsars has suggested.

D. Prospects

In a young and rapidly growing field, it is enjoyable to make predictions. Petroff, Hessels, and Lorimer (2019), made their respective predictions about the field within 5 yr of the original review and also in their later updated paper (Petroff, Hessels, and Lorimer, 2022). Even though some of the predictions were realized, some unpredicted, surprising discoveries were made in a less than 3-yr period after the first predictions were made. These include a periodically modulated FRB (rFRB 20180916B) with a 16-d period, a megajansky low-luminosity FRB (FRB 20200428) from a Galactic magnetar, and a repeating low-luminosity FRB (rFRB 20200120E) from a globular cluster in M81. The FRB field seems to discourage conservative predictions. I close this review with ten predictions for the next 5–10 yr.

1. The detected FRB number will continue to grow rapidly, reaching $\sim 10^4$ different sources (including both nonrepeating and repeating FRB populations) from survey programs such as the CHIME/FRB project and reaching $\sim 10^4$ bursts from a few active individual sources from dedicated observational campaigns such as the FAST FRB Key Project.
2. The FRB community will continue to grow and the number of papers and citations per year will keep rising for another 5–10 yr.
3. Surprises will continue to occur and will shake the FRB theoretical framework a few times before a standard paradigm is established.
4. X-ray counterparts of FRBs from nearby galaxies will be discovered, which are consistent with an SGR origin of FRBs.
5. Despite active searches, prompt optical flashes coinciding with FRBs will not be discovered, because of the intrinsic faintness of the prompt optical emission.
6. Claims about the associations between a progenitor of a magnetar (such as a long GRB, a superluminous supernova, a short GRB, or a regular type II supernova) and a repeating FRB source will be made, but a firm association cannot be established, because of the uncertainties in coincidences.
7. More claims about the associations between nonrepeating FRBs and gravitational wave sources will be made, but the sample is not large and consistent enough to draw a definitive conclusion.
8. More Galactic FRBs will be detected, most likely from SGR 1935+2154 or other magnetars, but also possibly from sources other than magnetars, such as the Galactic Center, young or old neutron stars, or even black hole binary systems.
9. Multiple channels of repeating FRBs will be widely accepted. The ansatz that "all FRBs repeat" still cannot be completely ruled out.
10. Debates on the physical mechanisms of FRBs will continue among theorists, not only because "a competent theorist can make any model to match any observational data" but also because there might indeed be several physically plausible mechanisms that operate together.

LIST OF SYMBOLS AND ABBREVIATIONS

AGN	active galactic nucleus
ALAE	amplified linear acceleration emission
ASKAP	Australian Square Kilometre Array Pathfinder
AXP	anomalous x-ray pulsar
BH	black hole
CBC	compact binary coalescence
cCBC	charged compact binary coalescence
CETI	communicative extraterrestrial intelligence
CGM	circumgalactic medium
CHIME	Canadian Hydrogen Intensity Mapping Experiment
CM	conversion measure
CMB	cosmic microwave background
DM	dispersion measure
DSR	Dicke superradiance
EM	emission measure or electromagnetic
FAST	Five-Hundred-Meter Aperture Spherical Telescope
FEL	free-electron laser
FRB	fast radio burst
GJ	Goldreich-Julian

GP	giant pulse
GRB	gamma-ray burst
GW	gravitational wave
ICS	inverse Compton scattering
IGM	intergalactic medium
ISM	interstellar medium
L mode	left mode
LGRB	long-duration gamma-ray burst
LSD	large superconducting dipole
MACHO	massive compact halo object
MW	Milky Way
MWN(e)	magnetar wind nebula(-ae)
O mode	ordinary mode
PA	polarization angle
PIC	particle in cell
PPN	parametrized post-Newtonian
PRS	persistent radio source
PWN(e)	pulsar wind nebula(-ae)
NS	neutron star
R mode	right mode
RFI	radio frequency interference
rFRB	repeating fast radio burst
RM	rotation measure
SGR	soft gamma-ray repeater
SGRB	short gamma-ray burst
SLSN(e)	superluminous supernova(-ae)
SM	scattering measure
SMBH	supermassive black hole
SMC	Small Magellanic Cloud
SMNS	supramassive neutron star
SN(e)	supernova(-ae)
SNR	supernova remnant
STARE2	Survey for Transient Astronomical Radio Emission 2
ULX	ultraluminous x ray
WD	white dwarf
WEP	weak equivalence principle
X mode	extraordinary mode
XRB	x-ray burst

REFERENCES

Abbott, R., *et al.* (LIGO Scientific, Virgo, KAGRA, and CHIME/FRB Collaborations), 2022, arXiv:2203.12038.

Abramowicz, M. A., M. Bejger, and M. Wielgus, 2018, Astrophys. J. **868**, 17.

Ade, P. A. R., *et al.* (Planck Collaboration), 2016, Astron. Astrophys. **594**, A13.

Aghanim, N., *et al.* (Planck Collaboration), 2020, Astron. Astrophys. **641**, A6.

Ai, S., H. Gao, and B. Zhang, 2021, Astrophys. J. **906**, L5.

Alcock, C., E. Farhi, and A. Olinto, 1986, Astrophys. J. **310**, 261.

Amaro-Seoane, P., *et al.*, 2017, arXiv:1702.00786.

Amiri, M., *et al.* (CHIME/FRB Collaboration), 2021, Astrophys. J. **257**, 59.

Amiri, M., *et al.* (CHIME/FRB Collaboration), 2019, Nature (London) **566**, 235.

Amiri, M., *et al.* (CHIME/FRB Collaboration), 2020, arXiv:2001.10275.

Andersen, B. C., *et al.* (CHIME/FRB Collaboration), 2019, Astrophys. J. **885**, L24.

Andersen, B. C., *et al.* (CHIME/FRB Collaboration), 2020, Nature (London) **587**, 54.

Andersen, B. C., *et al.* (CHIME/FRB Collaboration), 2022, Nature (London) **607**, 256.

Andersen, B. C., *et al.* (CHIME/FRB Collaboration), 2023a, arXiv:2301.08762.

Andersen, B. C., *et al.* (CHIME/FRB Collaboration), 2023b, Astrophys. J. **947**, 83.

Anna-Thomas, R., *et al.*, 2023, Science **380**, 599.

Arons, J., and E. T. Scharlemann, 1979, Astrophys. J. **231**, 854.

Babul, A.-N., and L. Sironi, 2020, Mon. Not. R. Astron. Soc. **499**, 2884.

Bagchi, M., 2017, Astrophys. J. **838**, L16.

Bailes, M., 2022, Science **378**, abj3043.

Bannister, K. W., T. Murphy, B. M. Gaensler, and J. E. Reynolds, 2012, Astrophys. J. **757**, 38.

Bannister, K. W., *et al.*, 2017, Astrophys. J. **841**, L12.

Bannister, K. W., *et al.*, 2019, Science **365**, 565.

Barrau, A., F. Moulin, and K. Martineau, 2018, Phys. Rev. D **97**, 066019.

Barrau, A., C. Rovelli, and F. Vidotto, 2014, Phys. Rev. D **90**, 127503.

Beloborodov, A. M., 2009, Astrophys. J. **703**, 1044.

Beloborodov, A. M., 2017, Astrophys. J. **843**, L26.

Beloborodov, A. M., 2020, Astrophys. J. **896**, 142.

Beloborodov, A. M., 2021a, Astrophys. J. **922**, L7.

Beloborodov, A. M., 2021b, arXiv:2108.05464.

Beloborodov, A. M., and C. Thompson, 2007, Astrophys. J. **657**, 967.

Benford, G., and J. C. Weatherall, 1992, Phys. Fluids B **4**, 4111.

Beniamini, P., and P. Kumar, 2020, Mon. Not. R. Astron. Soc. **498**, 651.

Beniamini, P., and P. Kumar, 2022, arXiv:2211.07669.

Beniamini, P., P. Kumar, X. Ma, and E. Quataert, 2021, Mon. Not. R. Astron. Soc. **502**, 5134.

Beniamini, P., P. Kumar, and R. Narayan, 2022, Mon. Not. R. Astron. Soc. **510**, 4654.

Beniamini, P., Z. Wadiasingh, and B. D. Metzger, 2020, Mon. Not. R. Astron. Soc. **496**, 3390.

Bhandari, S., and C. Flynn, 2021, Universe **7**, 85.

Bhandari, S., et al., 2020, Astrophys. J. **895**, L37.

Bhandari, S., et al., 2022, Astron. J. **163**, 69.

Bhardwaj, M., et al., 2021, Astrophys. J. **910**, L18.

Bhattacharya, M., P. Kumar, and E. V. Linder, 2021, Phys. Rev. D **103**, 103526.

Bochenek, C. D., V. Ravi, K. V. Belov, G. Hallinan, J. Kocz, S. R. Kulkarni, and D. L. McKenna, 2020, Nature (London) **587**, 59.

Bochenek, C. D., V. Ravi, and D. Dong, 2021, Astrophys. J. **907**, L31.

Boesgaard, A. M., and G. Steigman, 1985, Annu. Rev. Astron. Astrophys. **23**, 319.

Bonetti, L., J. Ellis, N. E. Mavromatos, A. S. Sakharov, E. K. Sarkisyan-Grinbaum, and A. D. A. M. Spallicci, 2016, Phys. Lett. B **757**, 548.

Bouwhuis, M., K. W. Bannister, J.-P. Macquart, R. M. Shannon, D. L. Kaplan, J. D. Bunton, B. S. Koribalski, and M. T. Whiting, 2020, Mon. Not. R. Astron. Soc. **497**, 125.

Boyd, T. J. M., and J. J. Sanderson, 2003, *The Physics of Plasmas* (Cambridge University Press, Cambridge, England).

Brandenberger, R., B. Cyr, and A. Varna Iyer, 2017, arXiv:1707.02397.

Burke-Spolaor, S., M. Bailes, R. Ekers, J.-P. Macquart, and I. Crawford, Fronefield, 2011, Astrophys. J. **727**, 18.

Cai, Y.-F., E. Sabancilar, D. A. Steer, and T. Vachaspati, 2012, Phys. Rev. D **86**, 043521.

Cai, Y.-F., E. Sabancilar, and T. Vachaspati, 2012, Phys. Rev. D **85**, 023530.

Caleb, M., C. Flynn, and B. W. Stappers, 2019, Mon. Not. R. Astron. Soc. **485**, 2281.

Caleb, M., B. W. Stappers, K. Rajwade, and C. Flynn, 2019, Mon. Not. R. Astron. Soc. **484**, 5500.

Caleb, M., et al., 2018, Mon. Not. R. Astron. Soc. **478**, 2046.

Camilo, F., et al., 2007, Astrophys. J. **663**, 497.

Champion, D. J., et al., 2016, Mon. Not. R. Astron. Soc. **460**, L30.

Chatterjee, S., et al., 2017, Nature (London) **541**, 58.

Chen, A. Y., and A. M. Beloborodov, 2017, Astrophys. J. **844**, 133.

Chen, A. Y., Y. Yuan, A. M. Beloborodov, and X. Li, 2022, Astrophys. J. **929**, 31.

Chen, B. H., T. Hashimoto, T. Goto, S. J. Kim, D. J. D. Santos, A. Y. L. On, T.-Y. Lu, and T. Y. Y. Hsiao, 2022, Mon. Not. R. Astron. Soc. **509**, 1227.

Chen, C. J., and B. Zhang, 2023, Mon. Not. R. Astron. Soc. **519**, 6284.

Cheng, K. S., C. Ho, and M. Ruderman, 1986, Astrophys. J. **300**, 522.

Chevalier, R. A., and Z.-Y. Li, 1999, Astrophys. J. **520**, L29.

Cho, H., et al., 2020, Astrophys. J. **891**, L38.

Clegg, A. W., A. L. Fey, and T. J. W. Lazio, 1998, Astrophys. J. **496**, 253.

Colpi, M., U. Geppert, and D. Page, 2000, Astrophys. J. **529**, L29.

Connor, L., and V. Ravi, 2022, arXiv:2206.14310.

Connor, L., J. Sievers, and U.-L. Pen, 2016, Mon. Not. R. Astron. Soc. **458**, L19.

Contopoulos, I., D. Kazanas, and C. Fendt, 1999, Astrophys. J. **511**, 351.

Cooper, A. J., O. Gupta, Z. Wadiasingh, R. A. M. J. Wijers, O. M. Boersma, I. Andreoni, A. Rowlinson, and K. Gourdji, 2022, arXiv:2210.17205.

Cooper, A. J., and R. A. M. J. Wijers, 2021, Mon. Not. R. Astron. Soc. **508**, L32.

Cordes, J. M., and S. Chatterjee, 2019, Annu. Rev. Astron. Astrophys. **57**, 417.

Cordes, J. M., and T. J. W. Lazio, 2002, arXiv:astro-ph/0207156.

Cordes, J. M., and M. A. McLaughlin, 2003, Astrophys. J. **596**, 1142.

Cordes, J. M., S. K. Ocker, and S. Chatterjee, 2021, arXiv:2108.01172.

Cordes, J. M., and I. Wasserman, 2016, Mon. Not. R. Astron. Soc. **457**, 232.

Cordes, J. M., I. Wasserman, J. W. T. Hessels, T. J. W. Lazio, S. Chatterjee, and R. S. Wharton, 2017, Astrophys. J. **842**, 35.

Cordes, J. M., J. M. Weisberg, and V. Boriakoff, 1985, Astrophys. J. **288**, 221.

Cordes, J. M., R. S. Wharton, L. G. Spitler, S. Chatterjee, and I. Wasserman, 2016, arXiv:1605.05890.

Cruces, M., L. G. Spitler, P. Scholz, R. Lynch, A. Seymour, J. W. T. Hessels, C. Gouiffés, G. H. Hilmarsson, M. Kramer, and S. Munjal, 2021, Mon. Not. R. Astron. Soc. **500**, 448.

Cunningham, V., et al., 2019, Astrophys. J. **879**, 40.

Dai, L., and W. Lu, 2017, Astrophys. J. **847**, 19.

Dai, S., et al., 2021, Astrophys. J. **920**, 46.

Dai, S., et al., 2022, arXiv:2203.08151.

Dai, Z. G., 2019, Astrophys. J. **873**, L13.

Dai, Z. G., 2020, Astrophys. J. **897**, L40.

Dai, Z. G., J. S. Wang, X. F. Wu, and Y. F. Huang, 2016, Astrophys. J. **829**, 27.

Dai, Z. G., J. S. Wang, and Y. W. Yu, 2017, Astrophys. J. **838**, L7.

Dai, Z. G., and S. Q. Zhong, 2020, Astrophys. J. **895**, L1.

Daugherty, J. K., and A. K. Harding, 1996, Astrophys. J. **458**, 278.

Day, C. K., et al., 2020, Mon. Not. R. Astron. Soc. **497**, 3335.

Dehman, C., D. Viganò, N. Rea, J. A. Pons, R. Perna, and A. Garcia-Garcia, 2020, Astrophys. J. **902**, L32.

DeLaunay, J. J., D. B. Fox, K. Murase, P. Mészáros, A. Keivani, C. Messick, M. A. Mostafá, F. Oikonomou, G. Tešić, and C. F. Turley, 2016, Astrophys. J. **832**, L1.

Deng, C.-M., Y. Cai, X.-F. Wu, and E.-W. Liang, 2018, Phys. Rev. D **98**, 123016.

Deng, W., and B. Zhang, 2014, Astrophys. J. **783**, L35.

Dicke, R. H., 1954, Phys. Rev. **93**, 99.

Dolag, K., B. M. Gaensler, A. M. Beck, and M. C. Beck, 2015, Mon. Not. R. Astron. Soc. **451**, 4277.

Draine, B. T., 2011, *Physics of the Interstellar and Intergalactic Medium*, Princeton Series in Astrophysics Vol. 19 (Princeton University Press, Princeton, NJ).

Duncan, R. C., and C. Thompson, 1992, Astrophys. J. **392**, L9.

Egorov, A. E., and K. A. Postnov, 2009, Astron. Lett. **35**, 241.

Er, X., Y.-P. Yang, and A. Rogers, 2020, Astrophys. J. **889**, 158.

Falcke, H., and L. Rezzolla, 2014, Astron. Astrophys. **562**, A137.

Fan, X., C. L. Carilli, and B. Keating, 2006, Annu. Rev. Astron. Astrophys. **44**, 415.

Feng, Y., et al., 2022, Science **375**, 1266.

Fong, W.-f., et al., 2021, Astrophys. J. **919**, L23.

Fukugita, M., C. J. Hogan, and P. J. E. Peebles, 1998, Astrophys. J. **503**, 518.

Fung, P. K., and J. Kuijpers, 2004, Astron. Astrophys. **422**, 817.

Gajjar, V., et al., 2018, Astrophys. J. **863**, 2.

Gao, H., Z. Li, and B. Zhang, 2014, Astrophys. J. **788**, 189.

Gao, H., B. Zhang, and H.-J. Lü, 2016, Phys. Rev. D **93**, 044065.

Geng, J., B. Li, and Y. Huang, 2021, Innovation **2**, 100152.

Geng, J. J., and Y. F. Huang, 2015, Astrophys. J. **809**, 24.

Ghisellini, G., 2017, Mon. Not. R. Astron. Soc. **465**, L30.

Ghisellini, G., and N. Locatelli, 2018, Astron. Astrophys. **613**, A61.

Ghisellini, G., and R. Svensson, 1991, Mon. Not. R. Astron. Soc. **252**, 313.

Gil, J., Y. Lyubarsky, and G. I. Melikidze, 2004, Astrophys. J. **600**, 872.

Goldreich, P., and W. H. Julian, 1969, Astrophys. J. **157**, 869.

Gourgouliatos, K. N., and D. Lynden-Bell, 2019, Mon. Not. R. Astron. Soc. **482**, 1942.

Gruzinov, A., 2019, arXiv:1912.08150.

Gruzinov, A., and Y. Levin, 2019, Astrophys. J. **876**, 74.

Gu, W.-M., Y.-Z. Dong, T. Liu, R. Ma, and J. Wang, 2016, Astrophys. J. **823**, L28.

Gu, W.-M., T. Yi, and T. Liu, 2020, Mon. Not. R. Astron. Soc. **497**, 1543.

Guidorzi, C., et al., 2020, Astron. Astrophys. **642**, A160.

Gupta, P. D., and N. Saini, 2018, J. Astrophys. Astron. **39**, 14.

Hackstein, S., M. Brüggen, F. Vazza, B. M. Gaensler, and V. Heesen, 2019, Mon. Not. R. Astron. Soc. **488**, 4220.

Hankins, T. H., and J. A. Eilek, 2007, Astrophys. J. **670**, 693.

Hansen, B. M. S., and M. Lyutikov, 2001, Mon. Not. R. Astron. Soc. **322**, 695.

Harding, A. K., and A. G. Muslimov, 1998, Astrophys. J. **508**, 328.

Hashimoto, T., T. Goto, A. Y. L. On, T.-Y. Lu, D. J. D. Santos, S. C. C. Ho, S. J. Kim, T.-W. Wang, and T. Y. Y. Hsiao, 2020, Mon. Not. R. Astron. Soc. **498**, 3927.

Hashimoto, T., T. Goto, D. J. D. Santos, S. C. C. Ho, T. Y. Y. Hsiao, Y. H. V. Wong, A. Y. L. On, S. J. Kim, T.-Y. Lu, and E. Kilerci-Eser, 2021, Phys. Rev. D **104**, 124026.

Hashimoto, T., et al., 2022, Mon. Not. R. Astron. Soc. **511**, 1961.

Hawking, S. W., 1974, Nature (London) **248**, 30.

Heintz, K. E., et al., 2020, Astrophys. J. **903**, 152.

Hessels, J. W. T., et al., 2019, Astrophys. J. **876**, L23.

Hewitt, D. M., et al., 2022, Mon. Not. R. Astron. Soc. **515**, 3577.

Hibschman, J. A., and J. Arons, 2001, Astrophys. J. **560**, 871.

Hilmarsson, G. H., et al., 2021, Astrophys. J. **908**, L10.

Hiramatsu, D., E. Berger, B. D. Metzger, S. Gomez, A. Bieryla, I. Arcavi, D. A. Howell, R. Mckinven, and N. Tominaga, 2022, arXiv:2211.03974.

Houde, M., A. Mathews, and F. Rajabi, 2018, Mon. Not. R. Astron. Soc. **475**, 514.

Houde, M., F. Rajabi, B. M. Gaensler, A. Mathews, and V. Tranchant, 2019, Mon. Not. R. Astron. Soc. **482**, 5492.

Huang, L., and R. V. Shcherbakov, 2011, Mon. Not. R. Astron. Soc. **416**, 2574.

Inoue, S., 2004, Mon. Not. R. Astron. Soc. **348**, 999.

Ioka, K., 2003, Astrophys. J. **598**, L79.

Ioka, K., 2020, Astrophys. J. **904**, L15.

Ioka, K., and B. Zhang, 2020, Astrophys. J. **893**, L26.

Iwazaki, A., 2015, Phys. Rev. D **91**, 023008.

Iwazaki, A., 2021, Phys. Rev. D **104**, 043022.

James, C. W., J. X. Prochaska, J. P. Macquart, F. O. North-Hickey, K. W. Bannister, and A. Dunning, 2022, Mon. Not. R. Astron. Soc. **510**, L18.

Jaroszynski, M., 2019, Mon. Not. R. Astron. Soc. **484**, 1637.

Jiang, J.-C., et al., 2022, Res. Astron. Astrophys. **22**, 124003.

Kader, Z., et al. (CHIME/FRB Collaboration), 2022, Phys. Rev. D **106**, 043016.

Kalapotharakos, C., G. Brambilla, A. Timokhin, A. K. Harding, and D. Kazanas, 2018, Astrophys. J. **857**, 44.

Kalapotharakos, C., A. K. Harding, and D. Kazanas, 2014, Astrophys. J. **793**, 97.

Karastergiou, A., et al., 2015, Mon. Not. R. Astron. Soc. **452**, 1254.

Kasen, D., and L. Bildsten, 2010, Astrophys. J. **717**, 245.

Kashiyama, K., K. Ioka, and P. Mészáros, 2013, Astrophys. J. **776**, L39.

Kashiyama, K., and K. Murase, 2017, Astrophys. J. **839**, L3.

Kaspi, V. M., and A. M. Beloborodov, 2017, Annu. Rev. Astron. Astrophys. **55**, 261.

Katz, J. I., 1982, Astrophys. J. **260**, 371.

Katz, J. I., 2014, Phys. Rev. D **89**, 103009.

Katz, J. I., 2016, Astrophys. J. **826**, 226.

Katz, J. I., 2017a, Mon. Not. R. Astron. Soc. **469**, L39.

Katz, J. I., 2017b, Mon. Not. R. Astron. Soc. **471**, L92.

Katz, J. I., 2018a, Mon. Not. R. Astron. Soc. **481**, 2946.

Katz, J. I., 2018b, Prog. Part. Nucl. Phys. **103**, 1.

Katz, J. I., 2019, Mon. Not. R. Astron. Soc. **487**, 491.

Katz, J. I., 2020a, Mon. Not. R. Astron. Soc. **494**, L64.

Katz, J. I., 2020b, Mon. Not. R. Astron. Soc. **499**, 2319.

Katz, J. I., 2022a, Mon. Not. R. Astron. Soc. **516**, L58.

Katz, J. I., 2022b, Mon. Not. R. Astron. Soc. **513**, 1925.

Keane, E. F., B. W. Stappers, M. Kramer, and A. G. Lyne, 2012, Mon. Not. R. Astron. Soc. **425**, L71.

Keane, E. F., et al., 2016, Nature (London) **530**, 453.

Kellermann, K. I., and I. I. K. Pauliny-Toth, 1969, Astrophys. J. **155**, L71.

Kelly, B. J., J. G. Baker, Z. B. Etienne, B. Giacomazzo, and J. Schnittman, 2017, Phys. Rev. D **96**, 123003.

Kirsten, F., M. P. Snelders, M. Jenkins, K. Nimmo, J. van den Eijnden, J. W. T. Hessels, M. P. Gawroński, and J. Yang, 2021, Nat. Astron. **5**, 414.

Kirsten, F., et al., 2022, Nature (London) **602**, 585.

Kompaneets, A. S., 1957, J. Exp. Theor. Phys. **4**, 730, https://ui.adsabs.harvard.edu/abs/1957JETP....4..730K/abstract.

Kramer, M., and I. H. Stairs, 2008, Annu. Rev. Astron. Astrophys. **46**, 541.

Kremer, K., A. L. Piro, and D. Li, 2021, Astrophys. J. **917**, L11.

Kulkarni, S. R., 2020, arXiv:2007.02886.

Kulkarni, S. R., E. O. Ofek, J. D. Neill, Z. Zheng, and M. Juric, 2014, Astrophys. J. **797**, 70.

Kulsrud, R. M., 2005, Plasma Physics for Astrophysics, Princeton Series in Astrophysics Vol. 66 (Princeton University Press, Princeton, NJ).

Kumar, P., and Ž. Bošnjak, 2020, Mon. Not. R. Astron. Soc. **494**, 2385.

Kumar, P., R. Gill, and W. Lu, 2022, Mon. Not. R. Astron. Soc. **516**, 2697.

Kumar, P., and E. V. Linder, 2019, Phys. Rev. D **100**, 083533.

Kumar, P., and W. Lu, 2020, Mon. Not. R. Astron. Soc. **494**, 1217.

Kumar, P., W. Lu, and M. Bhattacharya, 2017, Mon. Not. R. Astron. Soc. **468**, 2726.

Kumar, P., R. M. Shannon, M. E. Lower, S. Bhandari, A. T. Deller, C. Flynn, and E. F. Keane, 2022, Mon. Not. R. Astron. Soc. **512**, 3400.

Kumar, P., and B. Zhang, 2015, Phys. Rep. **561**, 1.

Kumar, P., *et al.*, 2019, Astrophys. J. **887**, L30.

Kundu, E., and B. Zhang, 2021, Mon. Not. R. Astron. Soc. **508**, L48.

Laha, R., 2020, Phys. Rev. D **102**, 023016.

Laha, S., *et al.*, 2022a, arXiv:2203.07489.

Laha, S., *et al.*, 2022b, arXiv:2203.07465.

Lai, D., 2012, Astrophys. J. **757**, L3.

Lasky, P. D., B. Haskell, V. Ravi, E. J. Howell, and D. M. Coward, 2014, Phys. Rev. D **89**, 047302.

Lattimer, J. M., and M. Prakash, 2007, Phys. Rep. **442**, 109.

Law, C. J., *et al.*, 2017, Astrophys. J. **850**, 76.

Law, C. J., *et al.*, 2019, Astrophys. J. **886**, 24.

Law, C. J., *et al.*, 2020, Astrophys. J. **899**, 161.

Leung, C., *et al.*, 2022, Phys. Rev. D **106**, 043017.

Levin, J., D. J. D'Orazio, and S. Garcia-Saenz, 2018, Phys. Rev. D **98**, 123002.

Levin, Y., A. M. Beloborodov, and A. Bransgrove, 2020, arXiv:2002.04595.

Levin, Y., and M. Lyutikov, 2012, Mon. Not. R. Astron. Soc. **427**, 1574.

Li, A., Z. Y. Zhu, E. P. Zhou, J. M. Dong, J. N. Hu, and C. J. Xia, 2020, J. High Energy Astrophys. **28**, 19.

Li, C., and L. Li, 2014, Sci. China Phys. Mech. Astron. **57**, 1390.

Li, C. K., *et al.*, 2021, Nat. Astron. **5**, 378.

Li, D., and J. J. Zanazzi, 2021, Astrophys. J. **909**, L25.

Li, D., *et al.*, 2021, Nature (London) **598**, 267.

Li, D.-Z., K. J. Lee, Y.-P. Yang, W. Y. Wang, and B. Zhang, 2023 (to be published).

Li, L., Q.-C. Li, S.-Q. Zhong, J. Xia, L. Xie, F.-Y. Wang, and Z.-G. Dai, 2022, Astrophys. J. **929**, 139.

Li, L.-B., Y.-F. Huang, J.-J. Geng, and B. Li, 2018, Res. Astron. Astrophys. **18**, 061.

Li, Q.-C., Y.-P. Yang, and Z.-G. Dai, 2020, Astrophys. J. **896**, 71.

Li, Q.-C., Y.-P. Yang, F. Y. Wang, K. Xu, Y. Shao, Z.-N. Liu, and Z.-G. Dai, 2021, Astrophys. J. **918**, L5.

Li, Y., and B. Zhang, 2020, Astrophys. J. **899**, L6.

Li, Y., B. Zhang, K. Nagamine, and J. Shi, 2019, Astrophys. J. **884**, L26.

Li, Z., H. Gao, J. J. Wei, Y. P. Yang, B. Zhang, and Z. H. Zhu, 2020, Mon. Not. R. Astron. Soc. **496**, L28.

Li, Z.-X., H. Gao, X.-H. Ding, G.-J. Wang, and B. Zhang, 2018, Nat. Commun. **9**, 3833.

Li, Z.-Y., T. Chiueh, and M. C. Begelman, 1992, Astrophys. J. **394**, 459.

Liebling, S. L., and C. Palenzuela, 2016, Phys. Rev. D **94**, 064046.

Lieu, R., 2017, Astrophys. J. **834**, 199.

Lin, L., *et al.*, 2020, Nature (London) **587**, 63.

Lingam, M., and A. Loeb, 2017, Astrophys. J. **837**, L23.

Linscott, I. R., and J. W. Erkes, 1980, Astrophys. J. **236**, L109.

Liu, T., G. E. Romero, M.-L. Liu, and A. Li, 2016, Astrophys. J. **826**, 82.

Loeb, A., Y. Shvartzvald, and D. Maoz, 2014, Mon. Not. R. Astron. Soc. **439**, L46.

Long, K., and A. Pe'er, 2018, Astrophys. J. **864**, L12.

Lorimer, D. R., M. Bailes, M. A. McLaughlin, D. J. Narkevic, and F. Crawford, 2007, Science **318**, 777.

Lorimer, D. R., and M. Kramer, 2012, in *Handbook of Pulsar Astronomy*, edited by D. R. Lorimer and M. Kramer (Cambridge University Press, Cambridge, England).

Lu, W., 2021 (unpublished).

Lu, W., P. Beniamini, and P. Kumar, 2022, Mon. Not. R. Astron. Soc. **510**, 1867.

Lu, W., and P. Kumar, 2018, Mon. Not. R. Astron. Soc. **477**, 2470.

Lu, W., P. Kumar, and R. Narayan, 2019, Mon. Not. R. Astron. Soc. **483**, 359.

Lu, W., P. Kumar, and B. Zhang, 2020, Mon. Not. R. Astron. Soc. **498**, 1397.

Lu, W., and E. S. Phinney, 2020, Mon. Not. R. Astron. Soc. **496**, 3308.

Lu, W., and A. L. Piro, 2019, Astrophys. J. **883**, 40.

Lü, H.-J., B. Zhang, W.-H. Lei, Y. Li, and P. D. Lasky, 2015, Astrophys. J. **805**, 89.

Luan, J., and P. Goldreich, 2014, Astrophys. J. **785**, L26.

Luo, J., *et al.*, 2016, Classical Quantum Gravity **33**, 035010.

Luo, J.-W., J.-M. Zhu-Ge, and B. Zhang, 2023, Mon. Not. R. Astron. Soc. **518**, 1629.

Luo, Q., and D. B. Melrose, 1995, Mon. Not. R. Astron. Soc. **276**, 372.

Luo, R., K. Lee, D. R. Lorimer, and B. Zhang, 2018, Mon. Not. R. Astron. Soc. **481**, 2320.

Luo, R., Y. Men, K. Lee, W. Wang, D. R. Lorimer, and B. Zhang, 2020, Mon. Not. R. Astron. Soc. **494**, 665.

Luo, R., *et al.*, 2020, Nature (London) **586**, 693.

Lyubarsky, Y., 2008, Astrophys. J. **682**, 1443.

Lyubarsky, Y., 2014, Mon. Not. R. Astron. Soc. **442**, L9.

Lyubarsky, Y., 2020, Astrophys. J. **897**, 1.

Lyubarsky, Y., 2021, Universe **7**, 56.

Lyutikov, M., 2017, Astrophys. J. **838**, L13.

Lyutikov, M., 2020a, Phys. Rev. E **102**, 013211.

Lyutikov, M., 2020b, Astrophys. J. **889**, 135.

Lyutikov, M., 2021, Astrophys. J. **922**, 166.

Lyutikov, M., M. V. Barkov, and D. Giannios, 2020, Astrophys. J. **893**, L39.

Lyutikov, M., R. D. Blandford, and G. Machabeli, 1999, Mon. Not. R. Astron. Soc. **305**, 338.

Macquart, J.-P., and J. Y. Koay, 2013, Astrophys. J. **776**, 125.

Macquart, J.-P., *et al.*, 2020, Nature (London) **581**, 391.

Mahlmann, J. F., A. A. Philippov, A. Levinson, A. Spitkovsky, and H. Hakobyan, 2022, arXiv:2203.04320.

Mahony, E. K., *et al.*, 2018, Astrophys. J. **867**, L10.

Marcote, B., *et al.*, 2017, Astrophys. J. **834**, L8.

Marcote, B., *et al.*, 2020, Nature (London) **577**, 190.

Margalit, B., P. Beniamini, N. Sridhar, and B. D. Metzger, 2020, Astrophys. J. **899**, L27.

Margalit, B., E. Berger, and B. D. Metzger, 2019, Astrophys. J. **886**, 110.

Margalit, B., and B. D. Metzger, 2018, Astrophys. J. **868**, L4.

Margalit, B., B. D. Metzger, and L. Sironi, 2020, Mon. Not. R. Astron. Soc. **494**, 4627.

Masui, K., *et al.*, 2015, Nature (London) **528**, 523.

McLaughlin, M. A., *et al.*, 2006, Nature (London) **439**, 817.

McQuinn, M., 2014, Astrophys. J. Lett. **780**, L33.

Melikidze, G. I., J. A. Gil, and A. D. Pataraya, 2000, Astrophys. J. **544**, 1081.

Melrose, D. B., 1978, Astrophys. J. **225**, 557.

Melrose, D. B., 2010, Astrophys. J. **725**, 1600.

Melrose, D. B., 2017, Rev. Mod. Plasma Phys. **1**, 5.

Melrose, D. B., P. A. Robinson, and T. M. Feletto, 1995, Sol. Phys. **158**, 139.

Men, Y., *et al.*, 2019, Mon. Not. R. Astron. Soc. **489**, 3643.

Mereghetti, S., *et al.*, 2020, Astrophys. J. **898**, L29.

Mészáros, P., 1992, *High-Energy Radiation from Magnetized Neutron Stars* (University of Chicago Press, Chicago).

Mészáros, P., and M. J. Rees, 1997, Astrophys. J. **476**, 232.

Metzger, B. D., E. Berger, and B. Margalit, 2017, Astrophys. J. **841**, 14.

Metzger, B. D., D. Giannios, T. A. Thompson, N. Bucciantini, and E. Quataert, 2011, Mon. Not. R. Astron. Soc. **413**, 2031.

Metzger, B. D., B. Margalit, and L. Sironi, 2019, Mon. Not. R. Astron. Soc. **485**, 4091.

Metzger, B. D., N. Sridhar, B. Margalit, P. Beniamini, and L. Sironi, 2022, Astrophys. J. **925**, 135.

Michel, F. C., 1982, Rev. Mod. Phys. **54**, 1.

Michilli, D., et al., 2018, Nature (London) **553**, 182.

Mingarelli, C. M. F., J. Levin, and T. J. W. Lazio, 2015, Astrophys. J. **814**, L20.

Moroianu, A., L. Wen, C. W. James, S. Ai, M. Kovalam, F. Panther, and B. Zhang, 2022, arXiv:2212.00201.

Most, E. R., A. Nathanail, and L. Rezzolla, 2018, Astrophys. J. **864**, 117.

Mottez, F., and P. Zarka, 2014, Astron. Astrophys. **569**, A86.

Muñoz, J. B., E. D. Kovetz, L. Dai, and M. Kamionkowski, 2016, Phys. Rev. Lett. **117**, 091301.

Murase, K., K. Kashiyama, and P. Mészáros, 2016, Mon. Not. R. Astron. Soc. **461**, 1498.

Muslimov, A. G., and A. K. Harding, 2004, Astrophys. J. **606**, 1143.

Muslimov, A. G., and A. I. Tsygan, 1992, Mon. Not. R. Astron. Soc. **255**, 61.

Nathanail, A., E. R. Most, and L. Rezzolla, 2017, Mon. Not. R. Astron. Soc. **469**, L31.

Nemiroff, R. J., 1994, Comments Astrophys. **17**, 189, https://articles.adsabs.harvard.edu/pdf/1994ComAp..17..189N.

Nicholl, M., P. K. G. Williams, E. Berger, V. A. Villar, K. D. Alexander, T. Eftekhari, and B. D. Metzger, 2017, Astrophys. J. **843**, 84.

Niino, Y., et al., 2022, Astrophys. J. **931**, 109.

Nimmo, K., J. W. T. Hessels, A. Keimpema, A. M. Archibald, J. M. Cordes, R. Karuppusamy, F. Kirsten, D. Z. Li, B. Marcote, and Z. Paragi, 2021, Nat. Astron. **5**, 594.

Nimmo, K., et al., 2022, Nat. Astron. **6**, 393.

Niu, C. H., et al., 2022, Nature (London) **606**, 873.

Niu, J.-R., et al., 2022, Res. Astron. Astrophys. **22**, 124004.

O'Sullivan, S. P., et al., 2012, Mon. Not. R. Astron. Soc. **421**, 3300.

Ouyed, R., D. Leahy, and N. Koning, 2020, Res. Astron. Astrophys. **20**, 027.

Ouyed, R., D. Leahy, and N. Koning, 2021, Mon. Not. R. Astron. Soc. **500**, 4414.

Palaniswamy, D., Y. Li, and B. Zhang, 2018, Astrophys. J. **854**, L12.

Palaniswamy, D., R. B. Wayth, C. M. Trott, J. N. McCallum, S. J. Tingay, and C. Reynolds, 2014, Astrophys. J. **790**, 63.

Pan, Z., and H. Yang, 2019, Phys. Rev. D **100**, 043025.

Panther, F. H., et al., 2023, Mon. Not. R. Astron. Soc. **519**, 2235.

Pastor-Marazuela, I., et al., 2021, Nature (London) **596**, 505.

Petroff, E., J. W. T. Hessels, and D. R. Lorimer, 2019, Astron. Astrophys. Rev. **27**, 4.

Petroff, E., J. W. T. Hessels, and D. R. Lorimer, 2022, Astron. Astrophys. Rev. **30**, 2.

Petroff, E., et al., 2015a, Mon. Not. R. Astron. Soc. **447**, 246.

Petroff, E., et al., 2015b, Mon. Not. R. Astron. Soc. **454**, 457.

Petroff, E., et al., 2015c, Mon. Not. R. Astron. Soc. **451**, 3933.

Philippov, A., A. Timokhin, and A. Spitkovsky, 2020, Phys. Rev. Lett. **124**, 245101.

Philippov, A. A., and A. Spitkovsky, 2018, Astrophys. J. **855**, 94.

Piro, A. L., 2012, Astrophys. J. **755**, 80.

Piro, A. L., 2016, Astrophys. J. **824**, L32.

Piro, A. L., and B. M. Gaensler, 2018, Astrophys. J. **861**, 150.

Piro, L., et al., 2021, Astron. Astrophys. **656**, L15.

Pitjeva, E. V., and N. P. Pitjev, 2018, Astron. Lett. **44**, 554.

Platts, E., A. Weltman, A. Walters, S. P. Tendulkar, J. E. B. Gordin, and S. Kandhai, 2019, Phys. Rep. **821**, 1.

Pleunis, Z., et al., 2021a, Astrophys. J. **923**, 1.

Pleunis, Z., et al., 2021b, Astrophys. J. **911**, L3.

Plotnikov, I., and L. Sironi, 2019, Mon. Not. R. Astron. Soc. **485**, 3816.

Pol, N., M. T. Lam, M. A. McLaughlin, T. J. W. Lazio, and J. M. Cordes, 2019, Astrophys. J. **886**, 135.

Popov, S. B., and K. A. Postnov, 2010, in Evolution of Cosmic Objects through Their Physical Activity, edited by H. A. Harutyunian, A. M. Mickaelian, and Y. Terzian (Gitutyun Publishing House, Yerevan, Armenia), pp. 129–132, https://ui.adsabs.harvard.edu/abs/2010vaoa.conf..129P/abstract.

Popov, S. B., K. A. Postnov, and M. S. Pshirkov, 2018, Phys. Usp. **61**, 965.

Prochaska, J. X., and Y. Zheng, 2019, Mon. Not. R. Astron. Soc. **485**, 648.

Prochaska, J. X., et al., 2019, Science **366**, 231.

Qiang, D.-C., S.-L. Li, and H. Wei, 2022, J. Cosmol. Astropart. Phys. **01**, 040.

Qiao, G. J., and W. P. Lin, 1998, Astron. Astrophys. **333**, 172, https://ui.adsabs.harvard.edu/abs/1998A%26A...333..172Q/abstract .

Qiao, G. J., J. F. Liu, B. Zhang, and J. L. Han, 2001, Astron. Astrophys. **377**, 964.

Qu, Y., P. Kumar, and B. Zhang, 2022, Mon. Not. R. Astron. Soc. **515**, 2020.

Qu, Y., and B. Zhang, 2023, arXiv:2302.09697.

Qu, Y., B. Zhang, and P. Kumar, 2023, Mon. Not. R. Astron. Soc. **518**, 66.

Radhakrishnan, V., and D. J. Cooke, 1969, Astrophys. Lett. **3**, 225.

Rafiei-Ravandi, M., et al., 2021, Astrophys. J. **922**, 42.

Rajwade, K. M., et al., 2020, Mon. Not. R. Astron. Soc. **495**, 3551.

Rankin, J. M., 1993, Astrophys. J. **405**, 285.

Ravi, V., 2019, Nat. Astron. **3**, 928.

Ravi, V., and P. D. Lasky, 2014, Mon. Not. R. Astron. Soc. **441**, 2433.

Ravi, V., et al., 2016, Science **354**, 1249.

Ravi, V., et al., 2019, Nature (London) **572**, 352.

Ravi, V., et al., 2022, Mon. Not. R. Astron. Soc. **513**, 982.

Rea, N., et al., 2010, Science **330**, 944.

Rees, M. J., 1977, Nature (London) **266**, 333.

Rice, J. R., and B. Zhang, 2017, J. High Energy Astrophys. **13–14**, 22.

Rickett, B. J., 1977, Annu. Rev. Astron. Astrophys. **15**, 479.

Rickett, B. J., 1990, Annu. Rev. Astron. Astrophys. **28**, 561.

Ridnaia, A., et al., 2021, Nat. Astron. **5**, 372.

Romero, G. E., M. V. del Valle, and F. L. Vieyro, 2016, Phys. Rev. D **93**, 023001.

Rosa, J. G., and T. W. Kephart, 2018, Phys. Rev. Lett. **120**, 231102.

Rowe, E. T., 1995, Astron. Astrophys. **296**, 275, https://ui.adsabs.harvard.edu/abs/1995A%26A...296..275R/abstract.

Rowlinson, A., and G. E. Anderson, 2019, Mon. Not. R. Astron. Soc. **489**, 3316.

Rowlinson, A., P. T. O'Brien, B. D. Metzger, N. R. Tanvir, and A. J. Levan, 2013, Mon. Not. R. Astron. Soc. **430**, 1061.

Rowlinson, A., et al., 2010, Mon. Not. R. Astron. Soc. **409**, 531.

Ruan, W.-H., Z.-K. Guo, R.-G. Cai, and Y.-Z. Zhang, 2018, arXiv:1807.09495.

Ruderman, M. A., and P. G. Sutherland, 1975, Astrophys. J. **196**, 51.

Rybicki, G. B., and A. P. Lightman, 1979, Radiative Processes in Astrophysics (Wiley-VCH, Weinheim).

Sagiv, A., and E. Waxman, 2002, Astrophys. J. **574**, 861.

Sakamoto, T., E. Troja, A. Lien, B. Zhang, S. B. Cenko, V. Cunningham, and E. Berger, 2021, Astrophys. J. **908**, 137.

Sarachik, E. S., and G. T. Schappert, 1970, Phys. Rev. D **1**, 2738.

Sari, R., T. Piran, and R. Narayan, 1998, Astrophys. J. **497**, L17.

Shao, L., and B. Zhang, 2017, Phys. Rev. D **95**, 123010.

Shin, K., *et al.*, 2022, arXiv:2207.14316.

Shirasaki, M., R. Takahashi, K. Osato, and K. Ioka, 2022, Mon. Not. R. Astron. Soc. **512**, 1730.

Simha, S., *et al.*, 2020, Astrophys. J. **901**, 134.

Sironi, L., 2021 (private communication).

Sironi, L., I. Plotnikov, J. Nättilä, and A. M. Beloborodov, 2021, Phys. Rev. Lett. **127**, 035101.

Skribanowitz, N., I. P. Herman, J. C. MacGillivray, and M. S. Feld, 1973, Phys. Rev. Lett. **30**, 309.

Smallwood, J. L., R. G. Martin, and B. Zhang, 2019, Mon. Not. R. Astron. Soc. **485**, 1367.

Sobacchi, E., Y. Lyubarsky, A. M. Beloborodov, and L. Sironi, 2022, Mon. Not. R. Astron. Soc. **511**, 4766.

Sobacchi, E., Y. Lyubarsky, A. M. Beloborodov, L. Sironi, and M. Iwamoto, 2022, arXiv:2210.08754.

Spitkovsky, A., 2006, Astrophys. J. **648**, L51.

Spitler, L. G., *et al.*, 2016, Nature (London) **531**, 202.

Sridhar, N., and B. D. Metzger, 2022, Astrophys. J. **937**, 5.

Sridhar, N., B. D. Metzger, P. Beniamini, B. Margalit, M. Renzo, L. Sironi, and K. Kovlakas, 2021, Astrophys. J. **917**, 13.

Sridhar, N., J. Zrake, B. D. Metzger, L. Sironi, and D. Giannios, 2021, Mon. Not. R. Astron. Soc. **501**, 3184.

Stix, T. H., 1992, *Waves in Plasmas* (American Institute of Physics, Melville, NY).

Szary, A., B. Zhang, G. I. Melikidze, J. Gil, and R.-X. Xu, 2014, Astrophys. J. **784**, 59.

Takahashi, R., K. Ioka, A. Mori, and K. Funahashi, 2021, Mon. Not. R. Astron. Soc. **502**, 2615.

Tavani, M., *et al.*, 2021, Nat. Astron. **5**, 401.

Tendulkar, S. P., V. M. Kaspi, and C. Patel, 2016, Astrophys. J. **827**, 59.

Tendulkar, S. P., *et al.*, 2017, Astrophys. J. **834**, L7.

Thompson, C., 2017a, Astrophys. J. **844**, 65.

Thompson, C., 2017b, Astrophys. J. **844**, 162.

Thompson, C., 2022, arXiv:2209.11136.

Thompson, C., R. D. Blandford, C. R. Evans, and E. S. Phinney, 1994, Astrophys. J. **422**, 304.

Thompson, C., and R. C. Duncan, 1995, Mon. Not. R. Astron. Soc. **275**, 255.

Thompson, C., and R. C. Duncan, 1996, Astrophys. J. **473**, 322.

Thompson, C., and R. C. Duncan, 2001, Astrophys. J. **561**, 980.

Thompson, C., M. Lyutikov, and S. R. Kulkarni, 2002, Astrophys. J. **574**, 332.

Thornton, D., *et al.*, 2013, Science **341**, 53.

Timokhin, A. N., 2006, Mon. Not. R. Astron. Soc. **368**, 1055.

Timokhin, A. N., 2010, Mon. Not. R. Astron. Soc. **408**, 2092.

Timokhin, A. N., and J. Arons, 2013, Mon. Not. R. Astron. Soc. **429**, 20.

Tingay, S. J., and D. L. Kaplan, 2016, Astrophys. J. **820**, L31.

Tkachev, I. I., 2015, JETP Lett. **101**, 1.

Tong, H., and H. G. Wang, 2022, arXiv:2202.05475.

Totani, T., 2013, Publ. Astron. Soc. Jpn. **65**, L12.

Usov, V. V., 1987, Astrophys. J. **320**, 333.

Usov, V. V., 1992, Nature (London) **357**, 472.

Vachaspati, T., 2008, Phys. Rev. Lett. **101**, 141301.

Van Waerbeke, L., and A. Zhitnitsky, 2019, Phys. Rev. D **99**, 043535.

Vedantham, H. K., and V. Ravi, 2019, Mon. Not. R. Astron. Soc. **485**, L78.

Vieyro, F. L., G. E. Romero, V. Bosch-Ramon, B. Marcote, and M. V. del Valle, 2017, Astron. Astrophys. **602**, A64.

Wada, T., K. Ioka, and B. Zhang, 2021, Astrophys. J. **920**, 54.

Wada, T., M. Shibata, and K. Ioka, 2020, Prog. Theor. Exp. Phys. 103E01.

Wadiasingh, Z., P. Beniamini, A. Timokhin, M. G. Baring, A. J. van der Horst, A. K. Harding, and D. Kazanas, 2020, Astrophys. J. **891**, 82.

Wadiasingh, Z., and C. Chirenti, 2020, Astrophys. J. **903**, L38.

Wadiasingh, Z., and A. Timokhin, 2019, Astrophys. J. **879**, 4.

Wald, R. M., 1974, Phys. Rev. D **10**, 1680.

Walters, A., A. Weltman, B. M. Gaensler, Y.-Z. Ma, and A. Witzemann, 2018, Astrophys. J. **856**, 65.

Wang, F. Y., Y. Y. Wang, Y.-P. Yang, Y. W. Yu, Z. Y. Zuo, and Z. G. Dai, 2020, Astrophys. J. **891**, 72.

Wang, F. Y., G. Q. Zhang, Z. G. Dai, and K. S. Cheng, 2022, Nat. Commun. **13**, 4382.

Wang, J.-S., and D. Lai, 2020, Astrophys. J. **892**, 135.

Wang, J.-S., Y.-P. Yang, X.-F. Wu, Z.-G. Dai, and F.-Y. Wang, 2016, Astrophys. J. **822**, L7.

Wang, P., 2023 (to be published).

Wang, P. F., C. Wang, and J. L. Han, 2012, Mon. Not. R. Astron. Soc. **423**, 2464.

Wang, W., R. Luo, H. Yue, X. Chen, K. Lee, and R. Xu, 2018, Astrophys. J. **852**, 140.

Wang, W., B. Zhang, X. Chen, and R. Xu, 2019, Astrophys. J. **876**, L15.

Wang, W.-Y., J.-C. Jiang, K. Lee, R. Xu, and B. Zhang, 2022, Mon. Not. R. Astron. Soc. **517**, 5080.

Wang, W.-Y., R. Xu, and X. Chen, 2020, Astrophys. J. **899**, 109.

Wang, W.-Y., Y.-P. Yang, C.-H. Niu, R. Xu, and B. Zhang, 2022, Astrophys. J. **927**, 105.

Wang, W.-Y., B. Zhang, X. Chen, and R. Xu, 2020, Mon. Not. R. Astron. Soc. **499**, 355.

Wang, X.-G., L. Li, Y.-P. Yang, J.-W. Luo, B. Zhang, D.-B. Lin, E.-W. Liang, and S.-M. Qin, 2020, Astrophys. J. **894**, L22.

Wang, Y. K., and F. Y. Wang, 2018, Astron. Astrophys. **614**, A50.

Wang, Y.-F., and A. H. Nitz, 2022, Astrophys. J. **937**, 89.

Waxman, E., 2017, Astrophys. J. **842**, 34.

Wei, J.-J., H. Gao, X.-F. Wu, and P. Mészáros, 2015, Phys. Rev. Lett. **115**, 261101.

Williams, P. K. G., and E. Berger, 2016, Astrophys. J. **821**, L22.

Wilson, D. B., and M. J. Rees, 1978, Mon. Not. R. Astron. Soc. **185**, 297.

Woosley, S. E., 2010, Astrophys. J. **719**, L204.

Wu, X.-F., S.-B. Zhang, H. Gao, J.-J. Wei, Y.-C. Zou, W.-H. Lei, B. Zhang, Z.-G. Dai, and P. Mészáros, 2016, Astrophys. J. **822**, L15.

Xiao, D., F. Wang, and Z. Dai, 2021, Sci. China Phys. Mech. Astron. **64**, 249501.

Xing, N., H. Gao, J.-J. Wei, Z. Li, W. Wang, B. Zhang, X.-F. Wu, and P. Mészáros, 2019, Astrophys. J. **882**, L13.

Xu, H., *et al.*, 2022, Nature (London) **609**, 685.

Xu, J., and J. L. Han, 2015, Res. Astron. Astrophys. **15**, 1629.

Xu, R. X., J. F. Liu, J. L. Han, and G. J. Qiao, 2000, Astrophys. J. **535**, 354.

Xu, S., D. H. Weinberg, and B. Zhang, 2021, Astrophys. J. **922**, L31.

Xu, S., and B. Zhang, 2016, Astrophys. J. **832**, 199.

Xu, S., and B. Zhang, 2020, Astrophys. J. **898**, L48.

Yamasaki, S., T. Totani, and K. Kiuchi, 2018, Publ. Astron. Soc. Jpn. **70**, 39.

Yang, H., and Y.-C. Zou, 2020, Astrophys. J. **893**, L31.

Yang, Y.-H., B.-B. Zhang, and B. Zhang, 2019, Astrophys. J. **875**, L19.

Yang, Y.-P., Q.-C. Li, and B. Zhang, 2020, Astrophys. J. **895**, 7.

Yang, Y.-P., W. Lu, Y. Feng, B. Zhang, and D. Li, 2022, Astrophys. J. **928**, L16.

Yang, Y.-P., R. Luo, Z. Li, and B. Zhang, 2017, Astrophys. J. **839**, L25.

Yang, Y.-P., S. Xu, and B. Zhang, 2022, arXiv:2208.08712.

Yang, Y.-P., and B. Zhang, 2016, Astrophys. J. **830**, L31.

Yang, Y.-P., and B. Zhang, 2017, Astrophys. J. **847**, 22.

Yang, Y.-P., and B. Zhang, 2018, Astrophys. J. **868**, 31.

Yang, Y.-P., and B. Zhang, 2020, Astrophys. J. **892**, L10.

Yang, Y.-P., and B. Zhang, 2021, Astrophys. J. **919**, 89.

Yang, Y.-P., B. Zhang, and Z.-G. Dai, 2016, Astrophys. J. **819**, L12.

Yang, Y.-P., B. Zhang, and J.-Y. Wei, 2019, Astrophys. J. **878**, 89.

Yang, Y.-P., J.-P. Zhu, B. Zhang, and X.-F. Wu, 2020, Astrophys. J. **901**, L13.

Yao, J. M., R. N. Manchester, and N. Wang, 2017, Astrophys. J. **835**, 29.

Ye, J., K. Wang, and Y.-F. Cai, 2017, Eur. Phys. J. C **77**, 720.

Yi, S.-X., H. Gao, and B. Zhang, 2014, Astrophys. J. **792**, L21.

Yu, Y.-W., K.-S. Cheng, G. Shiu, and H. Tye, 2014, J. Cosmol. Astropart. Phys. **11**, 040.

Yu, Y.-W., Y.-C. Zou, Z.-G. Dai, and W.-F. Yu, 2021, Mon. Not. R. Astron. Soc. **500**, 2704.

Yuan, Y., A. M. Beloborodov, A. Y. Chen, and Y. Levin, 2020, Astrophys. J. **900**, L21.

Zhang, B., 2014, Astrophys. J. Lett. **780**, L21.

Zhang, B., 2016, Astrophys. J. Lett. **827**, L31.

Zhang, B., 2017, Astrophys. J. **836**, L32.

Zhang, B., 2018a, Astrophys. J. **867**, L21.

Zhang, B., 2018b, Astrophys. J. **854**, L21.

Zhang, B., 2018c, *The Physics of Gamma-Ray Bursts* (Cambridge University Press, Cambridge, England).

Zhang, B., 2019, Astrophys. J. **873**, L9.

Zhang, B., 2020a, Front. Phys. **15**, 54502.

Zhang, B., 2020b, Astrophys. J. **890**, L24.

Zhang, B., 2020c, Nature (London) **587**, 45.

Zhang, B., 2020d, Nature (London) **582**, 344.

Zhang, B., 2021, Astrophys. J. **907**, L17.

Zhang, B., 2022, Astrophys. J. **925**, 53.

Zhang, B., and A. K. Harding, 2000, Astrophys. J. **532**, 1150.

Zhang, B., A. K. Harding, and A. G. Muslimov, 2000, Astrophys. J. **531**, L135.

Zhang, B., and P. Mészáros, 2001, Astrophys. J. **552**, L35.

Zhang, B., G. J. Qiao, W. P. Lin, and J. L. Han, 1997, Astrophys. J. **478**, 313.

Zhang, B.-B., and B. Zhang, 2017, Astrophys. J. **843**, L13.

Zhang, C. F., *et al.*, 2020, Astronomer's Telegram **13699**, 1, https://ui .adsabs.harvard.edu/abs/2020ATel13699....1Z/abstract.

Zhang, G. Q., H. Yu, J. H. He, and F. Y. Wang, 2020, Astrophys. J. **900**, 170.

Zhang, R. C., and B. Zhang, 2022, Astrophys. J. **924**, L14.

Zhang, R. C., B. Zhang, Y. Li, and D. R. Lorimer, 2021, Mon. Not. R. Astron. Soc. **501**, 157.

Zhang, X., and H. Gao, 2020, Mon. Not. R. Astron. Soc. **498**, L1.

Zhang, Y., J.-J. Geng, and Y.-F. Huang, 2018, Astrophys. J. **858**, 88.

Zhang, Y. G., V. Gajjar, G. Foster, A. Siemion, J. Cordes, C. Law, and Y. Wang, 2018, Astrophys. J. **866**, 149.

Zhang, Y.-K., *et al.*, 2022, Res. Astron. Astrophys. **22**, 124002.

Zheleznyakov, V. V., and E. Y. Zlotnik, 1964, Sov. Astron. **7**, 485, https://ui.adsabs.harvard.edu/abs/1964SvA.....7..485Z/abstract.

Zheng, Z., E. O. Ofek, S. R. Kulkarni, J. D. Neill, and M. Juric, 2014, Astrophys. J. **797**, 71.

Zhong, S.-Q., and Z.-G. Dai, 2020, Astrophys. J. **893**, 9.

Zhong, S.-Q., Z.-G. Dai, and C.-M. Deng, 2019, Astrophys. J. **883**, L19.

Zhong, S.-Q., W.-J. Xie, C.-M. Deng, L. Li, Z.-G. Dai, and H.-M. Zhang, 2022, Astrophys. J. **926**, 206.

Zhou, B., X. Li, T. Wang, Y.-Z. Fan, and D.-M. Wei, 2014, Phys. Rev. D **89**, 107303.

Zhou, D. J., *et al.*, 2022, Res. Astron. Astrophys. **22**, 124001.

Zhou, H., Z. Li, K. Liao, C. Niu, H. Gao, Z. Huang, L. Huang, and B. Zhang, 2022, Astrophys. J. **928**, 124.

Zhu, W.-W., *et al.*, 2023, Sci. Adv. **9**, 6198.

Zhu-Ge, J.-M., J.-W. Luo, and B. Zhang, 2023, Mon. Not. R. Astron. Soc. **519**, 1823.